NTNU
Norwegian University of
Science and Technology

A Study of the Strength and the Physical Properties of Glacier-ice Runways

Assesment of Troll Airfield, Antarctica

Maren Salte Kallelid

Civil and Environmental Engineering
Submission date: June 2018
Supervisor: Knut Vilhelm Høyland, IBM
Co-supervisor: Torodd Skjerve Nord, IBM
Arne Aalberg, IBM

Norwegian University of Science and Technology
Department of Civil and Environmental Engineering

NORWEGIAN UNIVERSITY OF SCIENCE AND TECHNOLOGY
DEPARTMENT OF CIVIL AND ENVIRONMENTAL ENGINEERING

Report Title: **A Study of the Strength and Physical Properties of Glacier-ice Runways – Assessment of Troll Airfield, Antarctica**	Dato: **11.06.2018** Number of pages: **122**	
	Master Thesis	x
Name: Maren Salte Kallelid		
Professor in charge/supervisor: Knut V. Høyland		
Other external professional contacts/supervisors: Postdoc. Torodd S. Nord and Prof. Arne Aalberg		

Abstract:
Airfields located in Antarctica are unique because the runways are constructed by glacier ice. Ice as a construction material differs from conventional runway materials in sense of strength, hardness and temperature dependency, and new techniques and tools are therefore required for monitoring the runway strength. Troll Airfield is an example of such an airport. However, this airfield experiences an additional challenge related to particle accumulation on the runway surface. The minerals absorb heat from the sun due to the dark colour and thereby melt the surrounding ice. The holes are repaired by removing the particles and freezing new ice, a method called patching.

A field investigation program was conducted at Troll Airfield where the objective was to determine the strength and the physical properties of the runway ice. The difference between the glacier ice and the patch ice was emphasized. For this purpose, an indentation test and a penetration test were conducted along the runway, and ice specimens were brought back to NTNU for determination of the physical properties.

The indentation test was conducted by use of a recently developed borehole jack. This series involved a 30-mm diameter piston indenting a borehole wall at constant displacement rate of ~0.9 mm/s. The results indicated that the ice strength was mainly related to ice temperature, especially for temperatures above ~ -5 °C. The patch ice was found to absorb more heat from sun radiation than glacier ice, and the patch ice strength was therefore in general weaker than the glacier ice. Furthermore, the failure behaviour of the stress-time curves were studied, and a thorough literature review is presented on this topic. The collected data showed that ductile failure behaviours dominated for temperatures above -8 °C, and that brittle failure behaviours became relevant in the colder temperature range. This observation is supported in the literature, where a corresponding ductile-to-brittle transition is found for increasing indentation rates. In particular, a "sawtooth" loading pattern was studied and was related to a microstructurally modified "layer" in the ice adjacent to the piston.

A Russian snow penetrometer test was recommended by Cold Regions Research and Engineering Laboratory (CRREL) as a monitoring procedure of the runway strength at Troll Airfield. However, this test proved to be unsuited for the ice pavement at Troll because the ice was too hard and dens, and sufficient penetration was thereby suppressed.

Thin sections and CT scanning of the runway ice specimens have been performed in the cold laboratories at NTNU. The glacier ice structure is characterized as granular with moderate grain elongation in vertical direction. The average grain size is 4-5 mm in the horizontal plane, and the density is 845 kg/m^3. A small degree of anisotropy is observed. The patch ice has an isotropic, granular structure with grain sizes varying from 1-7 mm. The patch ice density is 898 kg/m^3. The CT scan of the ice specimens showed that the patch ice contains less air bubbles than the glacier ice.

Keywords:

1. borehole jack
2. indentation test
3. thin sections
4. glacier ice

Maren Salte Kallelid

____
(sign.)

MASTER DEGREE THESIS

Spring 2018
for

Student: Maren S. Kallelid

A Study of the Strength and Physical Properties of Glacier-ice Runways

BACKGROUND

The Norwegian Polar Institute (NPI) requested assistance to determine the strength and physical properties of their runway located in Antarctica. The runway experienced challenges related to the occurrence of sand particles that accumulate on the runway and create melt holes. The current procedure to repair these holes involve removal of sand particles and subsequently freeze new ice, so-called patch ice. Today, little information exist on the physical and mechanical properties of the a) runway ice and b) the patch ice. Therefore, the task for this thesis is to determine these by means of using a recently developed borehole jack and collecting samples for determination of physical properties at NTNU. NPI has also been adviced by the Cold Regions Research and Engineering Laboratory (CRREL) to implement a Russian Snow Penetrometer test (RSP) to their maintenance routines of the runway, therewith a secondary goal of this thesis shall assess the usefulness of this test.

TASK

Troll airfield has large traffic with a variety of airplanes and a runway material that depend heavily on the meteorological conditions. Safe air traffic requires a survey of the physical and mechanical properties of the runway. In the initial phase of this project, NTNU and UNIS evaluated a range of testing methods which could meet both HSE and repeatability requirements of the testing. It was decided to use a lightweight borehole jack, initially designed by M-tech for the military to determine the strength of river ice. The student is supposed to conduct fieldwork in Antarctica, evaluate the strength of the Troll Airfield by means of this borehole jack, and further assess the testing methodology and recommend improvements of their current runway monitoring. The student shall further determine the physical properties of the two types of ice, the patch ice and runway ice, and finally assess the usefulness of the RSP testing.

Task description

- Conduct Borehole jack testing
- Conduct RSP testing
- Determine the physical properties of the runway ice and patch ice
- Assess the mechanical strength

Objective and purpose

The objective is to determine the mechanical and physical properties of the Antarctic ice and assess the usefulness of the RSP test for the Troll runway monitoring program.

Subtasks and research questions

- Ice failure patterns
- Temperature dependence on the strength
- Better understanding of the physical properties of the ice adjacent to the borehole jack indenter.

Professor in charge: Knut V. Høyland

Postdoc Torodd S. Nord
Prof. Arne Aalberg

Department of Civil and Transport Engineering, NTNU
Date: 09.06.2017, (revised: dd.mm.yyyy)

____
Professor in charge (signature)

Preface

This paper constitutes the master thesis for Maren Salte Kallelid, and makes the concluding work of a five years long Master Degree's Program at Department of Civil and Transport Engineering at NTNU. This thesis was initiated by the Norwegian Polar Institute (NPI), and has been a collaboration project between them and NTNU.

The purpose of the project is to investigate the runway strength for pavements constructed by glacier material. A three weeks long field work program has been conducted at Troll Airfield located in Antarctica during February 2018. Additional investigations of the physical properties of the runway ice have been conducted in the cold laboratory at NTNU. For this purpose, ice specimens were collected at the runway and transported to Trondheim in a freezing box.

The work presented in this paper will be important in the development for a new monitoring program of the runway strength at Troll Airfield.

Acknowledgements

First of all, I want to thank the Norwegian Polar Institute for giving a master student the opportunity to visit the Troll station. When I signed up for this master thesis, I was first of all very excited about the trip to Antarctica. However, the scientific part also proved to be interesting, and I enjoyed the field work. A special thank to Sven Lidstrøm for helping out in organizing the experiments, both at Troll and ahead of the trip.

Secondly I want to thank my co-supervisor Torodd S. Nord. He has been helping me with all the practical challenges I have met, from the very beginning of this project in September 2017 until now. Planning a field work, especially when sited in Antarctica, proved to be more complicated than I first expected. Torodd has also showed great interest in the field data I collected, and his engagement in my results was inspiring. My supervisor Knut Høyland also gave highly useful feedback on my analysis whenever I asked him, and he was always available for a discussion.

I also want to thank Postdoc. Sønke Maus for suggesting to bring ice specimens back to Trondheim for further investigation. He also conducted the CT scan and provided me with results that I believe increased the scientific level of this thesis.

Lastly, I want to thank friends and family for support and encouragement whenever this project felt a bit overwhelming.

Abstract

Airfields located in Antarctica are unique because the runways are constructed by glacier ice. Ice as a construction material differs from conventional runway materials in sense of strength, hardness and temperature dependency, and new techniques and tools are therefore required for monitoring the runway strength. Troll Airfield is an example of such an airport. However, this airfield experiences an additional challenge related to particle accumulation on the runway surface. The minerals absorb heat from the sun due to the dark colour and thereby melt the surrounding ice. The holes are repaired by removing the particles and freezing new ice, a method called patching.

A field investigation program was conducted at Troll Airfield where the objective was to determine the strength and the physical properties of the runway ice. The difference between the glacier ice and the patch ice was emphasized. For this purpose, an indentation test and a penetration test were conducted along the runway, and ice specimens were brought back to NTNU for determination of the physical properties.

The indentation test was conducted by use of a recently developed borehole jack. This series involved a 30-mm diameter piston indenting a borehole wall at constant displacement rate of $\sim$ 0.9 mm s^{-1}. The results indicated that the ice strength was mainly related to ice temperature, especially for temperatures above $\sim$ -5°C. The patch ice was found to absorb more heat from sun radiation than glacier ice, and the patch ice strength was therefore in general weaker than the glacier ice. Furthermore, the failure behaviour of the stress-time curves were studied, and a thorough literature review is presented on this topic. The collected data showed that ductile failure behaviours dominated for temperatures above -8°C, and that brittle failure behaviours became relevant in the colder temperature range. This observation is supported in the literature, where a corresponding ductile-to-brittle transition is found for increasing indentation rates. In particular, a "sawtooth" loading pattern was studied and related to a microstructurally modified "layer" in the ice adjacent to the piston.

A Russian snow penetrometer test was recommended by Cold Regions Research and Engineering Laboratory (CRREL) as a monitoring procedure of the runway strength at Troll Airfield. However, this test proved to be unsuited for the ice pavement at Troll because the ice was too hard and dens, and sufficient penetration was thereby suppressed.

Thin sections and CT scanning of the runway ice specimens have been performed in the cold laboratories at NTNU. The glacier ice structure is characterized as granular with moderate grain elongation in vertical direction. The average grain size is 4-5 mm in the horizontal plane, and the density is 845 kg m^{-3}. A small degree of anisotropy is observed. The patch ice has an isotropic, granular structure with grain sizes varying from 1-7 mm. The patch ice density is 898 kg m^{-3}. The CT scan of the ice specimens showed that the patch ice contains less air bubbles than the glacier ice.

Sammendrag

Flyplasser i Antarktis er unike fordi rullebanene er konstruert av isbremateriale. Is som bygningsmateriale er annerledes enn konvensjonelle rullebanematerialer i form av styrke, hardhet og temperaturavhengighet, og det er derfor nødvendig med nye teknikker og verktøy for å overvåke rullebanens styrke. Flyplassen på Troll er et eksempel på en slik flyplass med en rullebane laget av is. Denne flyplassen står ovenfor ekstra utfordringer knyttet til partikkelakkumulering på rullebanen. Mineralene absorberer varme fra solen på grunn av den mørke fargen, og smelter dermed den omliggende isen. Hullene repareres ved å fjerne partiklene og fryse ny is.

Et feltprogram ble gjennomført på flystripa til Troll, hvor målet var å bestemme styrken og de fysiske egenskapene til isen. Forskjellen mellom isbre-isen og reparasjonsisen ble vektlagt. For dette formålet ble en indentasjonstest og en penetrasjonstest utført langs rullebanen, og isprøver ble transportert tilbake til NTNU for å bestemme de fysiske egenskapene.

Indentasjonstesten ble utført ved hjelp av en nylig utviklet borhullsjekk. Denne testserien involverte et stempel på 30 mm i diameter som presses inn i en borhullsvegg med konstant forskyvningsrate på $\sim$ 0,9 mm s $^{-1}$. Resultatene indikerte at isstyrken hovedsakelig var relatert til istemperatur, spesielt for temperaturer over $\sim$ -5°C. Observasjoner viser at reperasjonsisen absorberer mer varme fra solstråling enn isbreen, og styrken av reperasjonsisen var derfor generelt svakere enn isbre-isen. Videre ble bruddoppførselen til spenning-tid-kurvene studert, og en grundig litteraturpresentasjon gis om dette emnet. De samlede dataene viste at duktile brudd dominerte for temperaturer over -8 °C, og at sprøbrudd ble gjeldende for kaldere temperaturer. Denne observasjonen støttes i litteraturen, hvor en tilsvarende duktil-til-sprø overgang er funnet for økte indentasjonsrater. Spesielt ble et "sagtann"-lastmønster studert, som også ble relatert til en mikrostrukturelt modifisert sone i isen rett bak stempelmerket.

RSP, en russisk penetrasjonsprøve, ble anbefalt av CRREL som en overvåkingsprosedyre av styrken av rullebanen på Troll. Denne testen viste seg imidlertid å være uegnet fordi isen på Troll var veldig hard og tett, og tilstrekkelig penetrasjon ble dermed ikke oppnådd.

Tynnslip og CT-scanning av isprøver fra rullebanen ble utført i kuldelaboratoriene ved NTNU. Isbre-isen er karakterisert som granulær med moderat kornforlengelse i vertikal retning. Den gjennomsnittlige kornstørrelsen er 4-5 mm i det horisontale planet, og tettheten er 845 kg m^{-3}. En liten grad av anisotropi er observert. Reparasjonsisen har en isotrop, granulær struktur med kornstørrelser varierende fra 1-7 mm. Reperasjonsisens tetthet er 898 kg m^{-3}. CT-scanningen av isprøvene viste at reparasjonsisen inneholder mindre luftbobler enn isbre-isen.

Table of Contents

Preface **iv**

Acknowledgements **v**

Abstract **vi**

Sammendrag **vii**

Table of Contents **xi**

List of Tables **xiii**

List of Figures **xvi**

Symbol list **xvii**

1 Introduction **1**
- 1.1 Research questions 2
- 1.2 Testing site 2
- 1.3 Field work program 3
- 1.4 Objectives 4
- 1.5 Literature 4

2 Theory **5**
- 2.1 Glacial ice 5
- 2.2 Physical and mechanical properties of granular ice 6
  - 2.2.1 Scientific strength parameters 6
  - 2.2.2 Failure processes 7
  - 2.2.3 Optical properties 9
- 2.3 Indentation failure 10
  - 2.3.1 Borehole ice strength value 10

2.3.2 Failure behaviour in load-time curves and corresponding damage events . . . 12
2.3.3 Temperature effect on failure behaviour and layer formation . . . 15

3 Experimental setup **17**
3.1 Organization of the experiments . . . 17
3.2 Borehole jack . . . 19
3.2.1 Equipment details . . . 19
3.2.2 Indentation load factor . . . 23
3.2.3 Experimental procedure . . . 25
3.3 Collecting ice core samples . . . 26
3.3.1 Density measurements . . . 28
3.4 Thin sections . . . 29
3.5 CT scanning . . . 30
3.6 Russian snow penetrometer . . . 30

4 Results **33**
4.1 Daily climate . . . 33
4.2 Borehole jack results . . . 34
4.2.1 Strength values . . . 38
4.2.2 Failure behaviour of stress-time curves . . . 39
4.2.3 Failure mode observations . . . 43
4.3 Density . . . 46
4.4 Thin sections . . . 47
4.5 CT-scanning . . . 53
4.6 Russian snow penetrometer . . . 58

5 Discussion **61**
5.1 Borehole jack . . . 61
5.1.1 Strength values . . . 62
5.1.2 Failure mode . . . 63
5.1.3 Comparing $blue_{10}$ and $patch_{10}$ results . . . 64
5.1.4 Stress evolution after terminal failure . . . 66
5.1.5 Failure behaviour variation with temperature . . . 66
5.1.6 Bubble density . . . 68
5.2 Density . . . 69
5.3 Thin sections . . . 70
5.3.1 BHJ-sections . . . 71
5.4 Russian snow penetrometer . . . 74

6 Further work **77**
6.1 Runway ice strength . . . 77
6.2 Testing equipment . . . 78
6.3 Scientific research . . . 78

7 Conclusion **79**
7.1 Practical 79
7.2 Scientific 80

Bibliography **80**

Appendix **I**
A Testing areas I
B Borehole jack results V

List of Tables

2.1 Typical densities for the snow, firn and glacier/blue ice 5

4.1 Weather and temperature for each day. 34
4.2 Summary of BHJ testing groups. 35
4.3 A collection of all the BHJ results. 36
4.4 Average strength values within temperature intervals. 39
4.5 Ranking of failure behaviour in the stress-time curves from BHJ recordings. 40
4.6 Pictures of thin sections made of blue ice. 48
4.7 Pictures of thin sections made of patch ice. 51
4.8 Pictures of thin sections made of the indented ice. 52
4.9 A collection of all the RSP results. 58

5.1 List of comparable $patch_{10}$ and $blue_{10}$ results 64
5.2 Bubble density calculations for CT scanned ice. 68
5.3 New bubble densities values based on the short mean bubble diameter. . . 69
5.4 Summary of all the measurement in the damage layer. 72

7.1 Characterization of the blue ice and patch ice 79

List of Figures

1.1 Overview picture of the runway at Troll Airfield. 1
1.2 Map of the area around the Troll station. 3

2.1 Flexural strength vs. bubble density. 7
2.2 Maximum differential stress vs. confining pressure. 8
2.3 Illustrations of the two kinds of compressive shear faults. 9
2.4 Four common types of failures behaviour during a borehole indentation test. 11
2.5 BHJ strength vs. ice temperature, a collection of former results. 11
2.6 Example of five different failure behaviours. 12
2.7 Example of sawtooth failure mechanism 13
2.8 Vertical thin section from indentation test 14
2.9 Example of temperature effect on the force-time curve. 15

3.1 Overview map showing the locations for all the testing areas. 18
3.2 Pictures of the borehole jack. 19
3.3 Ice drill together with two types of handle mechanisms. 20
3.4 Pictures of a dismounted BHJ. 20
3.5 Sketch of the BHJ 21
3.6 Picture and sketch of the reinforcement ring. 22
3.7 Free body diagram of the triangle and the piston in the BHJ device. 24
3.8 Experimental setup for the BHJ test. 25
3.9 Equipment for ice temperature measurements. 26
3.10 Equipment for collecting ice cores 27
3.11 Equipment used in transportation of ice cores. 27
3.12 Caliper used to measure the length of the ice cores. 28
3.13 Thin section equipment 29
3.14 Thin sections before and after milling. 30
3.15 Picture of the Russian snow penetrometer. 31
3.16 Minimum RSP index requirements for a range of tire pressure values. . . 32

4.1 Daily temperature measurements 34

4.2 Example of typical stress-time curve. 35
4.3 Average strength along the length axis of the runway 38
4.4 BHJ strength vs. ice temperature. 39
4.5 Examples of typical failure behaviours. 40
4.6 Examples of stress-time curves with sawtooth loading. 42
4.7 Examples of stress-time curves where the stress stabilized at a plateau. . . 43
4.8 Pictures of failure modes with cracks at surface. 43
4.9 Pictures of spalls produced during $blue_{10}$ tests 44
4.10 Pictures of spalls produced during $blue_{20}$ tests. 44
4.11 BHJ strength vs. spall size. 45
4.12 Pictures of the indented ice. 45
4.13 Example of a stress-time curve where number of large stress drops correspond with distinct cracking-sounds. 46
4.14 Density measurements for 10 ice cores 47
4.15 CT scan of the ice core from the eastern end. 54
4.16 CT scan of the ice core from the western end. 54
4.17 CT scan of the ice core from the patch ice. 54
4.18 SVF along the length axis for the ice cores from the eastern and western end and the patch. 55
4.19 Pore volume fraction for ice cores from eastern and western end and the patch. 56
4.20 X-ray picture of the indented ice from the bhj_7101 recording. 57
4.21 X-ray picture of the indented ice from the bhj_8103 recording. 57
4.22 X-ray picture of the indented ice from the bhj_9101 recording. 58
4.23 RSP index with depth. 60

5.1 Spatial variation of strength along the runway, including ice temperature. 63
5.2 BHJ strength vs. spall size for the $patch_{10}$ results, including ice temperature. 64
5.3 Picture illustrating sand particles left in the bottom of a patch 65
5.4 Stress-time curves of comparable BHJ recordings. 66
5.5 Failure behaviour vs. the ice temperature. 67
5.6 Plot of density measurements vs. the middle depth of each core. 70
5.7 Pictures of ts_320h with two different section thicknesses. 71
5.8 Zoomed picture of thin section ts_7101v with the corresponding BHJ stress-time curve. 72
5.9 Zoomed picture of thin section ts_8103h with the corresponding BHJ stress-time curve 72
5.10 Zoomed picture of thin section ts_9101v with the corresponding BHJ stress-time curve. 73

A.1 Explanation of symbols used in the testing area maps. I

Symbol list

Abbreviations

BHJ = borehole jack
CRREL = Cold Region Research and Engineering Laboratory
CT = computed tomography
FEM = finite element method
HPZ = high pressure zone
NPI = Norwegian Polar Institute
NTNU = Norwegian University of Science and Technology
RSP = Russian Snow Penetrometer
SVF = solid volume fraction
UNIS = The University Center in Svalbard

Roman symbols

A_{pist} = area of piston
c = indentation load factor
D = penetration depth
F_{bar} = tension force in bar
F_{pist} = force from piston into ice
F_{rec} = compressive force recorded in load cells
h = height of hammer drop
L = mean long bubble diameter
n = number of hammer drops
Q = mass of penetrometer without hammer
S = mean short bubble diameter
v = indentation rate
V_{bubble} = mean bubble size
W = mass of drop hammer

Greek symbols

$\dot{\varepsilon}$ = strain rate

$\dot{\varepsilon}_{cr}$ = critical strain rate

μ_1, μ_2, μ_3 = friction coefficients

ν = fractional porosity of ice

ρ = density

ρ_{avg} = average density for the blue ice

σ_1, σ_2, σ_3 = principal stress

$\sigma_{blue,10}$ = strength of *blue,10* ice

$\sigma_{blue,20}$ = strength of *blue,20* ice

$\sigma'_{blue,20}$ = strength of *blue,20* ice when recording bhj_7301 is excluded

σ_{ice} = stress in ice indented by piston

$\sigma_{patch,10}$ = strength of *patch,10* ice

Chapter 1

Introduction

Troll is a Norwegian research station located in Queen Maud Land in Antarctica, operated by the Norwegian Polar Institute (NPI). The station experienced great improvements in 2005 when it was decided that the station should be attended during the winter in addition to the summer. These improvements included among others a 3 km long runway. This airstrip is quite unique in sense of its construction material, which happened to be glacier ice. Typical techniques and tools developed to characterize the runway strength are normally designed for materials like concrete and asphalt. Runways located on ice require therefore unconventional techniques to assess the strength of the pavement.

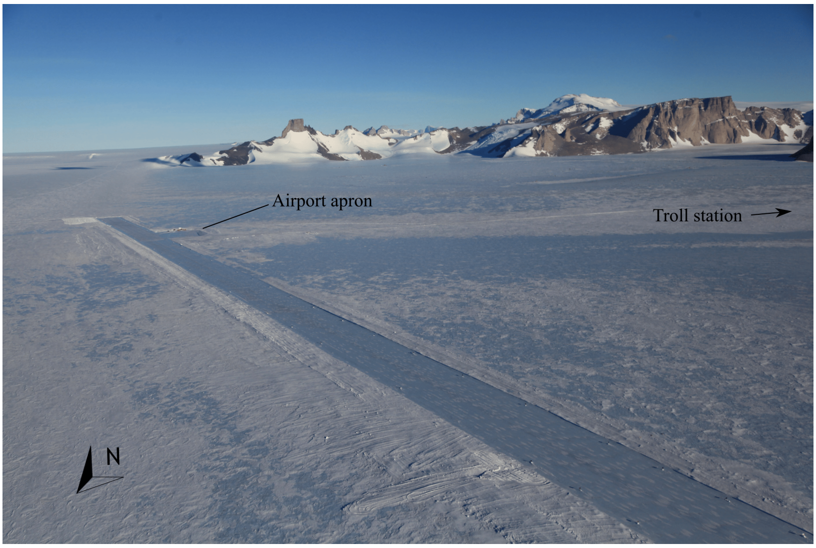

Figure 1.1: Overview picture of the 3 km long runway at Troll Airfield. The airport apron can be seen in the eastern part of the runway. The north pile gives the orientation.

Troll Airfield are facing challenges related to so-called cryoconite holes. These holes are a result of dark particle accumulation on the glacier surface. At Troll Airfield, these particles are wind-transported sand material from the surrounding mountains. The dark colour implies that the material has a low albedo and absorbs heat from the sun radiation. Melt holes can therefore be produced for temperatures below 0°C.

Obviously, there can not be melt holes on a runway surface. The personnel at Troll Airfield spend hours during the summer season on repairing the ice. This is done by hacking the refrozen melt water and removing all the sand particles in the hole. It is important to remove *all* the particles because whats left in the bottom of the hole can absorb sun radiation through the ice, and the melting can initiate from the bottom and up. Afterwards, the hole is refilled by a mixture of crushed ice and water to imitate the colour of the surrounding ice. This method is called the patching method and has been successfully applied for many years (Sund and Guldahl, 2007).

1.1 Research questions

But how strong is this patch ice compared to the glacier ice? And is there a significant difference in the general characteristics of the two types of ice which together constitute the runway surface? These questions are concerns for the Troll Airfield personnel, and will be the research topic of this project.

The objectives of this master thesis are concretized later in this introduction. But first will the testing site and field work program be presented.

1.2 Testing site

The Troll station is located in a blue ice area in Queen Maud Land. The station was established in 1989-90, and was initially attended only during the summer season. It is situated 72°S and 2°40'E, 235 km from the ice shelf margin and elevated 1200 m.a.s.l. The station, in contradiction to the airfield, is established on solid ground by the foot of the mountain Jutulsessen. This mountain is part of a large range of nunataks running parallel to the shore line.

The Troll Airfield is placed directly on the glacier ice, about 7 km away from the station. The runway is 3 km long, and stretches from east to west. The picture in Fig. 1.1 shows almost the hole length of the runway, and a map of the area is given in Fig. 1.2. The airport apron is the loading and parking area for aircrafts while stationed at Troll.

The Troll Airfield is a busy airport compared to others located in Queen Maud Land. The summer season 2017/18, 10 intercontinental flights were scheduled and 22 feeder flights used the airfield for tanking. Intercontinental flights put more requirements on the ground personnel, and Troll Airfield is one out of two airports in Queen Maud Land who meets these specifications. NPI wants their airport to function as a gateway from Antarctica to Cape Town for the other research stations in the area. Embedded in this strategy is an improvement of the runway monitoring program.

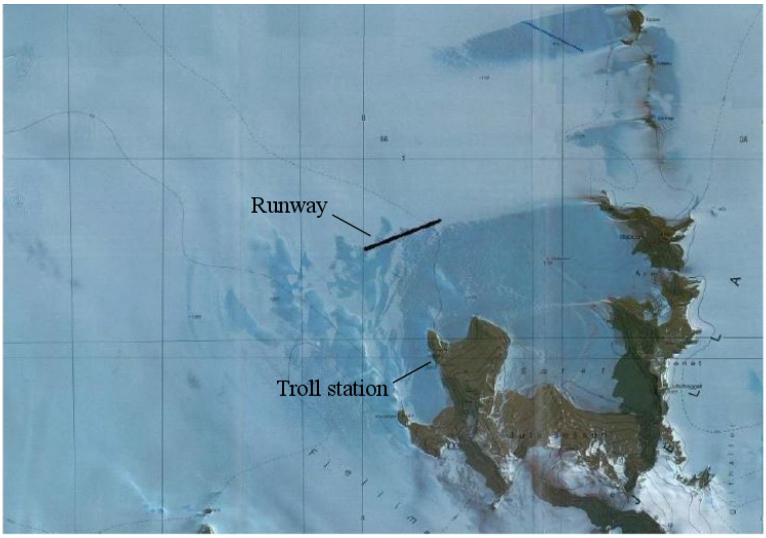

Figure 1.2: Map of the area around the Troll station. The 3 km long airstrip is marked with the black line. The station is located on solid ground 7 km away from the runway (in courtesy of Sund and Guldahl (2007)).

1.3 Field work program

All the investigations of the runway strength was performed by the author of this master thesis in February 2018. During this period, two experiments were conducted; an indentation test and a penetration test. In addition, ice cores were sampled and brought back to NTNU in Trondheim for further investigations of the physical properties of the ice.

The indentation test was performed by use of a newly developed borehole jack (BHJ). This device measures the required force to indent a piston into a borehole wall. The design of this particular BHJ stands out when it comes to weight and functionality. The old equipment, used by students at the University Centre in Svalbard (UNIS), weighted about 100 kg and required two or more people to maneuver it. In contrast is the weight of the new BHJ only 15 kg and it can therefore be handled by one person alone.

The penetration test was developed by the Russian Arctic and Antarctic Research Institute, and they named the testing device "Russian snow penetrometer" (RSP). The RSP consists of a steel rod with a sharp tip, an anvil located mid-height and a hammer which can slide along the upper part of the shaft. The test provides a hardness index based on number of hammer drops needed to obtain a certain penetration depth. This testing procedure is extensively used at for instance the newly opened Phoenix Airfield in Antarctica. Detailed manuals are provided by CRREL, and required minimum hardness number is given for different tire pressures.

The transportation of the ice cores was made possible by a heavily isolated freezer with several cooling elements. Both samples of the blue ice, patch ice and the indented ice after a BHJ test was collected. At NTNU, the ice was investigated through thin sections and a CT scan.

1.4 Objectives

This master thesis is initiated by NPI, with the aim of doing a comprehensive survey of the runway ice. In that is an investigation of the ice strength and the physical properties essential. Moreover is the patch ice of particular interest. The patching method has been successfully applied to repair melting holes at the runway surface for many years, but there exist no documentation of the characteristics of the patch ice. Strength values for both the blue ice and the patch ice are measured using the BHJ and the RSP. A correlation between the to testing methods is wanted because the testing procedure for the RSP is much simpler compared to the BHJ.

Increasing flight traffic demands a system for monitoring the runway strength. With this in mind will an assessment of the relevance of the experiments and the user-friendliness of the equipment be given.

The BHJ is recently developed, and a description of the equipment is presented in Chap. 3.2. The indentation mechanism will be studied in detail, where the goal is to derive a relationship between the measured force and the indentation force.

The BHJ failure behaviours for the blue ice and the patch ice will be studied and compared to one another and to literature. The blue ice is tested at different depths, and the evolution of strength, failure behaviour and structure with depth will be investigated.

1.5 Literature

Ice mechanics have been extensively investigated in recent time due to the increasing activity in the Arctic regions. Numerous field work and laboratory programs have been conducted with the objective of examining the ice strength and how it is related to various parameters. Schulson and Duval (2009) have collected the most important publications in a book called "Creep and Fracture of Ice", and the results in this book will be widely utilized in this thesis.

There exist little literature about the strength of *glacier* ice in particular. Yet, as long as the physical properties of the glacier material is known, reliable estimates of the mechanical strength can done based on the literature of ice with similar structure.

Publications of small- and medium scale indentation experiments have been reviewed. In these papers, the confined ice strength has been related to both indentation rate and ice temperature through series of laboratory experiments, and the modified ice adjacent to the indentor is studied through thin sections. However, similar studies of the failure behaviour and the damage of ice for the experiments conducted in the field are not found.

Chapter 2

Theory

2.1 Glacial ice

Glacial ice has a granular structure consisting of a mixture of single grains and aggregates of several. The content of air bubbles is relative high, varying between the different stages in the glacial formation process. Glaciers exist in areas where the accumulation of snow during a winter is larger than the melting during the summer. Layers of snow on top of each other will eventually constitute a large pressure on the underlying snow, and this is the driving factor in the transformation of snow into ice. The snow recrystallizes and form equally sized grains. The intermediate state between snow and ice is called firn, which is a type of porous ice with density of ca. two third of water density. Firn is said to turn into ice when the pressure is high enough to cut off the interconnecting air- or water-filled passages between grains. The air exists in the ice in form off air bubbles, and further densification of the ice will be driven by bubble compression (Cuffey and Paterson, 2010). The maximum density of ice is 916.4 kg m^{-3} for 0°C, which is a condition with no air in the ice (Hobbs, 1974).

Typical densities for snow, firn and glacier ice are given in Tab. 2.1. Glacier ice will be referred to as "blue ice" in the following because of the blue appearance of the ice when the surface snow is removed and the ice becomes visible (Cuffey and Paterson, 2010).

Table 2.1: Typical densities for the snow, firn and glacier/blue ice [kg m^{-3}] (Cuffey and Paterson, 2010).

New snow	50 - 70
Settled snow	200 - 300
Wind packed snow	350 - 400
Firn	400 - 830
Glacier ice	830 - 923

To sum it up, glacier ice is formed by compression of snow. Thereby, one would expect the structure to be isotropic. Isotropy is referring to a random orientation of the ice crystals on a molecular level. Water molecules are organized in layers of hexagonal ring structures with six molecules in each ring. The layers are called basal planes, and the normal to the planes are defined as the c-axis. The contradiction to the isotropic structure is an anisotropic structure, which means that the c-axis are oriented parallel to each other. This alignment implies that the mechanical properties depends on the testing direction. The movement of a glacier might effect the direction of the basal planes through plastic deformation and result in some degree of c-axis alignment. Hence, the glacial ice might be anisotropic (Schulson and Duval, 2009).

2.2 Physical and mechanical properties of granular ice

The strength of fresh-water granular ice is mainly dependant on temperature, grain size and strain rate. The effect of each parameter is given in this chapter. In addition, the possible effect of air bubble density on the strength will be presented because of the high content of pores in glacier ice. The stress state during loading effects the failure process and provides different values of the maximum loading pressure. The effect of confinement is discussed, and relevant failure processes will be presented. A short description of the optical properties which is relevant for thin sections will also be given.

2.2.1 Scientific strength parameters

Temperature and grain size

The compressive strength of unconfined ice increases with approximately 0.3 MPa pr. °C for temperatures in the range of 0 to -50 °C. The strength is also said to be inversely proportional with increasing grain size. Cracks nucleate along the grain boundaries, and larger grains result in larger initial "flaws" (Schulson, 1990).

It must be noted that the initial crack openings are tensile failures, and that the temperature and grain size is essentially effecting the tensile strength. In light of this one can say that the temperature and grain size effects described above has an indirectly effect on the compressive strength.

Bubble density

According to Gagnon and Gammon (1995) will the flexural strength of iceberg and glacier ice increase linearly with bubble density. The flexural strength is an engineering parameter which gives an indication of the tensile strength (Timco and Weeks, 2010), and will therefore effect the compressive strength indirectly. The resulting curve from the field work of Gagnon and Gammon (1995) is given in Fig. 2.1. The bubble density is defined as the number of bubbles per unit volume, and is calculated as follows:

$$\text{Bubble density } = \nu \cdot 1\ \text{mm}^3 / V_{bubble}, \tag{2.1}$$

where v is the fractional porosity of ice defined as the percentage volume of air within an ice sample. V_{bubble} represents an estimate for the mean bubble size, and is given by

$$V_{bubble} = \frac{4\pi}{3}(S/2)^3 + \pi(L-S)(S/2)^3, \tag{2.2}$$

where S is the mean short and L is the mean long diameter of the bubbles in the ice specimen. The bubble volume is calculated as a sum of a sphere and a cylinder.

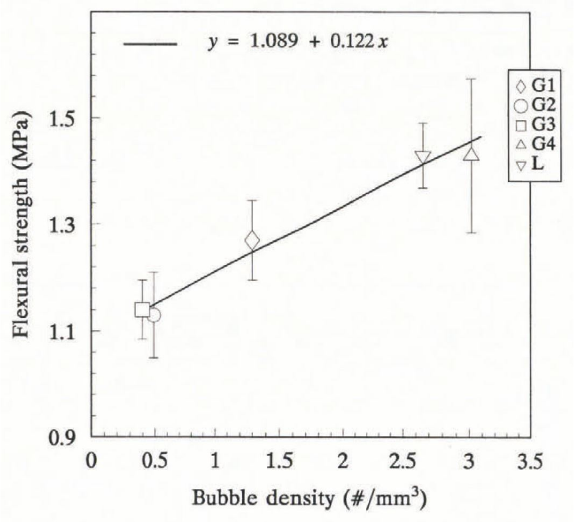

Figure 2.1: Flexural strength vs. bubble density for iceberg and glacier ice from five different locations. All tests are conducted with a strain rate of 10^{-3} s^{-1} and at temperature -7°C (Gagnon and Gammon, 1995).

Ductile and brittle failure

Ice exhibits either ductile or brittle behaviour, or a mixture, during a loading sequence. The ice is said to fail in a ductile manner when the ice experiences large deformation without significant increase in stress. The stress-strain curve is characterized by a smooth rise in the stress before it levels off or descent towards a plateau. Brittle behaviour is characterized by a sudden failure without warning. The stress-strain curve rises pseudo linearly before it suddenly drops to a lower stress level (Schulson and Duval, 2009). Examples of such curves are given in Fig. 2.9.

2.2.2 Failure processes

The failure process of ice is strictly related to the stress state. Uniaxial stress is the simplest case, where the ice is loaded in one direction only. The relevant failure process is then initiated by formation of primary cracks along the grain boundaries. At the tip of the primary crack there will form secondary cracks, so-called *wing cracks*. The wing cracks are directed parallel to the loading direction. Terminal failure stress is reached when the wings have propagated all the way to the ends of the specimen (Schulson and Duval, 2009).

If the confining pressure increases, the propagation of wing cracks are restricted. The effect of increasing confinement can be seen in Fig. 2.2. The figure is taken from Schulson and Duval (2009) and shows results from triaxial tests performed on granular ice of ~1 mm grain size at -11.50°C (Jones, 1982) and -40°C (Rist and Murrell, 1994), for a variation of confining pressure. The maximum stress represents the strength of the ice. It is evident from the plot that the difference between the maximum stress (σ_1) and the confinement stress increases mostly for lower degree of confinement, especially for -40°C. The strengthening effect of the confinement stabilizes for higher confining pressures.

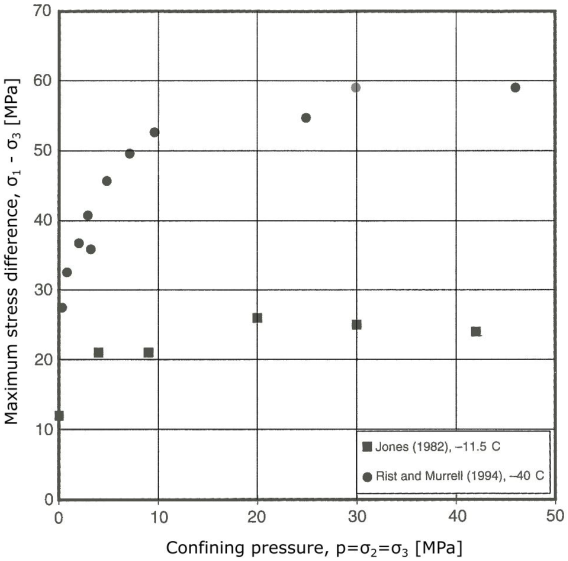

Figure 2.2: Maximum differential stress vs. confining pressure for manufactured fresh-water granular ice with 1 mm grain size and strain rate of 1 10^{-2} s^{-1}. The squares and the circles represent tests performed at -11.5 and -40°C, respectively. σ_1, σ_2 and σ_3 are common symbols for the principal stresses (in courtesy of Schulson and Duval (2009)).

The stress situation described above is called triaxial loading because the ice is loaded in three different directions. The supressing of wing crack propagation results in new failure processes. Dependant of the degree of confinement, the compressive shear fault is either described as a *Coulombic fault* or a *plastic fault*.

For lower degrees of confinement, the Coulombic shear fault in Fig. 2.3b is relevant. Initially, several short wing cracks form along the whole length of the primary cracks and is oriented parallel to the maximum principle stress referred to as *comb cracks*. The comb cracks fail first near-surface, and by further loading will the fault propagate through the specimen with an inclination of approximately 25°-30°. Sliding along this fault is compared to sliding along a rough surface, where the terminal failure is impeded by the internal friction (Renshaw and Schulson, 2001).

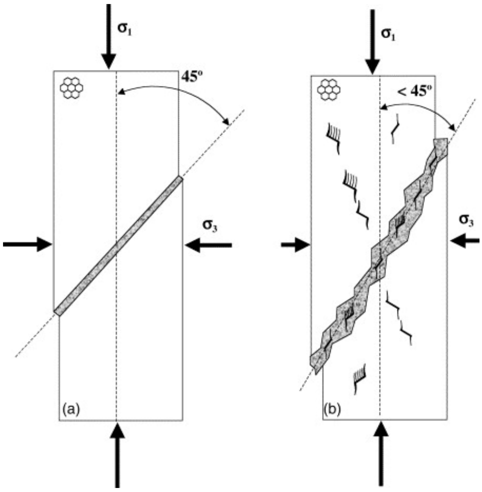

Figure 2.3: Illustrations of the two kinds of compressive shear faults for confined ice. (a) Plastic fault, which is relevant for higher degree of confinement. (b) Coulombic fault, for lower degree of confinement. (In courtesy of Schulson and Duval (2009))

For higher degrees of confinement, the plastic fault in Fig. 2.3a is relevant. This fault occur when the confinement is great enough to suppress frictional sliding along the Coulombic shear fault, and the fault is ascribed to localized plastic flow (Schulson and Duval, 2009).

Confined ice processes a remaining strength after terminal failure, especially when Coulombic faults have developed in the failure process. Upon further loading, the behaviour of the material is dependant on the prior loading history of the virgin material. This is also reflected in the sounds produced during the faulting. If the deformation is applied slowly, the failure will occur in a ductile-like manner and no sounds can be heard during the conduction of the test. On the other hand, the ice will be quite noisy if the deformation is applied rapidly (Fortt and Schulson, 2007; Schulson and Duval, 2009).

2.2.3 Optical properties

Ice structure is commonly studied by making so-called *thin sections* of the ice. This investigation method utilizes the optical properties of ice.

The electromagnetic vibrations of normal light moves in all direction perpendicular to the lightning direction. Whenever such light passes through a polarization filter, the vibrations are restricted to one plane. Further, if the same light beam passes trough another polarization filter oriented perpendicular to the first, no light will pass through the last filter. The light is completely extinguished because the plane light beam through the first filter has no component in the perpendicular direction.

However, if an ice crystal is placed in between the two orthogonal directed filters, the optical properties of the ice will alter the direction of the polarization, and coloured ice crystals can be seen. When a light beam is passing through the ice crystal, the beam is broken up in two new waves. One is parallel with the c-axes and the other one is perpendicular to the c-axes. These two new waves will then have a component in the direction of the second polarization filter and reveal colours dependant on the orientation of the c-axis. The c-axis is often referred to as the optical axis of ice (Hobbs, 1974).

2.3 Indentation failure

The indentation test is an experimental method to determine the confined strength of a material. It is an easy method to conduct, and is directly related to engineering challenges (Schulson and Duval, 2009). However, there are little control of the actual stress and strain situation in the contact area, which makes interpretation of the results challenging.

Schulson and Duval (2009) describe the failure mechanism during an indentation test as a combination of Coulombic and plastic faulting. The indented area which will be effected by this faulting is commonly described in terms of high-pressure zones (HPZs). The indentor load is often localized in smaller zones because fracture processes reduce the contact area. The pressure in these zones is thereby increased. The state of stress in the contact area is triaxial with highest degree of confining pressure near the centre of these HPZs. The regions near the edges of the zones experience a lower degree confinement, yet a great amount of shear stress (Wells et al., 2011). Therefore is the Coulombic faulting the prevalent failure mechanism along the edges of the HPZs, and plastic fault dominates near the center.

2.3.1 Borehole ice strength value

A borehole jack (BHJ) is a device which is used in indentation tests. Moreover, it has been used to characterize the *in situ* strength of ice, also called the borehole ice strength (Timco and Weeks, 2010). The main advantage of this test is that the tested ice is not removed from its original locations, hence, the *in situ* strength is obtained.

Yet, the complexity of the stress state must be kept in mind in the assessment the obtained strength values. Directly comparison between the strength values obtained from BHJ tests and from triaxial experiments conducted in laboratory is challenging. Sinha (2011) goes so far as calling the BHJ strength an "index".

Furthermore, he presents a diagram (see Fig. 2.4) of four common stress-displacement curves and suggests a strength definition for each curve. For the upper yield, asymptotic and premature failure curves, the strength is defined as the maximum recorded stress. The load in the flow stress curve, on the other hand, is continually increasing, and a maximum value will not be obtained. The strength is therefore defined as the stress after a certain amount of displacement, similar to the "yield strength" used for metals.

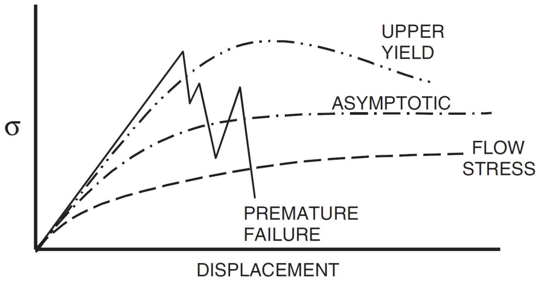

Figure 2.4: Four common types of failure behaviour for ice during a borehole indentation test. A strength definition is suggested for each curve, respectively (in courtesy of Sinha (2011)).

Temperature effect on BHJ strength

Fig. 2.5 shows a plot of the BHJ strength vs. ice temperature (Johnston et al., 2003). These measurements are collected from several different field programs conducted on saline ice floes. It appears from the plot that the ice temperature has a significant effect on the strength for tests performed on tempered ice above -5°C. Measurements done for lower ice temperatures show a considerable scatter in strength values, even for identical ice as the Ice Island measurements. They are performed on ice with the same microstructure, salinity and density. This variation is explained by the stress-rate effect which becomes important for cold ice experiments (Sinha, 1991).

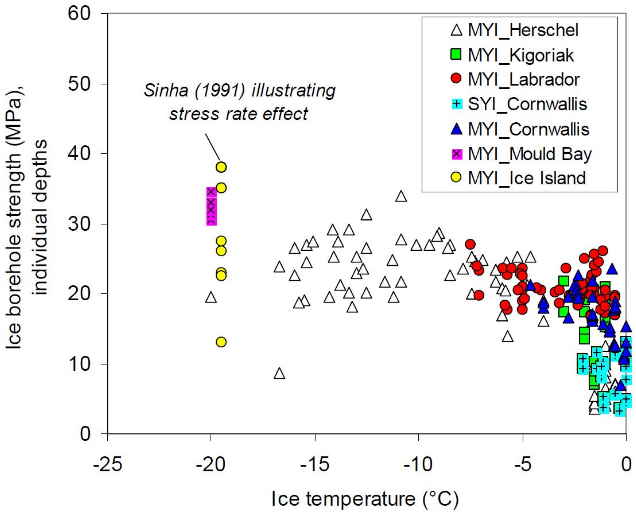

Figure 2.5: BHJ strength vs. ice temperature. Results are collected from various field programs on sea ice. The thickness of the floe vary from 1.7 to 18 m and the salinity vary from 0 to 6.2 ‰. The plot shows that the ice temperature is effecting the BHJ strength mostly for warmer ice (in courtesy of Johnston et al. (2003)).

2.3.2 Failure behaviour in load-time curves and corresponding damage events

The load-time curves recorded in an indentation test have a large range of possible behaviours. The load is reported as either stress or force. Indantaion rate and ice temperature are loading conditions which has a strong effect on the failure behaviour and will be treated in the following. A classification system is useful to ease the investigation of the curve behaviour. Such a system is suggested by Wells et al. (2011). They performed small-scale indentation tests with indentation rates varying from 0.2 to 10 mm s^{-1} with room temperature of -10°C. Further, they describe five different behaviour patterns; ductile behaviour, localized spall, isolated crushing events, cyclic-load crushing events and mixed mode. Examples of these load traces are illustrated in Fig. 2.6. Wells et al. (2011) classified the force-time curves for every indentation test based on the appearance of the individual failure behaviours. They ranked the severity and frequency of each of the described behaviours with numbers from 0 to 3 (0 = never and 3 = frequent), and they also counted the numbers of localized spalls.

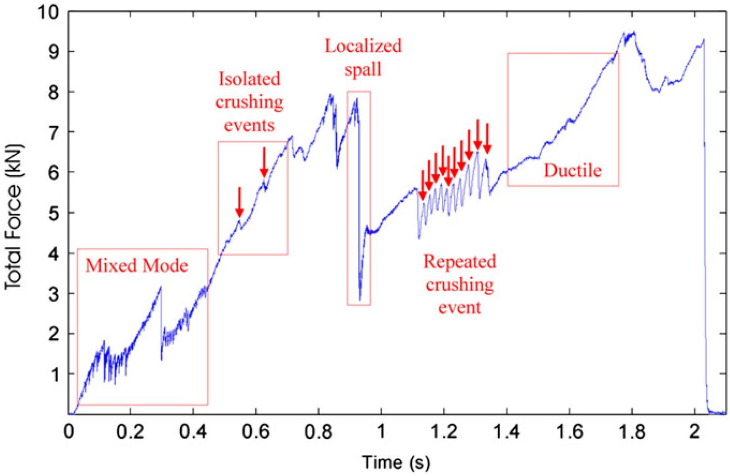

Figure 2.6: Example of five different load traces in a force-time curve (in courtesy of Wells et al. (2011)).

The following list gives a description of each failure behaviour and how the appearance is related to the indentation rate (Wells et al., 2011).

- *Ductile behaviour* is characterized by a steady rise in total force, which results in a smooth curve. The behaviour is commonly observed for slow tests with decreasing frequency as the rate is increased.

- *Localized spall* is characterized by a sudden drop in force as a result of a single flake of ice being released. The frequency and intensity of this phenomena is found to increase as the indentation rate is increased.

- *Isolated crushing events* are comparable to the localized spalls in sense of a drop in the load. However, the severity is much smaller and only crushed ice is extruded. Crushing events appear at all speeds, with the highest frequency for medium rates of 2-5 mm s^{-1}.

- *Cyclic-load crushing events* are characterized by synchronized load traces because of a dynamic activity. This crushing event is not interrupted by other failures, but followed by a localized spall. This phenomena is most frequently observed in medium rates of 2-5 mm s^{-1}, just as the isolated crushing events.

- *Mixed mode* represents an irregular pattern with a combination of small, localized spalls and crushing events. This is observed for rates above 2 mm s^{-1}, with increasing frequency as the rates are increased.

Another description of a failure behaviour observed in indentation tests is presented by O'Rourke et al. (2016). They focus on a failure mechanism called "sawtooth" loading. This loading pattern is described as a cycle of quasi-statically loading and rapid unloading, which can be very regular in its period. O'Rourke et al. (2016) performed several medium scale indentation tests with displacement rates (4-20 mm s^{-1}) chosen to induce the sawtooth mechanism. The ice temperature was constant at -10°C. Fig. 2.7 shows examples of the sawtooth loading mechanism, in which the mechanism is referred to as "Layer". Layer is the ice response to the sawtooth loading. In addition, spalls are pointed out in Fig. 2.7. Spalling is the ice response of a localized spall described by Wells et al. (2011). Both layers and spalls will be further elaborated in the following sections.

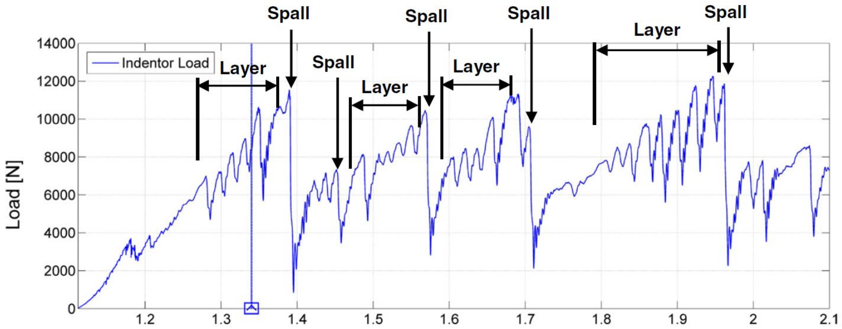

Figure 2.7: Example of sawtooth failure mechanism, marked as "Layer" in the curve. Spalls are also marked as the sudden load drops (in courtesy of O'Rourke et al. (2016)). Horizontal axis is time [s].

Layer: microstructural modification

Whenever a thin section is made of the indented ice, a zone of damaged ice can be observed in the ice adjacent to the indentor. This zone is referred to as "a layer", and the thickness seems to vary with indentation rate and penetration depth (O'Rourke et al., 2016). The damage processes which result in the formation of a layer are microstructural modifications as recrystallization and microcracking. The recrystallization is a result of the plastic faulting and will be located in the centre of the indented area because of the high degree of confinement here. The microcracks are a result of the Coulombic faulting and is found along the edges of the damage zones (Schulson and Duval, 2009; Wells et al., 2011).

The difference between recrystallization and microcracking can be seen if one study the thin sections either trough a cross polarized light or through a plane polarized light with scattered light reflected from the side, respectively (Barrette et al., 2002). This is done for the thin section photos in Fig. 2.8. Recrystallization is defined as grain refinement and the diminished grains can be seen with different colours in the cross polarized light (Barrette et al., 2002; Hobbs, 1974). According to O'Rourke et al. (2016), the recrystallization process will produce extrusion of a very fine-grained material when the sawtooth loading is obtained.

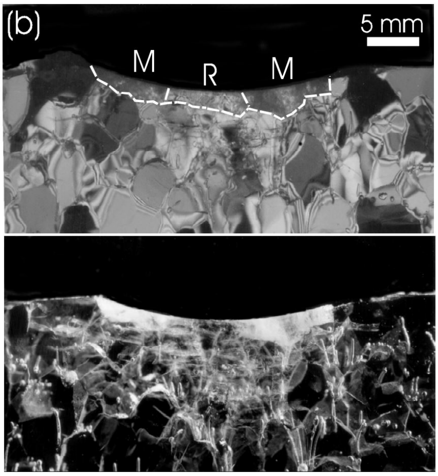

Figure 2.8: Vertical thin section of test performed at -10°C (displacement rate unknown). Upper picture are taken with cross polarized light and the lower picture is taken with plane polarized light with side light. The damaged layer are divided into R = recrystallization and M = microcracking (in courtesy of Barrette et al. (2002)).

Spall: material separation

The term "spall" is used extensively to describe distinct pieces of ice being separated from the test specimen. The mechanism for this type of brittle fracture is the release of energy through creation of a new crack surface (Wells et al., 2011). However, the size of this piece vary a lot. Spalls are often referring to smaller ice flakes being extruded from the contact area between the indentor and the ice. Yet, Jordaan (2001) uses this term for a piece of ice with 20 m in horizontal extent.

O'Rourke et al. (2016) used Trekscan pressure-distribution sensors to investigate the behaviour of the HPZs through a spalling event. They found that, in contradiction to the extrusion of crushed ice, spalling results in a relatively large reduction in the contact area between indentor and ice. They further conclude that spalling interrups a rather regular layer activity, just as the curve in Fig. 2.7 shows.

2.3.3 Temperature effect on failure behaviour and layer formation

The previous discussed articles all present results where the indentation rate is the varying parameter. However, ice temperature also has a great influence on the failure behaviour of ice (O'Rourke et al., 2015). The ice will behave in a ductile manner for high temperatures, and more brittle when the ice temperature decreases. This is investigated in particular by Barrette et al. (2002) and Browne et al. (2013).

Barrette et al. (2002) performed small-scale indentation experiments on granular, non-saline ice for temperatures at -20, -10 and -2°C. For each temperature, tests were performed at displacement rate 2, 4 and 6 mm s^{-1}. Load cycling occurrence is reported from all the tests, and so is the presence of a damaged ice layer. Further, they found that the damaged layer appeared in form of microcracking and recrystallization. For high temperature tests, recrystallization dominated as the failure mode, and microcracking for low temperatures. For tests conducted at -10°C, the damaged layer consists of a central recrystallization zone surrounded by ice with microcracks, illustrated by Fig. 2.8.

The relationship between the ice temperature and the loading pattern is investigated by Browne et al. (2013). Fig. 2.9 shows two force-time curves for ice temperature -5 and -15°C. Also he found that the failure behaviour is ductile for high temperatures and brittle for cold temperatures with increasing frequency of cyclic loading pattern for colder temperatures. Both tests were performed at indentation rate of 4 mm s^{-1}. Furthermore, they made thin sections of the damaged layer, and the failure mode distribution was similar to the result presented by Barrette et al. (2002).

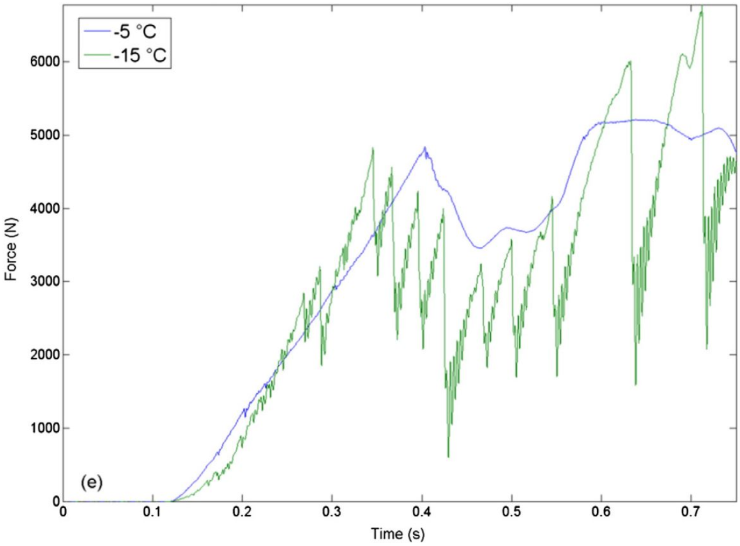

Figure 2.9: Example of temperature effect on the force-time curve. The blue curve represents the warmer ice test (-5°C) which failed in a ductile manner, and the green curve represent a cold ice test (-15°C) which failed in a brittle manner. The two tests both have an indentation rate of 4 mm s^{-1} (in courtesy of Browne et al. (2013).

Chapter 3

Experimental setup

This chapter gives a presentation of the different experiments used in the survey of the runway ice. The presentation includes a description of the experimental setup and the equipment for each test. The following experiments were conducted, where the three first were conducted at Troll Airfield:

1. An indentation test using a borehole jack (BHJ)
2. A penetration test using a Russian snow penetrometer (RSP)
3. Density measurements
4. Thin sections
5. CT scan

The two latter experiments were conducted in the cold laboratory at NTNU. To enable this, ice was collected from the runway and brought back to NTNU in a freezer. It must be noted that the CT scan was performed and analyzed by personnel at NTNU, and only parts of the results will be presented in this thesis.

But first will the organization of the different experiments conducted at Troll be presented.

3.1 Organization of the experiments

Fig. 3.1 shows a sketched map of the runway where the location for each testing area is given. The testing areas represent a group of several measurements. The map is based on the overview photo in Fig. 1.1, in which one can see the airport apron in the southwest part of the runway. The circles represent BHJ and RSP measurements, and the numbering gives the performance day and the testing site number for that particular day. For instance, testing area 7.3 was performed on day 7, and was the third are tested that day. There were in total nine testing days and the days were spread in the period from February 9. to 23.,

2018. It must be noted that the given positions are only approximations based on visual estimates. In addition, some of the testing areas range over a wider area than apparent. This holds in particular for 3.1 and the testing areas at the airport apron. Detailed maps for all the areas with the specific location for each measurement is given in Appx. A.

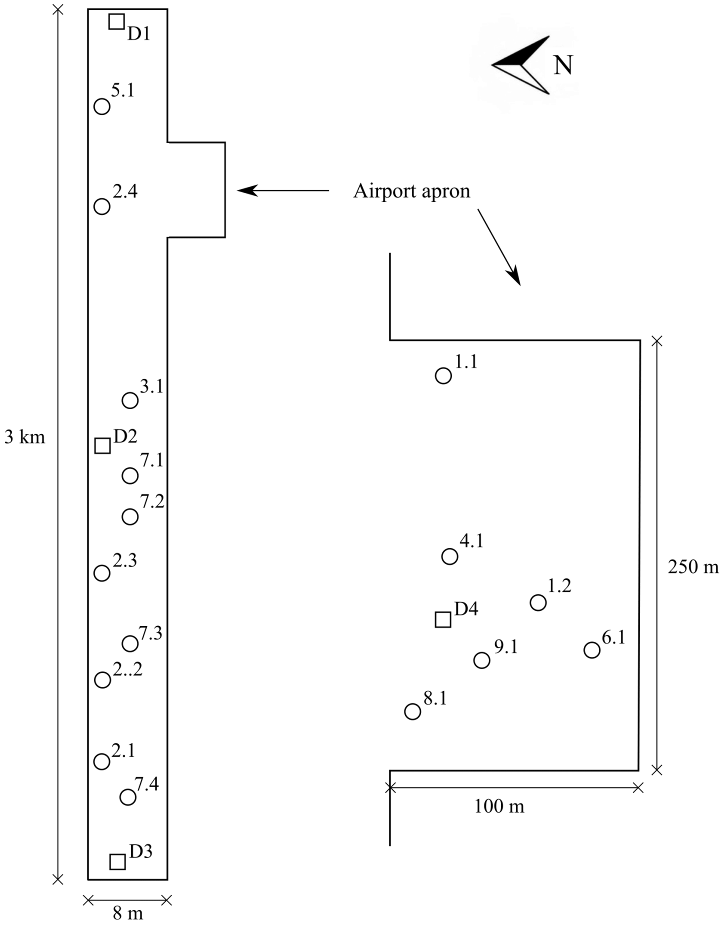

Figure 3.1: Overview map showing the locations for all the testing areas. The circles represent testing areas where BHJ and RSP tests are performed, and the first number represents day number and the second number represents the testing area that day. The squares represent areas where ice cores for density measurements are collected, numbered D1-D4.

BHJ measurements were conducted in both blue ice and patch ice to enable comparison of the characteristics of the two ice types. These experiments were grouped together in smaller areas to increase the efficiency. The RSP measurements were performed within the same areas to investigate whether there is a correlation between the two testing methods.

Additionally, ice cores have been sampled from the runway at four different locations;

the eastern, and western end, mid-way, and patch ice from the airport apron. These areas are noted D1-D4 in the overview map, and marked with squares. Samples of the penetrated ice from a BHJ experiment were also collected, and the relevant BHJ recordings are marked in the testing area maps in Appx. A.

3.2 Borehole jack

3.2.1 Equipment details

The BHJ used in this field program is recently developed, and was finished in January 2018. Pictures of the device are shown in Fig. 3.2. In short, the BHJ is composed of a steel cylinder and a piston. When a test is conducted, the cylinder is placed into a borehole, and the piston penetrates the borehole wall by power provided by a battery drill.

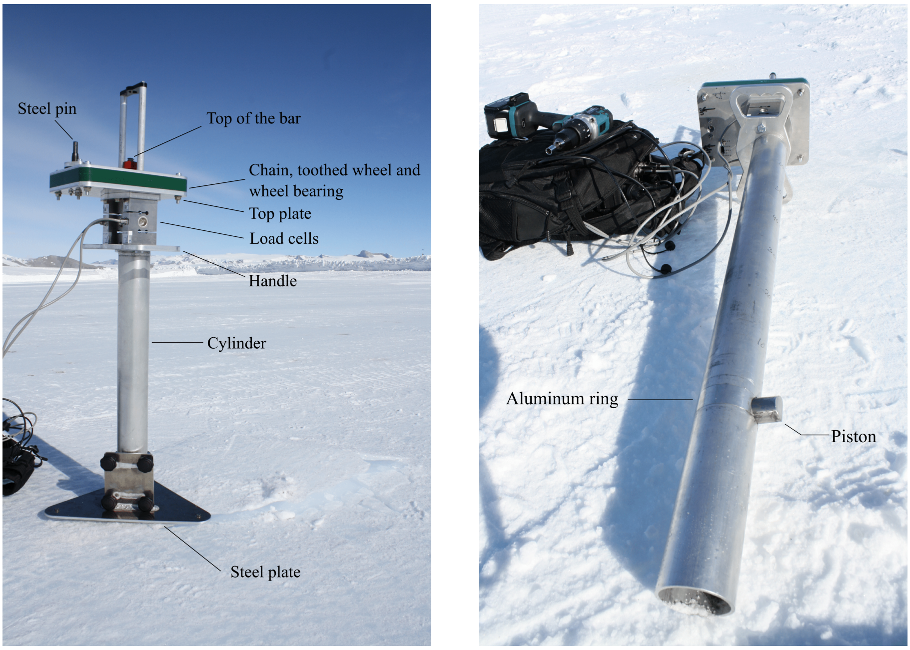

(a) **(b)**

Figure 3.2: (a) BHJ placed in borehole. (b) The BHJ with the piston fully extracted.

Fig. 3.2a shows a picture of the BHJ when placed in the borehole, and Fig. 3.2b shows the fully extracted piston. The cylinder is made of steel and the piston is made of stainless steel. The piston diameter is 30 mm, and the full stroke length is approximately 30 mm. The borehole was predrilled by an ice drill, and the borehole diameter was only slightly larger than the cylinder. The drill was at first run by hand power with use of a handle, but the blades quickly became blunt due to sand in the ice. A grip for a 18 V drill was made to ease the creation of the holes. The handle and the drill grip are shown together with the ice drill in Fig. 3.3. The steel plate seen in Fig. 3.2a ensures that the piston is located at desired depth and contributes to stabilization of the jack.

Figure 3.3: Ice drill with two types of handle mechanisms. Left: manual handle, middle: ice drill, right: grip for battery drill.

Inside the green cover in Fig. 3.2a there is a chain, a toothed wheel and a wheel bearing. Fig. 3.4 shows pictures of a dismounted BHJ where these components can be studied. The chain is connected to the steel pin, which will rotate by power from an 18 V Makita drill. Further, the toothed wheel will rotate, and so will the wheel bearing connected beneath the toothed wheel. The red item is the top of a bar located inside the wheel bearing and further down in the cylinder. This bar functions as an axle in the centre of the rotation because of the threaded surface. The bar is now being pulled upward, resulting in a compressive force from the wheel bearing onto the top plate. The mounting of all these components are illustrated in the sketch of the jack in Fig. 3.5.

(a) **(b)**

Figure 3.4: Pictures of a dismounted BHJ, showing the components located inside the green cover. (a) The steel pin, the chain and the toothed wheel. The red item is the top of the bar. (b) Wheel bearing attached under the toothed wheel.

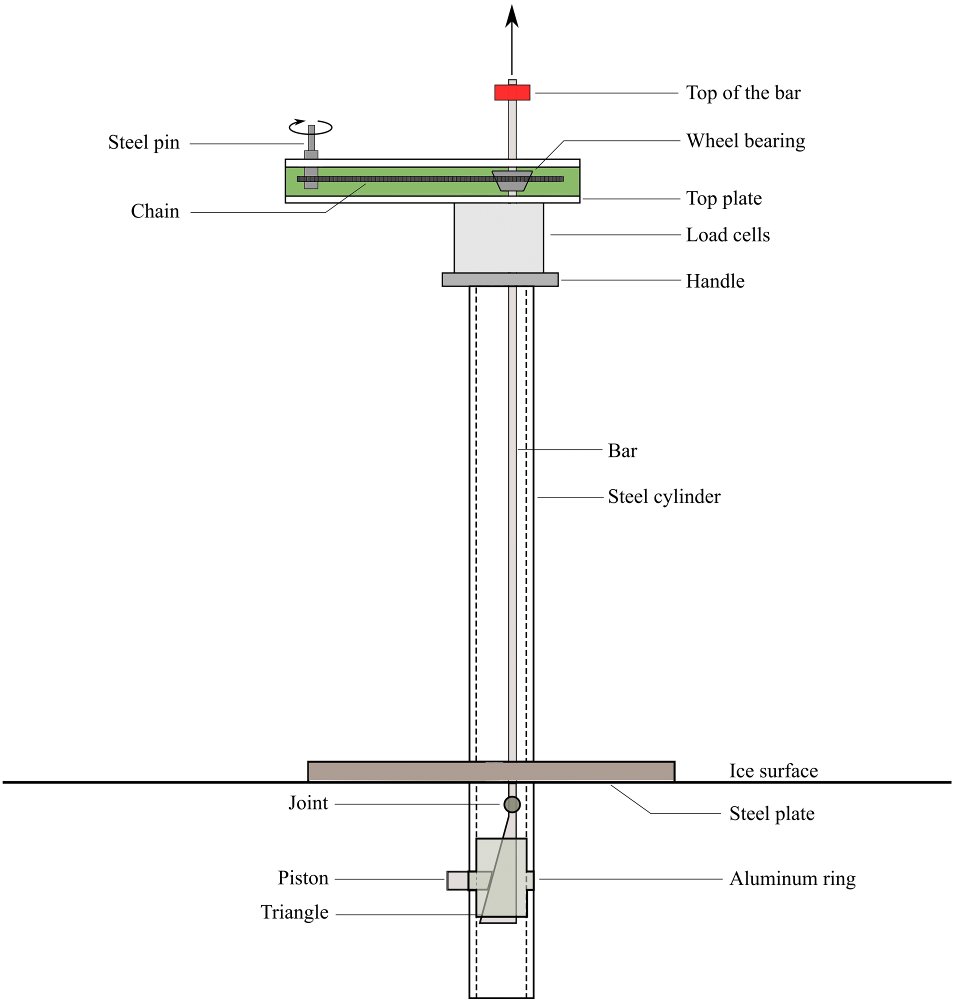

Figure 3.5: Sketch of the BHJ. When the steel pin rotates, the chain makes the wheel bearing rotate. The chain and the wheel bearing are connected by a toothed wheel cf. Fig- 3.4a. Further, the bar function as an axle located inside the wheel bearing, and is dragged upward because of the threaded surface. In the end of the bar there is a right-angled triangle. The back side of a piston is inclined equally as the triangle and will be pushed out of the cylinder when the triangle is dragged upward. This area is reinforced by an aluminum ring. The piston and the wheel bearing is producing a compressive force on the steel cylinder, and this force is recorded by two load cells located in between of the top plate and the handle.

At the very end of the bar there is a right angled triangle connected to the bar by a joint. The triangle is made of stainless steel. As it appears from the sketch, the back side of the piston is equally inclined as the triangle. There is a track along the triangle edge where the piston can slide. Further, there is a circular hole in the cylinder wall with the same diameter as the piston. When the triangle is moving upwards, the piston is pushed out of the cylinder. This motion creates a vertical force component which is transmitted to the steel cylinder. The triangle is pushed backward and a horizontal force component is created opposite directed of the piston load. Free body diagrams are given in Fig. 3.7 and are helpful illustrations.

The steel cylinder alone would not be strong enough to transfer these loads. An aluminum ring is therefore placed inside the cylinder as a reinforcement of this area. A picture and a sketch of this aluminum ring is given in Fig. 3.6. The aluminum ring has a cylindrical shape, with slightly larger diameter mid-height. The diameter here is the same as the steel cylinder, and is the only part visible when the BHJ is mounted (see Fig. 3.2b). Thereby the name aluminum "ring". Inside the ring, there are open space which allow the triangle to move upwards and the piston outwards. Otherwise is the cylinder massive, which gives a stabilizing effect to the two components. Having said that, there will be frictional forces in the contact areas, marked with red and green in Fig. 3.6b. The red friction area is a result of the vertical force component from the piston, and the green friction area results from the triangle being pushed backwards. There will also be a considerable friction contribution between the piston and the triangle. It must bu noted that all three contact areas are greased to reduce the friction, yet data of the greasing material are not given.

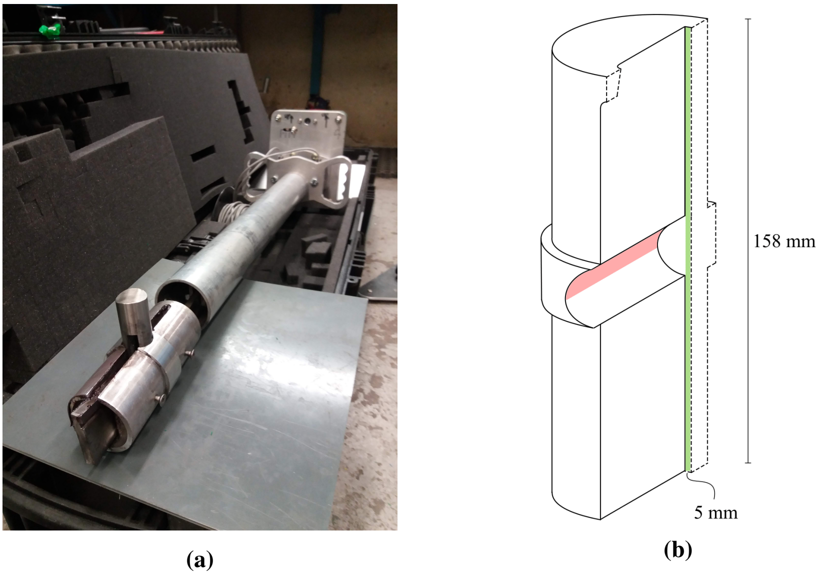

(a) (b)

Figure 3.6: Picture and sketch of the aluminum ring. (a) The picture shows the location of the triangle and piston inside the aluminum ring. There is a track along the edge of the triangle for the piston to slide along. The bottom part of the cylinder is not shown in the picture. (b) A cross-sectional sketch of the aluminum ring. The dotted lines show the cuts. The red and the green areas mark the frictional contact areas for the piston and the triangle, respectively.

The steel cylinder experiences a compressive force as a result of the wheel bearing pushing downward and the aluminum ring pushing upwards. This force is measured by two load cells located in between the handle and the top plate. The total force will be the sum of the recorded force in the two load cells. A possible skewness in the force distribution will be intercepted by a difference in the two force values. The capacity of each cell is 20 kN, and the total maximum load is therefore 40 kN. The load cells are connected to a NI compact Duq 91XX data logger. The data logger is connected to a Panasonic Thoughbook computer through an USB-cable. A Labview program provides a plot of the forces in the two load cells together with the total force. The sampling frequency is 200 Hz, which can be adjusted. The results from each test are stored in text-files, with the readings from the two load cells separate.

3.2.2 Indentation load factor

The indentation load factor (c) gives the relationship between the recorded vertical force (F_{rec}) and the horizontal force from the piston into the ice (F_{pist}). This factor is crucial if one wants to determine the strength of the ice.

$$F_{pist} = c \cdot F_{rec} \tag{3.1}$$

In this context, some simplifications had to be done. Firstly, the stress acting on the friction areas are only considered as resultant forces. In doing so, it is not taken into account that the contact surfaces vary with the piston stroke, and that the contribution from friction will vary with time and force amplitude. Secondly, it is assumed that the only friction contribution comes from the three areas listed below. For instance, possible friction between the two large triangle surfaces against the aluminum ring are neglected. Lastly, the relevant friction coefficients are only estimated from known values and not measured.

Two free body diagrams are given in Fig. 3.7, one for the piston and one for the triangle. F_{bar} is the tension force in the bar. It must be noted that the joint between the the bar and the triangle is considered as a rigid connection because the triangle can only move straight upwards. F_{pist} will be identical to F_{bar}, because all the vertical forces (F_2 and $\mu_3 F_3$) are transmitted to the cylinder. As mentioned earlier, there are three contact areas, which are numbered as following:

1. Between the the piston and the triangle, μ_1.
2. Between the upper half of the piston and the aluminum ring, μ_2.
3. Between the back of the triangle and the aluminum ring, μ_3.

μ_1 represents stainless steel vs. stainless steel and is assumed to be 0.16. $\mu_2 = \mu_3$ represent stainless steel vs. aluminum and is assumed to be 0.13. These values are estimated based on known friction coefficients between the materials for lubricated surfaces. In here, data of the greasing material would provide a more accurate estimates.

The indentation load factor (c) is theoretical derived by taking equilibrium in the vertical and horizontal direction for the triangle and the piston separately. All forces are illustrated in Fig. 3.7.

Triangle:

$$\begin{array}{lcrcl}
\sum F_V = 0 & \Rightarrow & F_{bar} & = & \mu_3 F_3 + (\mu_1 \cos\theta + \sin\theta) F_1 \\
\sum F_H = 0 & \Rightarrow & F_3 & = & (\cos\theta - \mu_1 \sin\theta) F_1 \\
 & \Rightarrow & F_{bar} & = & (\mu_3 \cos\theta - \mu_1 \mu_3 \sin\theta + \mu_1 \cos\theta + \sin\theta) F_1 \\
 & & & = & A \cdot F_1
\end{array}$$

Piston:

$$\begin{array}{lcrcl}
\sum F_V = 0 & \Rightarrow & F_2 & = & (\sin\theta + \mu_1 \cos\theta) F_1 \\
\sum F_H = 0 & \Rightarrow & F_{pist} & = & (\cos\theta - \mu_1 \sin\theta) F_1 - \mu_2 F_2 \\
 & & & = & (\cos\theta - \mu_1 \sin\theta - \mu_2 \sin\theta - \mu_1 \mu_2 \cos\theta) F_1 \\
 & & & = & B \cdot F_1 \\
 & \Rightarrow & F_{pist} & = & A^{-1} B F_{bar} \\
 & & & = & c F_{bar}
\end{array}$$

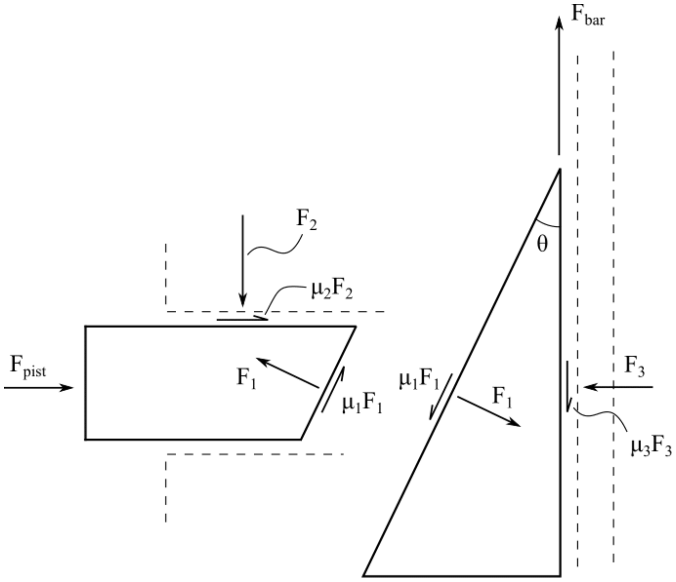

Figure 3.7: Free body diagram of the triangle and the piston in the BHJ device.

The obtained expression for c is:

$$c = \frac{\cos\theta - \mu_1 \sin\theta - \mu_2 \sin\theta - \mu_1 \mu_2 \cos\theta}{\mu_3 \cos\theta - \mu_1 \mu_3 \sin\theta + \mu_1 \cos\theta + \sin\theta}, \tag{3.2}$$

where θ is the angle in the upper corner in the triangle of 10.14°. If one include the estimates for the friction coefficients, the constant value of factor c is determined to be

$$c = 1.99 \tag{3.3}$$

It must be noted that a calibration equipment is under development. When this equipment is finished, one will get the accurate value of c. However, the theoretical derived factor in Eq. 3.3 will be used in this master thesis.

The relationship between the piston force and the stress in the ice (σ_{ice}) is given by the formula

$$\sigma_{ice} = \frac{F_{pist}}{A_{pist}} \tag{3.4}$$

where A_{pist} is the area of the piston. The piston diameter is 30 mm which gives an area of 707 mm^2.

A Matlab-script was used in the analyze of the BHJ recordings. In short, the script reads the text-file from the Labview program, summarizes the two load recordings and transforms each total load into the indentation load by use of the Eq. 3.1 and the value of c. Then, σ_{ice} is calculated from Eq. 3.4. The output is a stress-time curve and the maximum recorded stress value in each plot.

3.2.3 Experimental procedure

The experimental setup used in the field for this test is shown in Fig. 3.8. The grey cable between the load cells and the data logger was very long, and was therefore spun around a coil. The coil, together with the data logger, were put into the black backpack leaning against the sledge. This eased the transportation from one hole to another, and made it possible for one person to do the job alone. The data logger was connected to the computer through an USB-cable, which was detached when the BHJ was moved between boreholes.

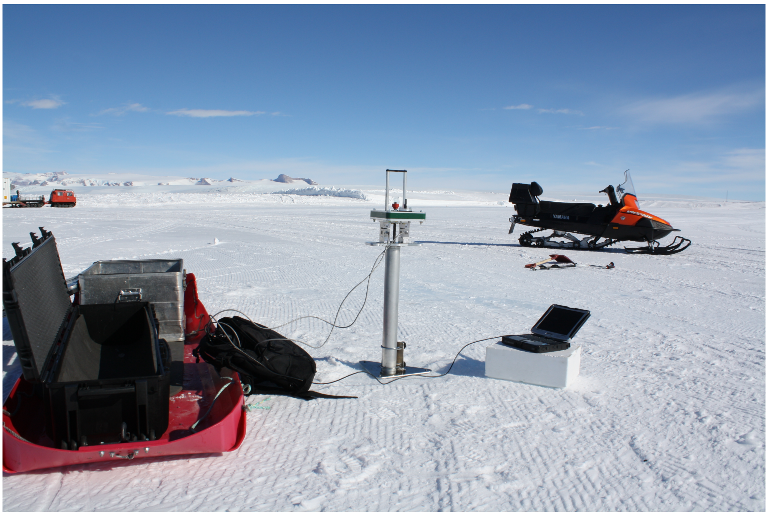

Figure 3.8: Experimental setup for the BHJ test.

Observations done during the conduction of the BHJ tests were noted, and almost all failure modes were photographed. The notes included different sounds one could hear during the indentation and whether the ice was lifted or not. Often largeer spalls were produced, and the size of these spalls are measured as the length from the borehole to the crack furthest away. When the patch ice is tested is the diameter of the patch noted. It must be commented that the notes became more systematic during the field work period.

The last step in the BHJ experiment was the ice temperature measurement. Fig. 3.9 shows the equipment used for this purpose, which was a ebos TFX 422 Pt1000 thermometer and the same Makita battery drill used for the BHJ recording. A twist drill bit was used to make a small hole into the borehole walls at depth 10 cm. The tip of the thermometer, which was slightly slimmer than the bit, was put into the wall. The ice temperature stabilized after about a minute, depending on the prior temperature measurement. For tests performed at depth 20 cm, it was challenging to reach down to the same depth. Therefore were most of these temperature measurements done at depth 10 cm.

Figure 3.9: The thermometer and the drill bit is used for ice temperature measurements. The tip of the thermometer is stuck into a hole in the ice made by the drill bit.

Notes regarding the weather type were also done at least one time each day. Information about the air temperature is collected from a weather station nearby the runway.

3.3 Collecting ice core samples

Ice cores samples of the blue ice were collected at three different locations along the runway: western and eastern end and midway. One ice core was collected from a patch at the airport apron. In addition, ice cores of the indented ice from five different BHJ experiments were collected.

The ice core sampling was done by use of a Kovacs drill with 75 mm diameter. An Rigid 690-l Hand-held Power Drive was used to rotate the core sampler, and the power was provided by a Honda EU20i portable generator. The generator and the Kovacs drill are shown in Fig. 3.10a and an example of an identical bolt threading machine is shown in Fig. 3.10b.

(a) **(b)**

Figure 3.10: Experimental setup and equipment for collecting ice cores (a) Kovacs drill used for ice core sampling and the generator providing electrical power. (b) Bolt threading machine used to rotate the core sampler.

The density of each ice core was measured by a commonly used mass/volume method, which will be presented in the following subchapter.

(a) **(b)**

Figure 3.11: Equipment used in the transportation of ice from Troll station to NTNU in Trondheim. (a) Cool-Ice freezing box (b) Indented ice specimen in a plastic cup.

A selection of the collected ice was brought back to NTNU for further investigations, including thin sections and CT scanning. The ice cores were put into small plastic cups and stored in a Cool-Ice freezing box during the transportation, see Fig. 3.11. The freezing box is heavily isolated and was stacked with cooling elements. The box is able to keep the temperature below $-6°C$ for approximately 40 hours if the whole system has an initial temperature below $-18°C$. Fig. 3.11b shows an examples of an ice core of the indented ice which was also brought back to Trondheim. One can clearly see the piston mark in the ice core.

In total 9 plastic cups with ice core samples were brought back to Trondheim. The core length varied from 1 cm to 7 cm, depending on how successful the ice core sampling was. The content of the cups are listed in the following. The given depths are approximations of the mid-height depth for each core.

- Eastern end, depth 10 cm
- Eastern end, depth 20 cm
- Midway, depth 5 cm
- Western end, depth 10 cm
- Western end, depth 20 cm
- Pathing ice, depth 10 cm
- 3 thick sections of indented ice from bhj_8101, bhj_8102 and bhj_8103.
- Indented ice from bhj_7101
- Indented ice from bhj_9101

3.3.1 Density measurements

The mass/volume method is commonly used to determine the density of ice specimens, and the formula is given in Eq. 3.5 (Pustogvar and Kulyakhtin, 2016). For the case where the ice specimens have a cylindrical shape, the volume measurement (V) includes only length measurement because the diameter is known for the Kovacs ice dill (here: 75 mm). The length was measured by use of a caliper as shown in Fig. 3.12. The ends of the cores were cut with a handsaw. A PCE group BT2000 electrical weight was used to measure the mass (m) of the ice cores.

Figure 3.12: Caliper used to measure the length of the ice cores after the ends are cut.

$$\rho = \frac{m}{V} \tag{3.5}$$

3.4 Thin sections

There exist different procedures for making thin sections of ice. The method used in this master thesis is explained in short: One side is polished and glued to a glass plate and the other side is milled until the section is thin enough. The thin sections were made in a cold laboratory at NTNU with a room temperature of ∼ -12°C.

More detailed, an approximately 1 cm thick ice slab was cut out from an ice core using a stationary belt saw. These slaps were either a horizontal or vertical cross section of the ice. One slab surface were then sanded down and polished. A 10 x 10 cm glass plate was gently heated to ∼ 50-60°C using a VWR hot plate located inside the cold lab. The ice slab was glued to the heated glass plate by pressing the polished surface of the ice against the plate. The resulting melt water function as glue when it froze. The compression lasted until the water was almost frozen and then left a few more minutes to ensure proper fastening.

Then the glass plate was attached to a Leica 1400 microtome to enable milling of the ice section, see Fig. 3.13a. A Vacuubrand membrane-vacuum pump ensured good fixing between the microtome and the glass plate. A sharp Leica 25 cm/c blade was installed at the microtome, and the desired sharpening angle had to be fixed.

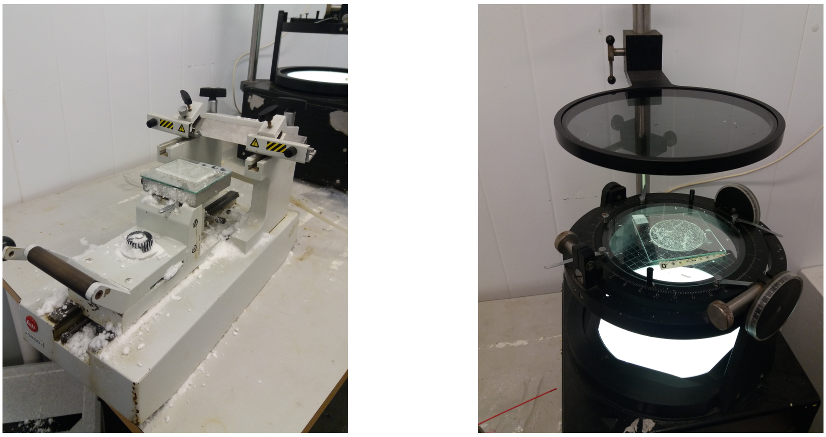

(a) **(b)**

Figure 3.13: Thin section equipment. (a) Microtome knife. (b) lamp with two crossed polarization filters

When satisfying thickness was reached, the thin section could be studied when it was placed in between two crossed polarization filters and light was passing through, see Fig. 3.13b. The observed colours revile the orientation of the crystals as explained in Chap. 2.2.3. The colours were documented through photographs.

Fig. 3.14 shows a picture of a final thin section with a thickness of 0.5 mm. In the background there is a thin section before milling.

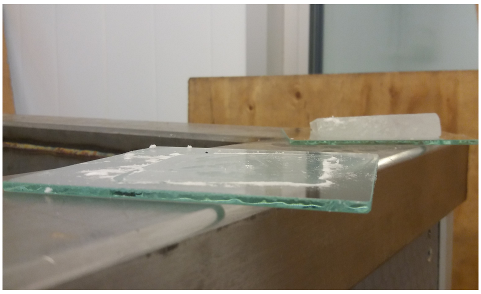

Figure 3.14: Thin sections before (in the background) and after milling.

3.5 CT scanning

The CT scan performed at the laboratory at NTNU is an X-ray computed microtomography scan which provides cross-sectional pictures of the hole ice core. CT is short for computed tomography.

The ice cores are composed of ice material with small air bubbles and a few sand grains. These materials all differ in the degree of absorption of the X-raying, mainly because of the difference in density. During a CT scan, about 3000 X-ray pictures are taken sideways while the core rotates. These pictures contain information about the degree of absorption in every little piece of the ice core when put together. Thereby, information about the material composition for the hole ice core is obtained when the pictures are combined. This makes it possible to reconstruct 2D pictures of every cross section in the core (both horizontal and vertical), or further, a complete 3D figure of the ice core.

3.6 Russian snow penetrometer

A Russian snow penetrometer (RSP) is a device used in a penetrating test of the ice surface. The equipment consists of a steel rod with a sharp cone tip, an anvil located about mid-height at the rod and a cylindrical weight (hammer) which smoothly slide along the upper portion of the penetrometer shaft. The total length of the penetrometer is 114 cm and it has a diameter of 11 mm. The cone tip has an angle of 30°. The weight of the hammer is 1.76 kg and the maximum sliding length is 50 cm. The penetrometer without the hammer weight 1.61 kg. Pictures of the RSP is shown in Fig. 3.15.

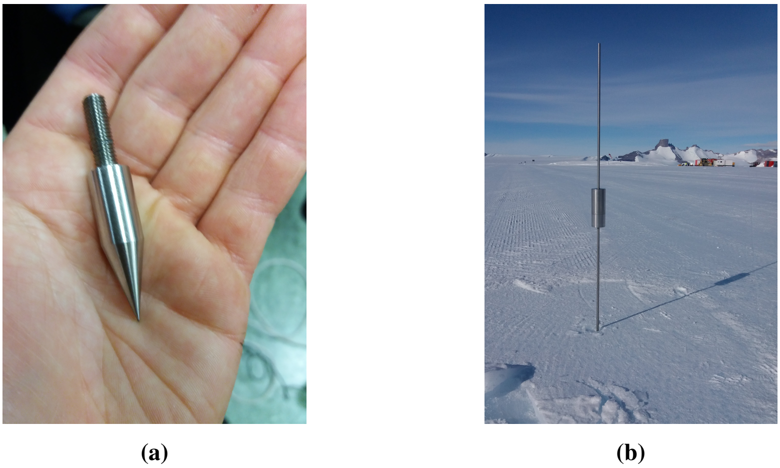
(a) (b)

Figure 3.15: Pictures of the Russian snow penetrometer. (a) The tip of the RSP, hold in hand for scale. (b) RSP when tip is inserted into the ice. The hammer can be lifted all the way to the upper end of the steel rod.

The test procedure is simple: The hammer is dropped from an optional height, slides along the rod and hits the anvil. This mechanism creates a downward pointing force on the cone, and the cone tip will penetrate the ice surface. Every 25 mm is marked on the shaft, and 25 mm penetration is referred to as one blow set. The procedure is standardized and given in the "RSP operating instructions" (U.S. Army Corps of Engineers, 2015). The result obtained from the penetration test is a hardness number, reflecting the ice resistance against vertical penetration. The value is depending on number of drops, drop height and penetration depth, and the formula is given in Eq. 3.6.

$$\text{RSP index} = \frac{Whn}{D} + W + Q \tag{3.6}$$

where

- W = mass of drop hammer [kg]
- h = height of the hammer drops [mm]
- n = number of hammer drops
- D = penetration depth [mm]
- Q = mass of penetrometer without hammer [mm]

U.S. Army Corps of Engineers (2015) give a correlation between tire pressure and minimum required RSP index, see Fig. 3.16. The tire pressure for different aircrafts is given in the same document, and the pressure vary from 95 psi to 210 psi.

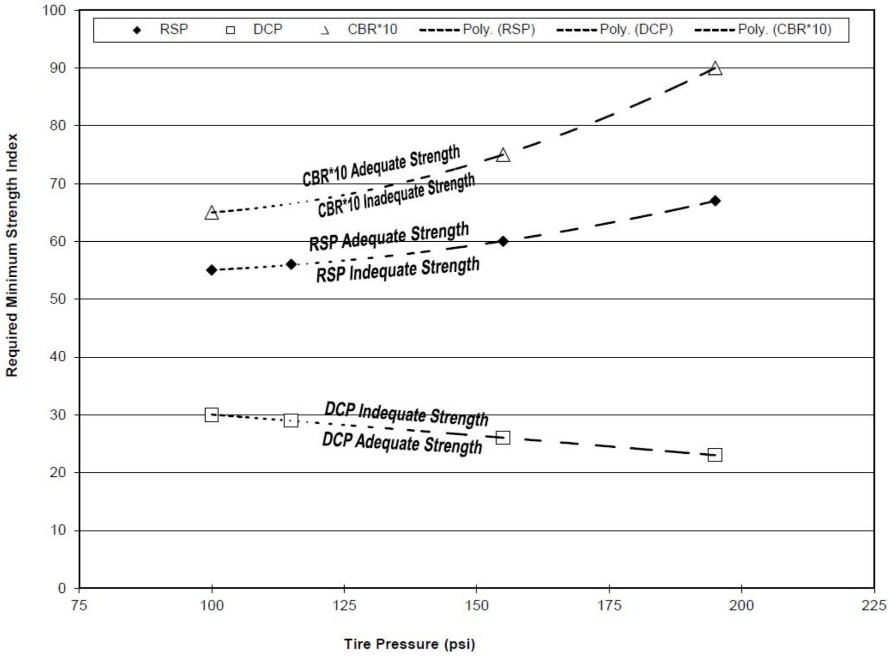

Figure 3.16: Minimum RSP index requirements for a range of tire pressure values. The relevant curve is the middle line with the black diamond marks (U.S. Army Corps of Engineers, 2015).

Chapter 4

Results

This chapter gives a presentation of the most interesting results collected during the field work at Troll Airfield and in the cold laboratories at NTNU.

In total, 65 BHJ tests and 52 RSP tests were conducted at Troll. The density were measured for 10 ice cores, whereas a selection of those were transported to Trondheim for further investigations.

In total 8 thin sections of blue ice and 2 thin sections of patch ice were made, including both vertical and horizontal sections. 3 thin sections were made of indented ice. All cores were CT scanned, but only results from the western and eastern end and one patch will treated in this thesis.

4.1 Daily climate

Notes of the weather and air temperature were taken on a daily basis. The weather varied from fully sun, lightly clouded to cloudy. On days with snow drift, no measurements were performed. The air temperature varied from -5°C to -13°C, generally decreasing during the period of the field work.

The temperature in the ice were measured within the range of -1,8°C and -14,7°C, with the majority below -7°C. The weather, air temperature and average ice temperature in the blue ice and the patch ice at 10 cm are all listed in Tab. 4.1.

Table 4.1: Weather and temperature for each day. Temperatures values are given in °C. The values represent the average measured temperature for each day. "?" means not measured and "-" means irrelevant.

Day no.	Date	Weather	Air temp.	Blue ice temp.	Patch ice temp.
1	09.02.18	sunny	-5	-7.0	-3.1
2	11.02.18	lightly clouded	-8	-9.0	-
3	14.02.18	lightly clouded	-7	?	-
4	15.02.18	sunny	-10	-8.8	-8.0
5	16.02.18	cloudy	-10	-9.6	-
6	18.02.18	sunny	-11	-12.3	-11.9
7	20.02.18	lightly clouded	-13	-14.2	-
8	22.02.18	cloudy	-11	-11.4	-10.6
9	23.02.18	cloudy	-11	-11.7	-

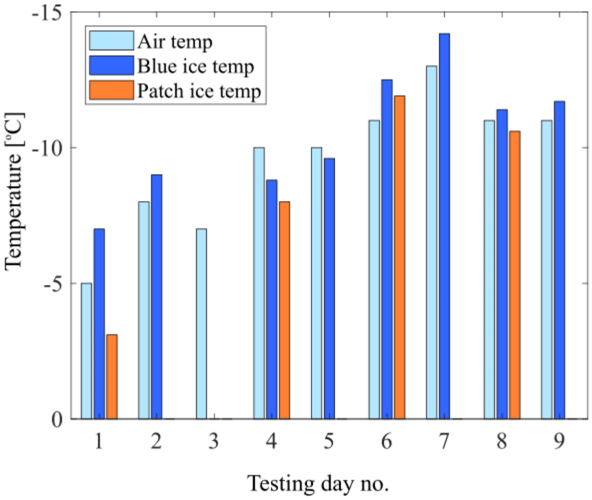

Figure 4.1: Average daily temperature measurements of the blue ice, patch ice and air.

4.2 Borehole jack results

The BHJ recordings are organized in three main groups based on type of ice and measuring depth, see Tab. 4.2. This will be the basis for comparison in the following chapters.

Table 4.2: The BHJ recordings are organized into three main groups, and a summary of the characteristics of each group are given below.

Group	Type of ice	Depth [cm]	Number of Recordings
$patch_{10}$	patch	10	11
$blue_{10}$	blue	10	45
$blue_{20}$	blue	20	9

Note that the glacier ice at the runway is assumed to be blue ice. This will be argued later in the density discussion in Chap. 5.2.

The BHJ recordings are presented as stress-time curves, and *all* graphs are given in Appx. B. The stress is calculated by the Matlab-script described in Chap. 3.2. Information about type of ice (blue ice or patch ice), measuring depth and ice temperature is given in each graph. Photos of the failure modes are provided in the appendix when available. Most stress-time curves have a distinct stress peak. The strength definition for premature failure (maximum stress) is therefore used for all results (Sinha, 2011). At the very end of each recording, there is a sudden drop in stress followed by a flatting. This marks the end of the test and is a result of stopping the drilling. Fig 4.2 shows recording bhj_2302 as an example of a typical stress-time curve. The distinct stress peak, which represents the strength, is marked with a red circle and the sudden stress drop at the end of the recording is marked with green. The testing information is listed in the box in the upper right corner.

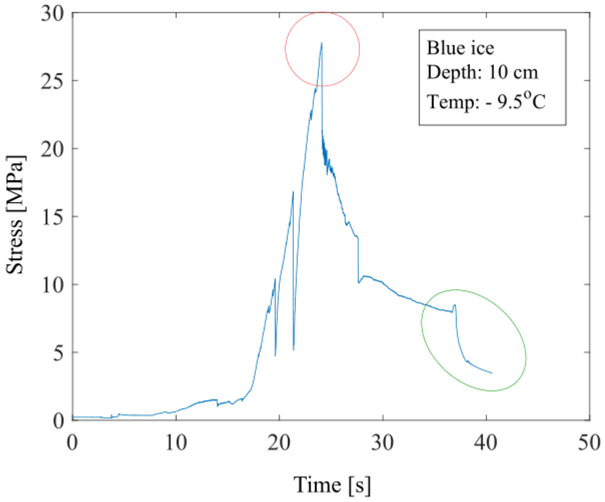

Figure 4.2: Recording bhj_2302 is given as an example of a typical stress-time curve. The red circle marks the maximum stress peak and the green circle marks the final stress drop which indicates the end of the recording.

An important factor in an indentation test is the indentation rate, describing how fast the ice is compressed. The actual penetration depth varied somewhat for each test because the borehole was slightly larger than the steel cylinder. Yet, 30 mm is regarded as a realistic estimate for a full stroke penetration, and that took approximately 34 s. Based on these numbers, the following estimate for the indentation rate (v) is provided.

$$v = \sim 0.9 \text{ mm s}^{-1} \tag{4.1}$$

In Tab. 4.3, the obtained strength values are listed for each recording, together with the depth, ice temperature and the tested ice type. The size of the longest crack is given for tests where the failure mode was visible at the surface, and the diameter of the patch is given for tests performed in patch ice.

The name of the BHJ recording provides information regarding day, location and test number. For instance, test bhj_4203 is performed at day number 4, at test area number 2 and is the third test performed at that location. The same testing area will be noted as 4.2 in the overview map in Fig. 3.1 and in the testing area maps in Appx. A. Further, this particular recording will be marked as B3 in testing area map 4.2, where the B is short for BHJ.

Table 4.3: A collection of all the BHJ results. "?" means not measured and "-" means not measurable or irrelevant for that recording.

BHJ number	Strength [MPa]	Depth [cm]	Temp [°CC]	Type of ice	Failure size [cm]	Patch size [cm]
bhj_1101	23.4	10	-7	blue	?	-
bhj_1102	19.4	10	-7	blue	?	-
bhj_1103	17.0	10	-7	blue	?	-
bhj_1104	23.9	10	-7	blue	40	-
bhj_1201	17.3	10	-3.9	patch	20	150
bhj_1202	16.7	10	-3.5	patch	35	130
bhj_1203	17.1	10	-1.8	patch*	40	130
bhj_2101	26.5	10	-9.3	blue	20	-
bhj_2102	28.3	10	-9.1	blue	25	-
bhj_2103	24.1	10	-8.6	blue	60	-
bhj_2104	29.5	10	-8.5	blue	20	-
bhj_2105	24.6	10	-9.2	blue	30	-
bhj_2106	25.2	10	-8.9	blue	50	-
bhj_2107	27.5	10	-8.5	blue	70	-
bhj_2201	20.9	10	-8.4	blue	50	-
bhj_2202	24.8	10	-8.6	blue	45	-
bhj_2203	25.4	10	-8.4	blue	60	-
bhj_2204	27.0	10	-8.2	blue	60	-
bhj_2205	14.3	10	-8.3	blue	30	-
bhj_2206	28.0	10	-8.9	blue	30	-
bhj_2207	26.7	10	-8.1	blue	40	-
bhj_2301	25.7	10	-9.7	blue	15	-
bhj_2302	27.8	10	-9.5	blue	50	-
bhj_2401	23.9	10	-10.0	blue	15	-
bhj_2402	30.2	10	-9.3	blue	50	-
bhj_2403	31.9	10	-9.4	blue	50	-

BHJ number	Strength [MPa]	Depth [cm]	Temp [°C]	Type of ice	Failure size [cm]	Patch size [cm]
bhj_2404	28.1	10	-9.6	blue	50	-
bhj_2405	25.0	10	-9.6	blue	25	-
bhj_2406	24.5	10	-9.6	blue	40	-
bhj_2407	33.1	10	-8.3	blue	70	-
bhj_2408	25.9	10	-9.0	blue	40	-
bhj_4101	18.4	10	-8.3	patch	25	80
bhj_4102	25.5	10	-8.0	patch	70	110
bhj_4103	25.8	10	-7.7	patch	85	100
bhj_4104	18.2	10	-8.0	patch	30	100
bhj_4105	20.4	10	-8.6	blue	70	-
bhj_4106	21.7	10	-9.0	blue	20	-
bhj_5101	23.2	10	-9.7	blue	25	-
bhj_5102	35.6	20	-9.6	blue	-	-
bhj_5103	24.5	10	-9.5	blue	40	-
bhj_6101	18.4	10	-11.9	patch	40	80
bhj_6102	26.9	10	-12.3	blue	50	-
bhj_6103	37.0	20	-12.4**	blue	-	-
bhj_6104	40.2	20	-12.6	blue	50	-
bhj_7101	45.0	20	-14.7	blue	-	-
bhj_7102	25.7	10	-14.5	blue	25	-
bhj_7103	23.9	10	-14.4	blue	?	-
bhj_7104	29.0	10	-14.2	blue	30	-
bhj_7201	49.1	20	-14.6	blue	40	-
bhj_7202	33.7	10	-14.3	blue	70	-
bhj_7301***	28.3	20	-13.6	blue	-	-
bhj_7302	25.6	10	-13.9	blue	70	-
bhj_7401	32.1	10	-14.0	blue	50	-
bhj_7402	21.9	10	-13.7	blue	30	-
bhj_7403	36.5	10	-14.1	blue	80	-
bhj_7404	33.7	10	-13.9	blue	80	-
bhj_8101	26.0	10	-11.5	blue	20	-
bhj_8102	26.2	10	-11.4	blue	50	-
bhj_8103	41.5	20	-11.5*	blue	70	-
bhj_8104	18.5	10	-10.7	patch	20	120
bhj_8105	26.9	10	-10.6	patch	60	120
bhj_8106	27.1	10	-10.6	patch	50	60
bhj_8107	16.8	10	-11.4	blue	70	-
bhj_9101	40.2	20	-11.8	blue	-	-
bhj_9102	37.4	20	-11.6	blue	-	-

* The patch had a darker colour compared with other patches.

** Temperature measurement is done at depth 20 cm.

*** bhj_7301 is performed in between two newly made patches.

4.2.1 Strength values

The average strength value and the standard deviation is calculated for each of the three BHJ recording groups and is given below in Eq. 4.2-4.4. The standard deviation is calculated by using the Excel function VAR.S, where the std.dev. is the square root of the variance.

$$\sigma_{patch,10} = 20.9 \pm 4.4 \text{ MPa} \tag{4.2}$$

$$\sigma_{blue,10} = 25.8 \pm 4.5 \text{ MPa} \tag{4.3}$$

$$\sigma_{blue,20} = 39.4 \pm 5.9 \text{ MPa} \tag{4.4}$$

Recording bhj_7301 is performed in between two patches located less than 1 meter apart. These patched were made only 24 hours in davance. In Tab. 4.3 one can see that the strength value of this recording is significant lower than the other tests performed at depth 20 cm. The average strength value for $blue_{20}$ is therefore also calculated without including recording bhj_7301.

$$\sigma'_{blue,20} = 40.8 \pm 4.5 \text{ MPa} \tag{4.5}$$

Spatial variation

Fig. 4.3 shows a plot of the variation of the BHJ strength along the length axis of the runway. The strength values represent the average of all recordings within each testing area. The $patch_{10}$ results are not included because the patch ice is not related to location.

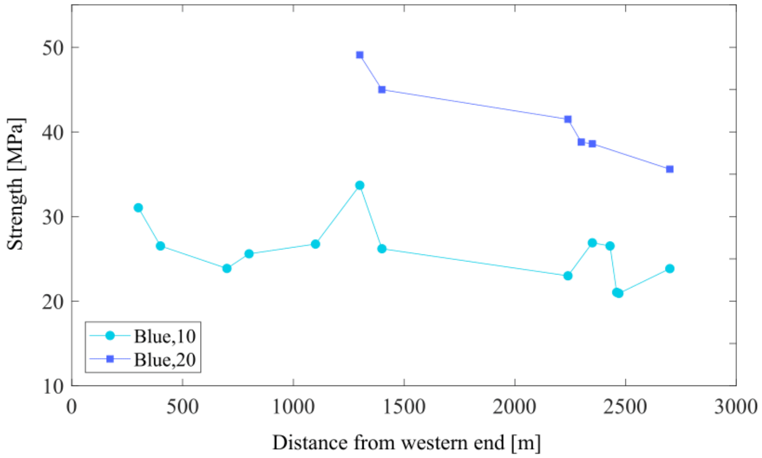

Figure 4.3: Strength values along the length axis of the runway. 0 represents the western end and 3000 represents the eastern end. The airport apron is located in between 2200 and 2450 m. The strength values are represented by the average value from all recordings within each testing location.

Temperature variation

Fig. 4.4 shows a plot of the obtained strength values for every recording vs. the respective ice temperature. The associated testing group is indicated by different colours and marking types. In Tab. 4.4 is the average strength value and std.dev. given for a temperature range of 2-3°C. The temperature intervals are marked in Fig. 4.4 by dotted lines. Note that bhj_7301 is not included in the average strength values for $blue_{20}$.

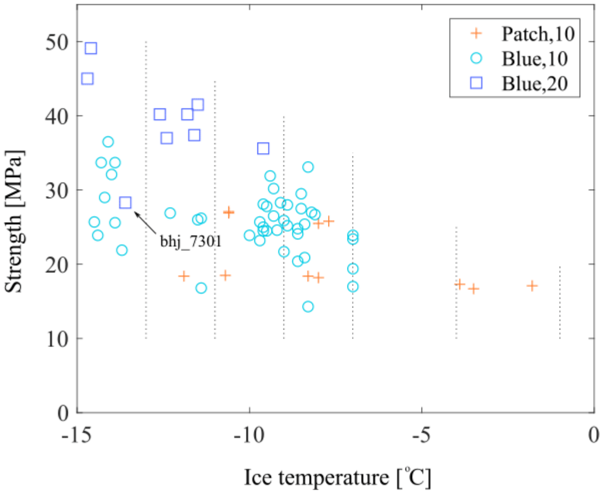

Figure 4.4: BHJ strength vs. ice temperature for the three testing groups. The vertical lines marks the temperature intervals cf. Tab. 4.4. Recording bhj_7301 is pointed out to visualize how much weaker this measurement is compared to other $blue_{20}$ recordings.

Table 4.4: Average strength values for temperature ranges of 2-3°C. The values are given for each ice type respectively. The strenght values are given in MPa.

	-1 to -4°C	-7 to -9°C	-9 to -11°C	-11 to -13°C	-13 to -15°C
$patch_{10}$	17.0 ± 0.3	22.0 ± 4.2	24.2 ± 4.9	18.4 ± 0	-
$blue_{10}$	-	24.2 ± 4.7	26.1 ± 2.7	24.0 ± 4.8	29.1 ± 5.1
$blue_{20}$	-	-	35.6 ± 0	39.3 ± 2.0	47.1 ± 2.9

4.2.2 Failure behaviour of stress-time curves

Wells classification system

A system for classifying the failure behaviour in the force-time curves is suggested by Wells et al. (2011). This system divides the failure behaviours into five categories; ductile behaviour, localized spall, isolated crushing events, cyclic-load crushing events and mixed mode, see Fig. 2.6. The slopes of the BHJ curves has been classified and ranked after the same system on a scale from 0 to 3, where 0 means that it never appeared and 3 means that it appeared frequently in the relevant curve. The localized spalls have been counted. Examples of typical failure behaviours are given in Fig. 4.5. Note that cyclic-load crushing events were not observed, and will not be treated further. Tab. 4.5 gives the ranking of the curves sorted after decreasing ice temperature. Only $patch_{10}$ and $blue_{10}$ results are included in this comparison because the confinement is higher for the $blue_{20}$ tests.

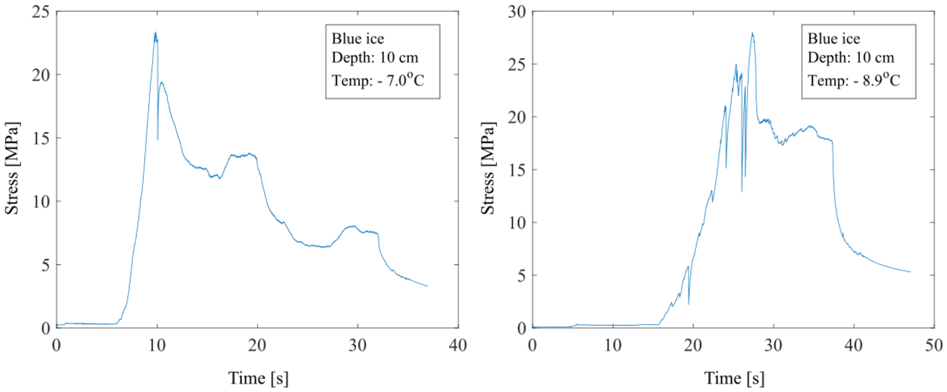

(a) bhj_1101 **(b)** bhj_2206

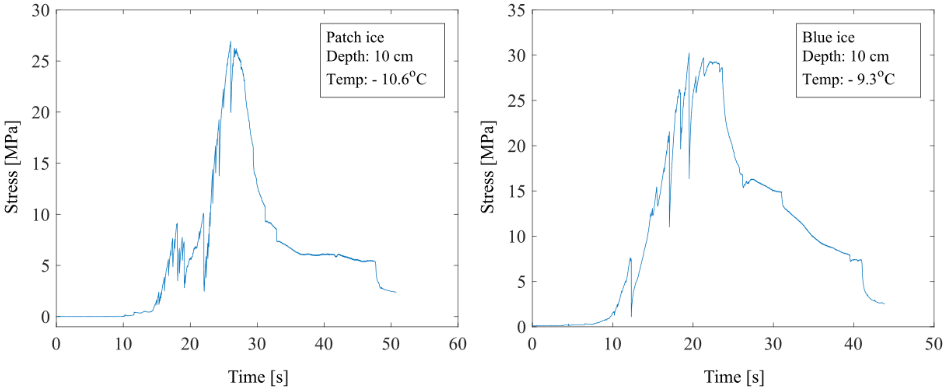

(c) bhj_8105 **(d)** bhj_2402

Figure 4.5: Examples of typical failure behaviour based on the system presented by Wells et al. (2011). (a) Ductile behaviour, (b) isolated crushing events, (c) Mixed mode (d) Localized spalls

Table 4.5: Failure behaviour ranked after system presented by Wells et al. (2011). The BHJ results are sorted after decreasing ice temperatures.

BHJ number	Ice temp.	Local spalls*	Ductile**	Isolated crushing**	Mixed mode**
bhj_1203	-1.8	0	3	0	0
bhj_1202	-3.5	0	3	0	0

BHJ number	Ice temp.	Local spalls*	Ductile**	Isolated crushing**	Mixed mode**
bhj_1201	-3.9	0	3	0	0
bhj_1101	-7.0	0	3	0	0
bhj_1102	-7.0	2	2	0	1
bhj_1103	-7.0	0	3	0	0
bhj_1104	-7.0	0	3	1	0
bhj_4103	-7.7	0	3	1	0
bhj_4102	-8.0	0	2	2	0
bhj_4104	-8.0	0	3	1	0
bhj_2207	-8.1	1	2	1	2
bhj_2204	-8.2	3	2	0	1
bhj_2205	-8.3	0	3	1	1
bhj_2407	-8.3	2	1	0	1
bhj_4101	-8.3	0	3	0	0
bhj_2201	-8.4	0	3	1	1
bhj_2203	-8.4	3	1	0	1
bhj_2104	-8.5	2	1	1	1
bhj_2107	-8.5	4	0	0	1
bhj_2103	-8.6	1	2	0	1
bhj_2202	-8.6	0	2	1	1
bhj_4105	-8.6	1	2	1	0
bhj_2106	-8.9	2	2	0	1
bhj_2206	-8.9	3	2	2	1
bhj_2408	-9.0	2	2	1	0
bhj_4106	-9.0	1	1	0	2
bhj_2102	-9.1	0	3	1	1
bhj_2105	-9.2	3	0	1	3
bhj_2101	-9.3	0	2	1	1
bhj_2402	-9.3	4	1	1	0
bhj_2403	-9.4	3	0	0	1
bhj_2302	-9.5	2	2	1	0
bhj_5103	-9.5	1	0	0	3
bhj_2404	-9.6	1	2	1	1
bhj_2405	-9.6	4	0	0	1
bhj_2406	-9.6	2	1	1	1
bhj_2301	-9.7	4	0	0	2
bhj_5101	-9.7	3	2	0	1
bhj_2401	-10.0	5	0	0	3
bhj_8105	-10.6	4	0	0	3
bhj_8106	-10.6	1	1	1	2
bhj_8104	-10.7	1	2	2	2
bhj_8102	-11.4	3	1	1	3
bhj_8107	-11.4	1	0	0	2
bhj_8101	-11.5	1	0	0	2
bhj_6101	-11.9	3	2	1	3

BHJ number	Ice temp.	Local spalls*	Ductile**	Isolated crushing**	Mixed mode**
bhj_6102	-12.3	3	1	1	2
bhj_7402	-13.7	1	0	0	2
bhj_7302	-13.9	2	0	0	3
bhj_7404	-13.9	2	0	1	3
bhj_7401	-14.0	7	0	0	3
bhj_7403	-14.1	2	1	0	2
bhj_7104	-14.2	5	0	0	3
bhj_7202	-14.3	5	0	0	3
bhj_7103	-14.4	3	0	0	3
bhj_7102	-14.5	4	0	0	3

* Counted numbers of large stress drops.

** 0 = never, 1 = infrequent, 2 = moderate, 3 = frequent

Sawtooth loading

Another discussed failure behaviour is the sawtooth loading mechanism, described by O'Rourke et al. (2016). Fig. 4.6 shows examples of curves that might represent such behaviour. Note that these BHJ recordings are among the $blue_{20}$ tests.

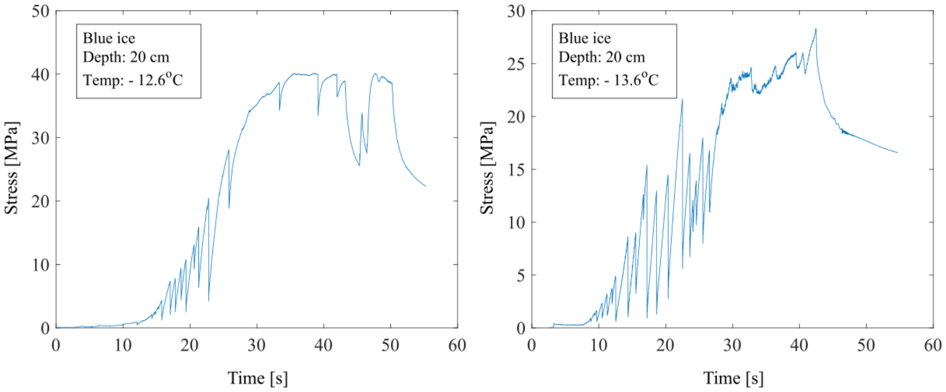

(a) bhj_6104

(b) bhj_7301

Figure 4.6: Examples of stress-time curves with sawtooth loading.

Terminal stress behaviour

The results can also be separated into two groups based the difference in terminal behaviour. Some of the curves has a sudden drop in stress, which leaves the maximum recorded stress as a distinct peak. For other curves, the stress is continually increasing before it seems to stabilize at a plateau. Most of the $blue_{10}$ and $patch_{10}$ results belong in the first group with a distinct stress peak, and examples of such behaviour is already given in Fig. 4.5. Most of the $blue_{20}$ results, on the other hand, are placed in the second group where the stress stabilizes at a plateau. Fig. 4.7 shows examples of two such $blue_{20}$ recordings. It must be reminded that the stress drop at the very end of these recordings is caused by stopping the drilling and not failure in the ice.

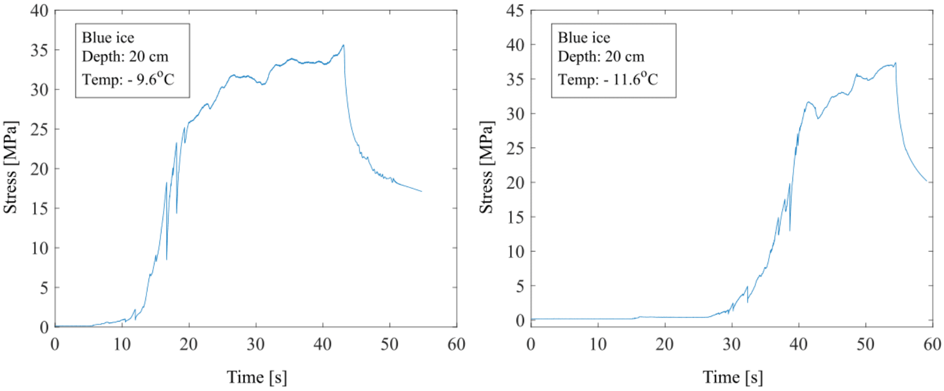

(a) bhj_5102 **(b)** bhj_9102

Figure 4.7: Examples of stress-time curves where the stress stabilized at a plateau, both from the $blue_{20}$ group.

4.2.3 Failure mode observations

Information regarding the failure mode is revealed during the conduction of the BHJ test. Cracks could be observed at the surface for most tests, and often larger ice blocks were released and lifted in the area above the piston. These blocks are called spalls. The size of the spall is measured as the distance from the borehole to the circumference. Whenever this distance varied along the spall edge, an estimate of the mean length was reported. The measurements are given Tab. 4.3. Most of the failure modes are also photographed, and pictures are shown next to the stress-time curves in Appx. B.

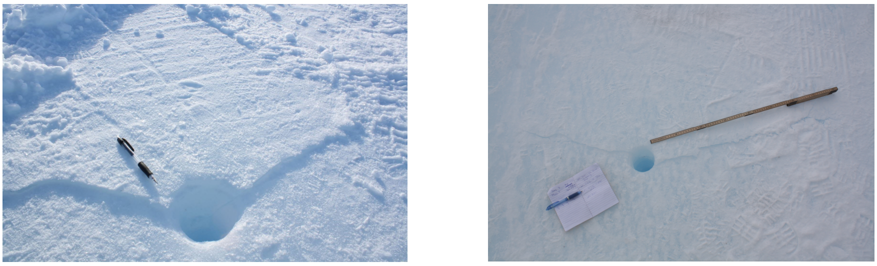

(a) bhj_2408 **(b)** bhj_2103

Figure 4.8: Pictures of failure modes where there were cracks at the surface, but no ice blocks were lifted.

(a) bhj_2106 **(b)** bhj_2102

Figure 4.9: Pictures of spalls produced during $blue_{10}$ tests. (a) shows a relative large spall of 50 cm and (b) shows a smaller spall of 25 cm. The yardstick and the notebook is included in the pictures for scale.

Fig. 4.9 shows spalls produced during $blue_{10}$ tests. The spall in Fig. 4.9a is an example of a larger spall with crack length of 50 cm, and Fig. 4.9b shows a smaller spall of 25 cm.

Fig. 4.8 shows examples of failure modes where there are cracks at the surface, but the ice block is not lifted. However, during the field work period it was experienced that spalls often could be released if one used a crowbar or a spade, but this required some power.

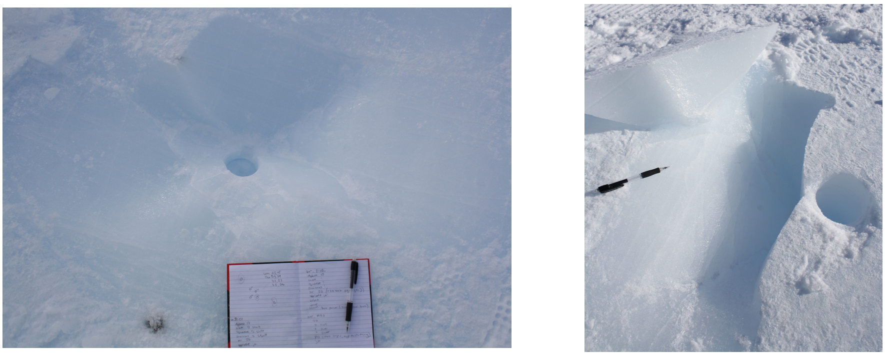

(a) bhj_8103 **(b)** bhj_6105

Figure 4.10: Pictures of failure modes for tests performed at 20 cm depth. (a) shows an example of a large spall, and (b) shows a spall with symmetrical shape.

For most of the $blue_{20}$ tests, there were no visual cracks at the surface and no spalls were produced. For the instances during which spalling occurred, the spalls were often very massive. Fig. 4.10a shows an example of such large spalls. It must be noted that the BHJ cylinder was slightly inclined during the conduction of this particular test, which might have influenced the size of the failure mode. Fig. 4.10b shows an example of another spall produced in a $blue_{20}$ test. This failure stands out in its symmetrical shape.

Fig. 4.11 shows a plot of the BHJ strength vs. the spall size. For the tests where no cracks could be observed at the surface, the size is reported as 0 cm in the plot.

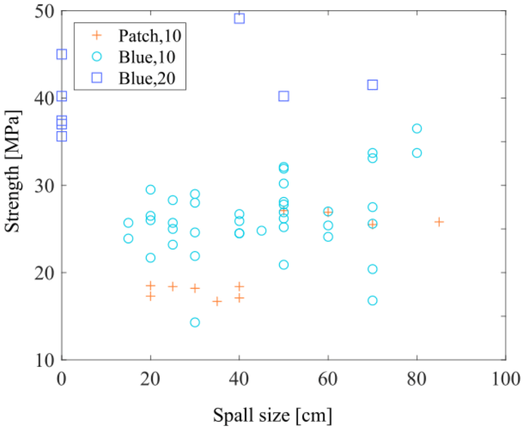

Figure 4.11: BHJ strength vs. spall size. Whenever no cracks were observed at the surface, the spall size is reported as 0.

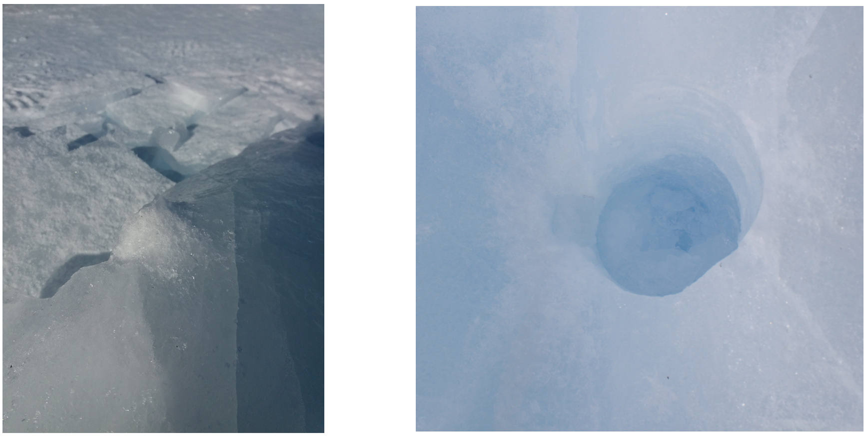

(a) bhj_4103

(b) bhj_8103

Figure 4.12: Pictures of the indented ice. A white powder-like material could be observed in the ice adjacent to the piston. (a) Underside of a the spall produced for bhj_4103. (b) Borehole and the indented ice seen from above.

The indented ice was visual inspected for a few of the BHJ tests. Generally, a horizontal crack evolved across the indentation mark, splitting the indented ice in two and producing a spall. The inspection was done beneath the spall and of the indentation mark in the borehole wall. Often, white powder-like material could be observed just behind the indentor as one can see in Fig. 4.12a. Fig. 4.12b shows a picture of a borehole seen from above. One can see a difference in the blue ice and the white crushed ice close to the piston mark. As mentioned earlier, test recording bhj_8103 was conducted with a slightly tilted BHJ cylinder. This resulted in crushing of the ice along the opposite side of the borehole, which also can be seen in the picture.

Another failure mode observation was the audible sounds coincident with the spalling. Different sounds could be heard, varying from long-lasting squeeze-sounds to periodic crushing-sounds. Sometimes distinct crack-sounds could be heard, and they could be quite loud. This holds especially for tests performed at deeper depths of 20 cm. Whenever these crack-sounds where counted, the number of cracks often corresponded with number of larger stress drops in the curve. For instance, during the conduction of bhj_7301 seen in Fig. 4.6b, about 15 loud cracking-sounds were counted. Another examples of this phenomena is bhj_5101, shown in Fig.4.13, where three distinct cracking-sounds were registered. The counting of the cracking-sounds were only done sporadic.

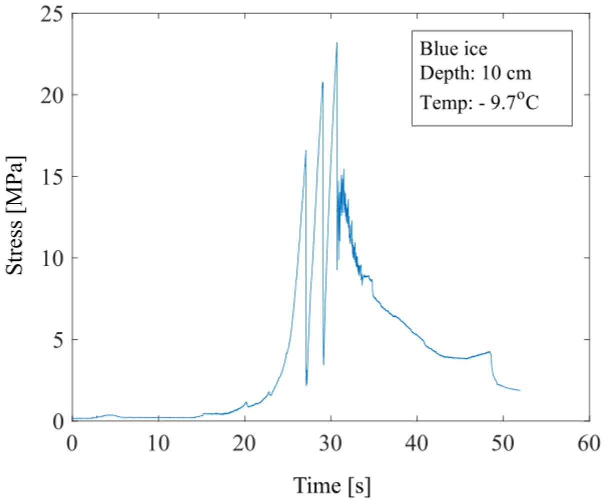

Figure 4.13: Stress-time curve for bhj_5101. Three distinct cracking-sounds were heard during the conduction of this test, which corresponds to the number of larger stress drops.

4.3 Density

In total 10 ice cores were collected with the purpose of measuring the density. Some of these cores were also brought back to NTNU for further investigations. The cores were collected in blue ice from the eastern and the western end, the middle of the runway and from a patch at the airport apron. The areas are marked D1-D4 in the overview map in Fig. 3.1, and the sampling areas are also the basis for the naming of each core. For instance, d_203 is the third core collected at D2, which is in the middle of the runway. The results are shown in Fig. 4.14a-d. As it appears from the graphs, the cores were not in one piece when extracted from the core sampler, and the density was measured for each piece, respectively.

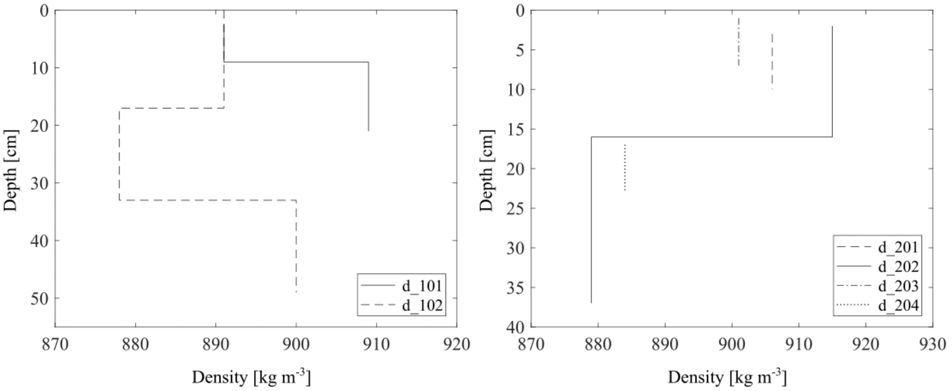

(a) D1 - east **(b)** D2 - middle

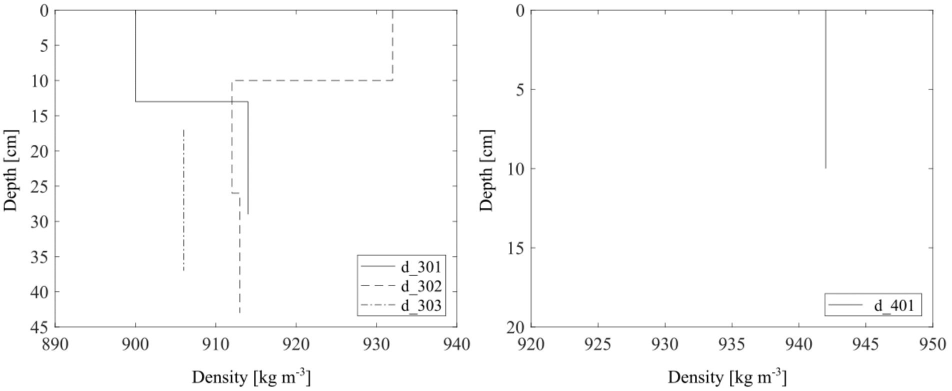

(c) D3 - west **(d)** D4 - patch

Figure 4.14: Density measurements for 10 ice cores collected at the runway.

4.4 Thin sections

In this project, there were made thin sections of the blue ice at different depths, the patch ice and the indented ice from BHJ recordings. Pictures of the thin sections under cross polarized light are given in Tab. 4.6, 4.7 and 4.8, respectively. The thin section of the indented ice will be referred to as "BHJ-sections" in the following. General information about location, direction of the cut (horizontal/vertical), thickness of the thin section and the measured grain size are given next to the pictures. Corresponding density measurements are also given. For the BHJ-sections, measured thickness of the damaged layer and diameter of the grains in this area are included.

The grain size of the blue ice was measured directly from the pictures in Tab. 4.6, and was found in the range of 2-8 mm. However, the grain size of 4-5 mm were highest represented, in where the average grain size was found. The grains had a tendency to be elongated in the vertical direction. Some of the blue ice thin sections show a tendency of similarity in grain colours, while others are randomly coloured.

The grain size of the patch ice was measured in the range of 1-7 mm, where all sizes were equally represented. No elongation in any direction were observed. The grains were randomly coloured.

In the area just behind the indentor in the BHJ-sections, the grain size is significantly reduced to less than 1 mm.

The numbering of the thin sections provide information about the location (D1-D4) and depth of the ice core. For instance, ts_120v is made of an ice core from D1 (eastern part of runway) and from depth 20 cm. The numbering of the BHJ-sections represents the corresponding BHJ test. All BHJ-sections are collected at depth 20 cm. The "h" or "v" in the end of the numbers tell if it is a horizontal or vertical section

Table 4.6: Pictures of thin sections made of blue ice together with general information about the location and dimensions. The cores are collected from the eastern and the western end and midway at the runway. A ruler is included in the pictures to give the scale.

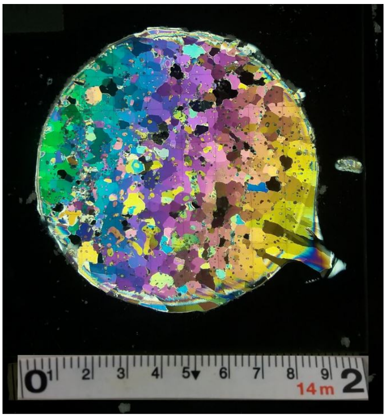

- **Name: ts_110h**
- Location: east
- Depth: 10 cm
- Density: d_102
- Cut: horizontal
- Thickness: 0.6 mm
- Grain size: 2-8 mm

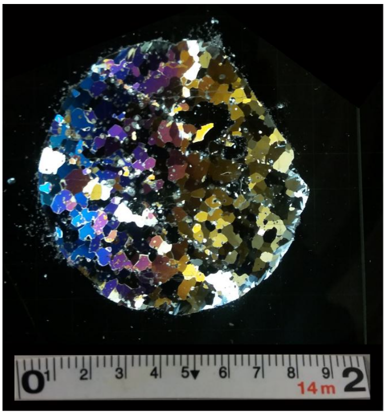

- **Name: ts_120h**
- Location: east
- Depth: 20 cm
- Density: d_102
- Cut: horizontal
- Thickness: 0.5 mm
- Grain size: 3-5 mm

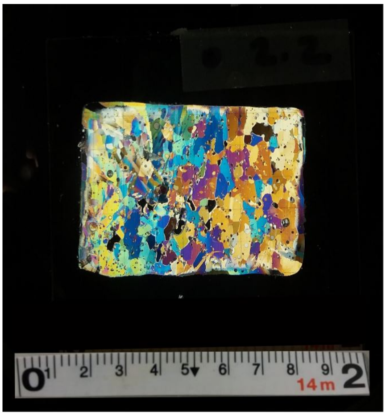

- **Name: ts_120v**
- Location: east
- Depth: 20 cm
- Density: d_102
- Cut: vertical
- Thickness: 0.4 mm
- Grain size: 3-8 mm

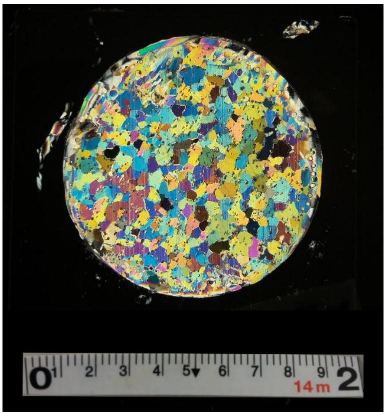

- **Name: ts_210h**
- Location: middle
- Depth: 10 cm
- Density: d_201
- Cut: horizontal
- Thickness: 0.8 mm
- Grain size: 3-4 mm

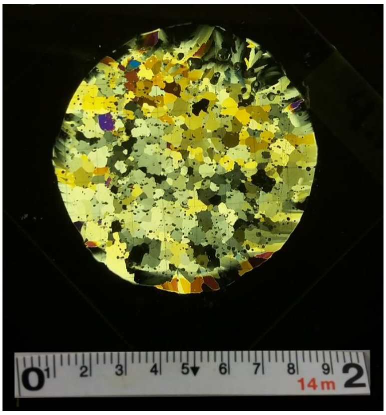

- **Name: ts_310h**
- Location: west
- Depth: 10 cm
- Density: d_301
- Cut: horizontal
- Thickness: 0.4 mm
- Grain size: 2-5 mm

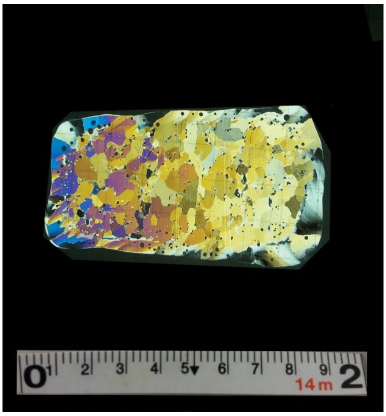

- **Name: ts_310v**
- Location: west
- Depth: 10 cm
- Density: d_301
- Cut: vertical
- Thickness: 0.4 mm
- Grain size: 3-8 mm

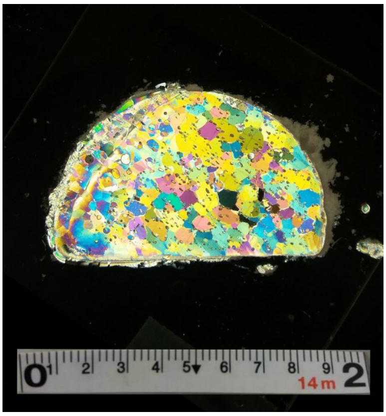

- **Name: ts_320h**
- Location: west
- Depth: 20 cm
- Density: d_302
- Cut: horizontal
- Thickness: 0.8 mm
- Grain size: 3-5 mm

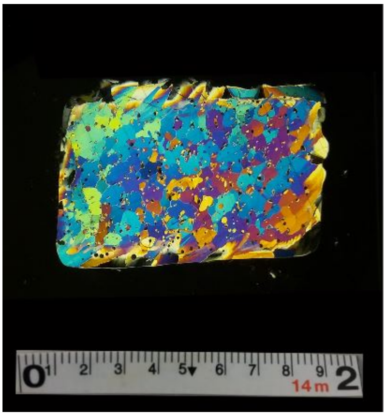

- **Name: ts_320v**
- Location: west
- Depth: 20 cm
- Density: d_302
- Cut: vertical
- Thickness: 0.5 mm
- Grain size: 3-8 mm

Table 4.7: Pictures of thin sections made of patch ice together with general information about the location and dimensions. The core is collected from a patch at the airport apron. A ruler is included in the pictures to give the scale.

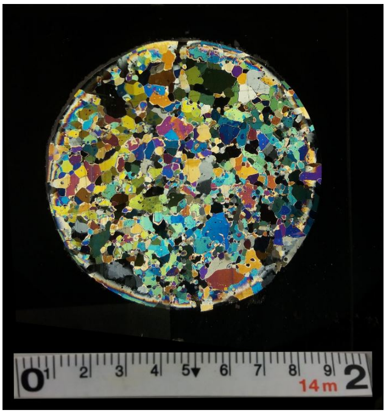	**Name: ts_410h** Patch ice Depth: 5 cm Density: d_401 Cut: horizontal Thickness: 0.4 mm Grain size: 1-7 mm
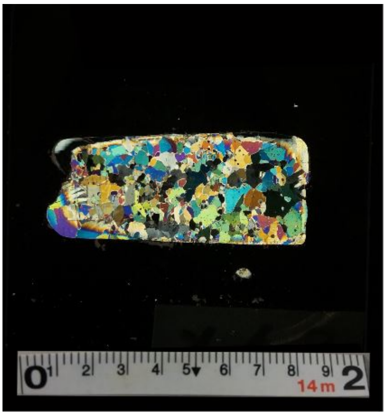	**Name: ts_410v** Patch ice Depth: 5 cm Density: d_401 Cut: vertical Thickness: 0.5 mm Grain size: 1-7 mm

Table 4.8: Pictures of thin sections made of the indented ice from three BHJ experiments, referred to as BHJ-sections. The corresponding BHJ recording is given in the list to the right of the picture, together with information about the dimensions of the thin section, the intact blue ice and the damaged layer.

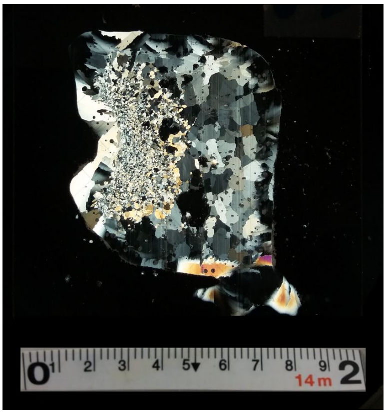

- **Name: ts_7101v**
- bhj_7101
- Depth: 20 cm
- Cut: vertical
- Thickness: 0.2 mm
- Grain size: 3-7 mm
- Crushed ice diameter: 0.3-2 mm
- Layer thickness: 2 cm

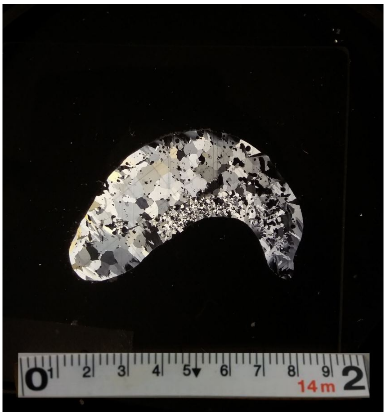

- **Name: ts_8103h**
- bhj_8103
- Depth: 20 cm
- Cut: horizontal
- Thickness: 0.2 mm
- Grain size: 3-7 mm
- Crushed ice diameter: 0.3-1 mm
- Layer thickness: 0.4 cm

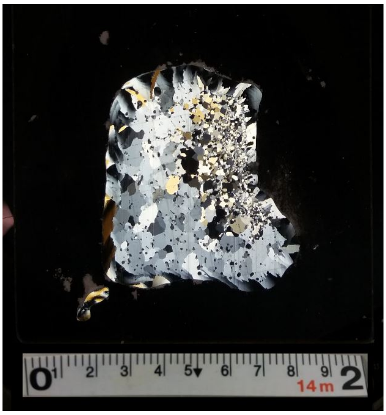

- **Name: ts_9101v**
- bhj_9101
- Depth: 20 cm
- Cut: vertical
- Thickness: 0.3 mm
- Grain size: 3-6 mm
- Crushed ice diameter: 0.5-2 mm
- Layer thickness: 1.5 cm

4.5 CT-scanning

In this section will a selection of the CT scan results be presented. All ice cores that were transported to Trondheim were CT scanned, but the results from only three samples will be treated in this thesis: Two blue ice cores from the eastern and western and, and one core from a patch. The is regarded as sufficiently to give an impression of the blue ice in general, and for a comparison between the blue ice and the patch ice. The indented ice cores were also scanned, and these results will be compared to the thin sections of the same ice.

Fig. 4.15, 4.16 and 4.17 show horizontal cross-sectional pictures and a 3D figure. The figures show results from the blue ice from eastern and western end and of the patch ice from the airport apron, respectively. The first picture (a) is an untreated picture from the X-ray scanning. The second picture (b) is basis for a solid volume fraction (SVF) calculation. The square is taken from the inside of the core circle, as indicated by the red line in Fig 4.15a. The same square is used in all the horizontal pictures through the length of the core, and when these squares are stacked on top of each other, a 3D figure is obtained. The 3D figure has shape of a cube as shown in (c). The red colour in (b) represents ice mass and the white colour represents air, and SVF is calculated from the amount of red colour. In Fig. 4.17 there are some green colour too, and this is sand particles in the patch ice. The (b) picture is made based on the degree of absorption for each mineral.

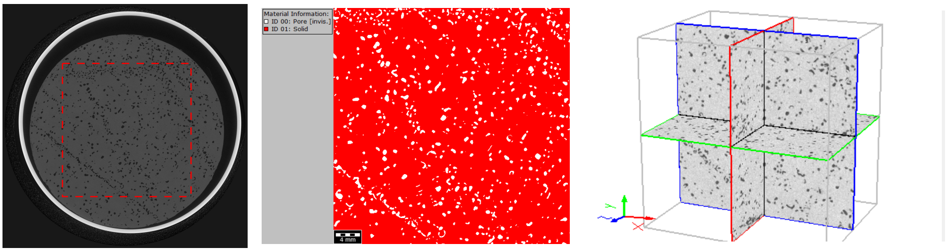

(a) **(b)** **(c)**

Figure 4.15: CT scan of the ice core from the eastern end at depth 10 cm. (a) Untreated X-ray picture, horizontal cross section. (b) Square taken from inside of the core circle in (a), used for SVF calculations. (c) 3D figure of the ice core. The z-axis represents the length axis of the ice core. The red square in (a) indicates where (b) is taken from.

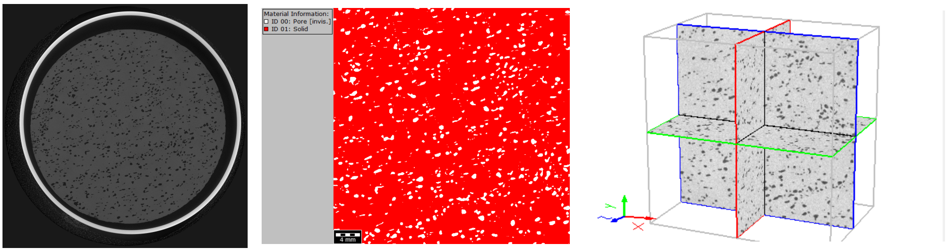

(a) **(b)** **(c)**

Figure 4.16: CT scan of the ice core from the western end at depth 10 cm. (a)-(c) cf. Fig. 4.15.

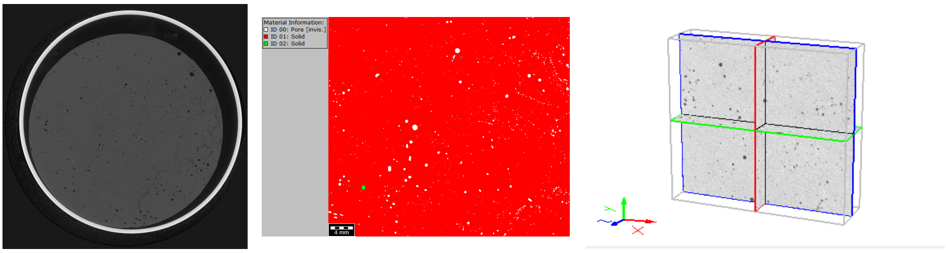

(a) **(b)** **(c)**

Figure 4.17: CT scan of the ice core from the patch ice collected at the airport apron. (a)-(c) cf. Fig. 4.15.

A calculation of the solid volume fraction (SVF) along the length axis of the ice core is performed, see Fig. 4.18. This is basically the amount of red colour in each picture along the z-axis It must be noted that it is unclear which direction of the z-axis is pointing upwards. The mean SVF for each ice core is given in Eq. 4.6-4.8.

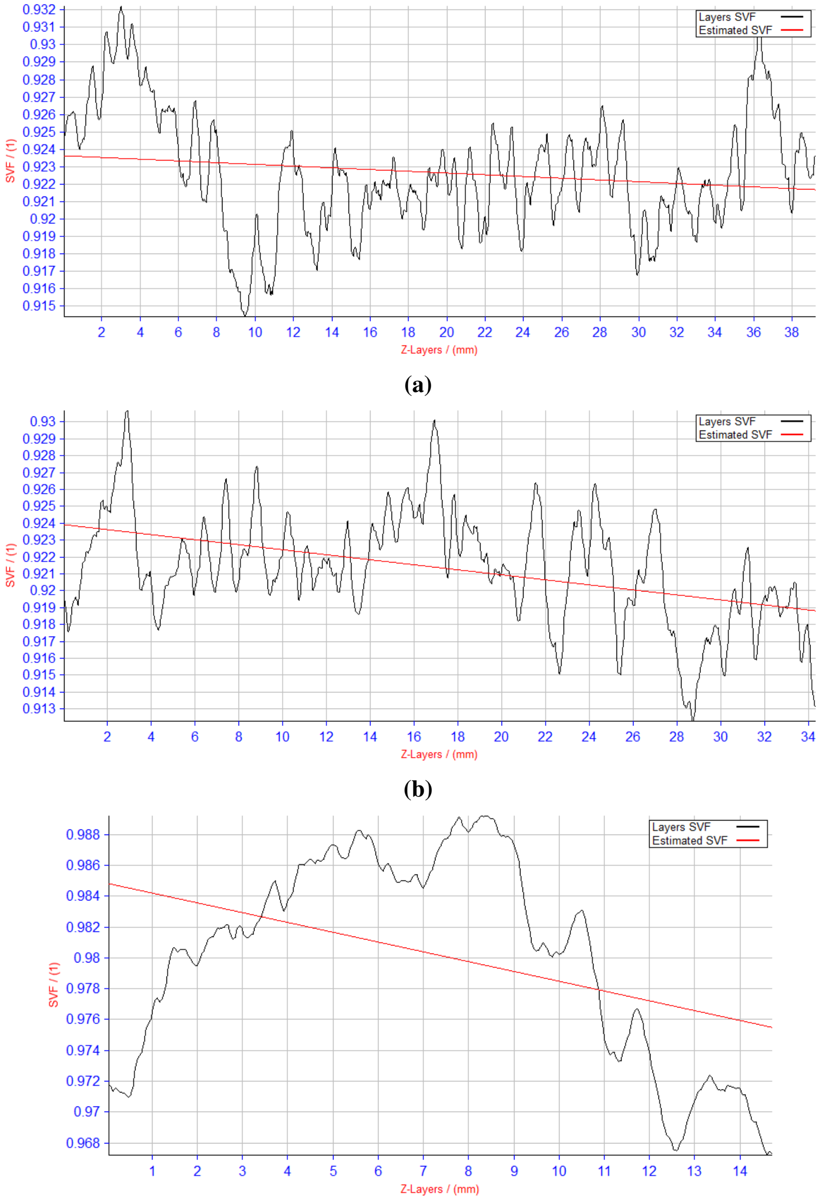

(a)

(b)

(c)

Figure 4.18: SVF along the length axis for the three ice cores, (a) eastern end, (b) western end, (c) patch ice.

$$SVF_{east,10} = 0.92265 \tag{4.6}$$

$$SVF_{west,10} = 0.921342 \tag{4.7}$$

$$SVF_{patch} = 0.980105 \tag{4.8}$$

The SVF results are used to calculate the density of the ice cores, simply by multiplying with the maximum density of ice. The maximum density of the ice at 0°C is 916.4 kg m^{-3} and is used in these calculations. Eq. 4.9-4.11 gives the densities of the ice core based on the CT scan.

$$\rho_{east,10} = 846 \text{ kg m}^{-3} \tag{4.9}$$

$$\rho_{west,10} = 844 \text{ kg m}^{-3} \tag{4.10}$$

$$\rho_{patch} = 898 \text{ kg m}^{-3} \tag{4.11}$$

Fig. 4.19 shows the pore size distribution for the three ice cores. The peak in the graphs represent the most frequent pore diameter.

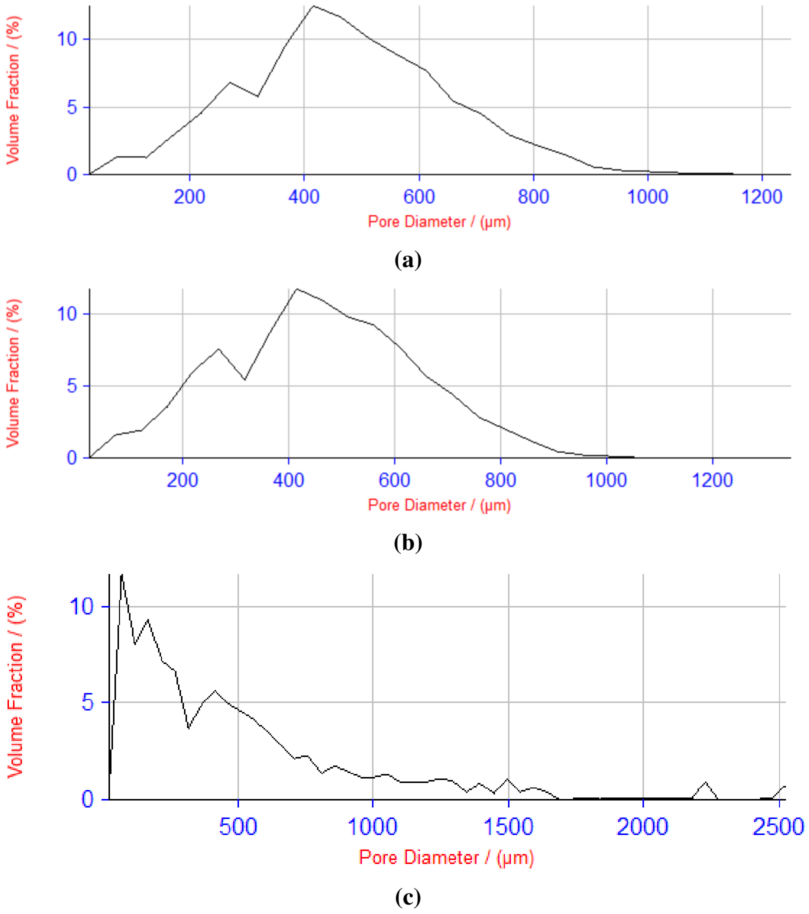

Figure 4.19: Volume fraction for different pore diameters for the three ice cores, (a) eastern end, (b) western end, (c) patch ice.

The photographs below show untreated X-ray pictures of ice cores with indented ice, taken before the thin sections were made. Fig. 4.20 correspond to ts_7101, Fig. 4.21 to ts_8103 and Fig 4.22 to ts_9101. Note that all the photos below show horizontal cuts of the ice core. Since ts_7101 and ts_9101 are vertical sections, a red dotted line is included in Fig. 4.20 and 4.22 to indicate where the vertical thin sections were taken.

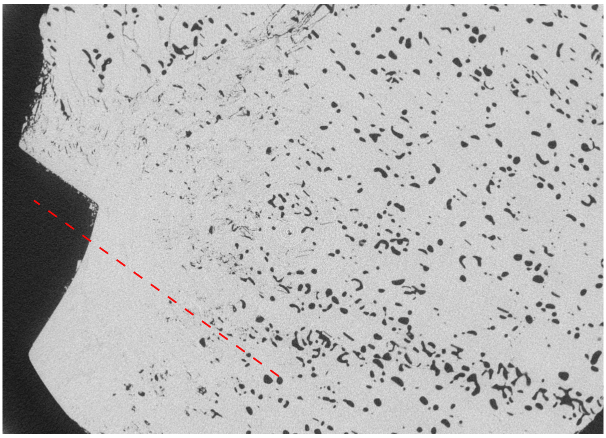

Figure 4.20: Untreated X-ray picture of the indented ice from the bhj_7101 test. This picture shows a horizontal cut of the ice core. The red line indicates where the corresponding, vertical thin section ts_7101 is taken.

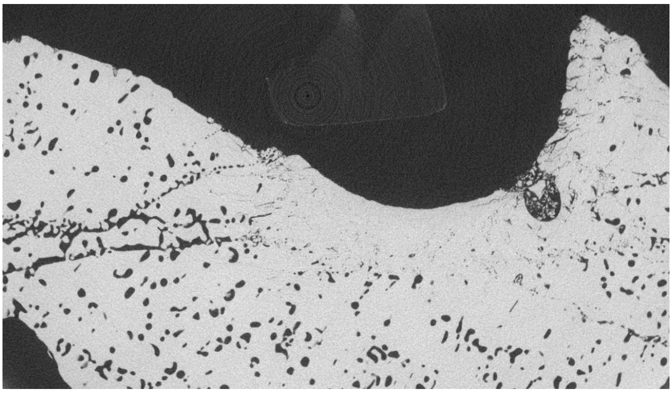

Figure 4.21: Untreated X-ray picture of the indented ice from the bhj_8103 test. This picture shows a horizontal cut of the ice core and corresponds to thin section ts_8103.

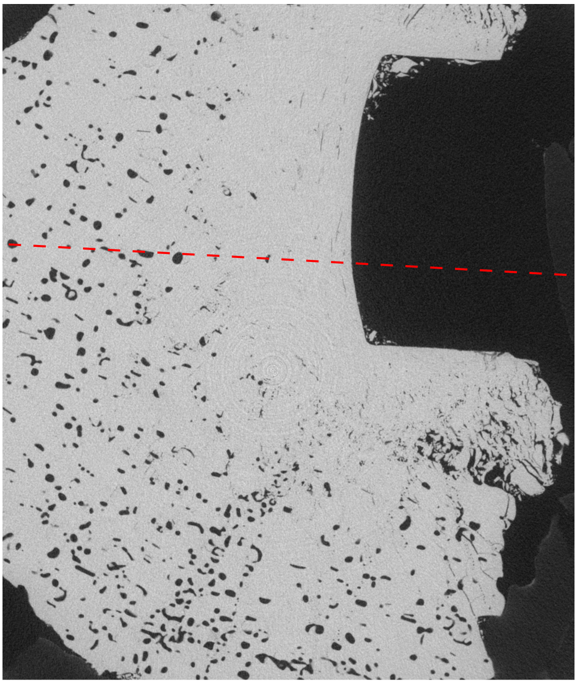

Figure 4.22: Untreated X-ray picture of the indented ice from the bhj_9101 test. This picture shows a horizontal cut of the ice core. The red line indicates where the corresponding, vertical thin section ts_9101 is taken.

4.6 Russian snow penetrometer

The RSP index is calculated after Eq. 3.6, and the index value for the upper 7.5 cm of the surface is given in Tab. 4.9. For tests conducted at day 2, 3, 4 and 5, the number of drops for every 25 mm penetration was noted and given in the table. In the following days, only the sum of drops at 75 mm penetration was noted. Corresponding ice temperature measurements at the surface does not exist for the RSP test. The given temperatures in the table are therefore the average value of the ice temperature measured for the BHJ tests in the same area. No such measurements exist for day 2 because the RSP measurements were conducted the day after the BHJ tests. No ice temperature measurements were done for day 3 because there are no corresponding BHJ tests.

The RSP results are named after the same system as the BHJ results, where the first to digits gives the day and testing site and the two last digits give the testing number at relevant site.

Table 4.9: A collection of all the RSP results. "?" means not measured and "-" means not measurable or irrelevant for that recording.

Name	1.	2.	3.	Sum of drops	RSP index	Temp [°C]
rsp_2101	3	7	13	23	273	?

Name	1.	2.	3.	Sum of drops	RSP index	Temp [°C]
rsp_2102	3	5	13	21	249	?
rsp_2201	3	7	5	15	179	?
rsp_2202	2	2	5	9	109	?
rsp_2203	3	11	13	27	320	?
rsp_2301	4	5	11	20	238	?
rsp_2302	3	7	10	20	238	?
rsp_2401	5	7	7	19	226	?
rsp_2402	3	8	20	31	367	?
rsp_2403	4	8	14	26	308	?
rsp_2404	3	10	12	25	296	?
rsp_3101	2	4	6	12	144	?
rsp_3102	3	8	8	19	226	?
rsp_3103	3	7	11	21	249	?
rsp_3104	3	6	18	27	319	?
rsp_3105	2	11	11	24	285	?
rsp_3106	3	4	7	14	167	?
rsp_3107	2	8	14	24	285	?
rsp_3108	2	7	15	24	285	?
rsp_4101	2	11	17	30	355	-10.5
rsp_4102	3	5	15	23	273	-10.5
rsp_4103	4	14	16	34	402	-10.5
rsp_4104	4	5	10	19	226	-10.5
rsp_4105	3	10	12	25	296	-10.5
rsp_5101	4	7	17	28	332	-10.5
rsp_5102	4	10	17	31	367	-10.5
rsp_7101	-	-	-	27	320	-14.4
rsp_7102	-	-	-	32	378	-14.4
rsp_7103	-	-	-	28	332	-14.4
rsp_7201	-	-	-	33	390	-14.3
rsp_7202	-	-	-	16	191	-14.3
rsp_7203	-	-	-	20	238	-14.3
rsp_7204	-	-	-	13	156	-14.3
rsp_7205	-	-	-	35	414	-14.3
rsp_7206	-	-	-	10	121*	-14.3
rsp_7301	-	-	-	26	308	-13.9
rsp_7302	-	-	-	21	249	-13.9
rsp_7303	-	-	-	25	296	-13.9
rsp_7304	-	-	-	18	214	-13.9
rsp_7401	-	-	-	20	238	-13.9
rsp_7402	-	-	-	20	238	-13.9
rsp_7403	-	-	-	21	249	-13.9
rsp_7404	-	-	-	21	249	-13.9
rsp_8101	-	-	-	34	402	-11.4
rsp_8102	-	-	-	19	226	-11.4

Name	1.	2.	3.	Sum of drops	RSP index	Temp [°C]
rsp_8103	-	-	-	23	273	-11.4
rsp_8104	-	-	-	23	273	-11.4
rsp_8105	-	-	-	27	320	-11.4
rsp_8106	-	-	-	26	308	-11.4
rsp_9101	-	-	-	23	273	-11.7
rsp_9102	-	-	-	30	355	-11.7
rsp_9103	-	-	-	33	390	-11.7

*Performed in a patch made about 24 hours in advance.

The average RSP index between 5 and 10 cm is

$$\text{RSP index (average)} = 274 \text{ kg} \tag{4.12}$$

Fig. 4.23 shows the average RSP index with depth for the different testing areas. Only the first measurements are included because this is the only times that number of drops were counted for every 2.5 cm.

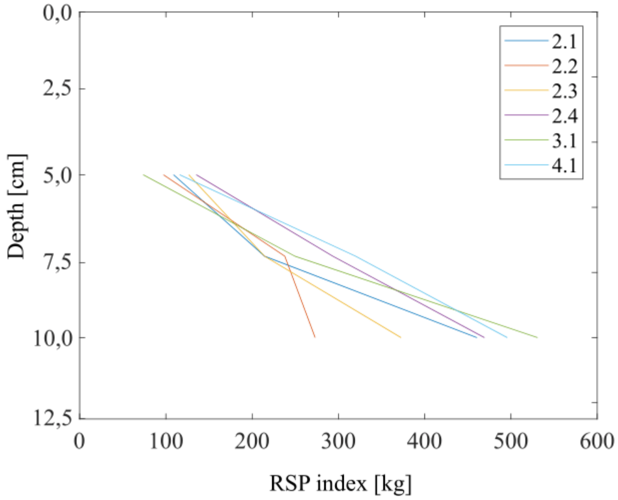

Figure 4.23: RSP index with depth.

Chapter 5

Discussion

The first part of this chapter is dedicated to the BHJ results. The strength values and variations in the measurements will be elaborated. A study of the failure behaviour has also been conducted, in that a comparison with the literature review presented in Chap. 2.3 is essential. Last in this section is a discussion of the bubble density and the possible effect on the flexural strength.

This section is followed by a comparison of the density measurements from the mass/volume method and from the values obtained from the CT scan analysis. Next in line is a discussion of the thin section results. The main focus will be on BHJ-sections. In that is a comparison with the X-ray pictures from the CT scan. As it appears, the CT scan will not be treated separately, but used as a support to the other results.

Lastly, there will be a discussion of the RSP results and the relevance of this test.

5.1 Borehole jack

The main goal for the BHJ experiments were to investigate the runway strength. This included blue ice measurements at depth 10 cm and 20 cm, and patch ice measurements at depth 10 cm.

In the first period of the field work, only shallower measurements were conducted due to a general concern regarding the functionality of the newly developed jack. The ice strength was expected to increase with depth and one did not want to break the jack before at least some data had been collected. No deeper measurements than 20 cm were conducted due to challenges in the borehole preparations.

All the patch ice measurements were conducted at the airport apron to avoid disturbance of the airport traffic. The blue ice measurements, on the other hand, could be conducted along the edge of the airstrip without effecting the airfield activity.

5.1.1 Strength values

If one compare the average strength values for the different testing groups given in Eq. 4.2-4.5, it is evident that the patch ice is in general weaker than the the blue ice, and that the strength increases with depth. However, the magnitude of the strength values must be considered with caution. The calculation of the stress is based on a theoretical derived relationship between the measured force and the indentation load. This indentation load factor, c, is dependant on rough estimates for the friction coefficients μ_1, μ_2 and μ_3. Furthermore, c proves to be very sensitive toward these friction coefficients. Having said that, the reported strength values are within the same range as the collected BHJ results in Fig. 2.5 (Johnston et al., 2003). Hence, the suggested value of c in Eq. 3.3 is assumed to provide a reasonable indentation load estimate.

There are two strength values given for the $blue_{20}$ ice, one where bhj_7301 is included ($\sigma_{blue,20}$) and one without this recording ($\sigma'_{blue,20}$). The bhj_7301 test was performed in between two newly made patches spaced less than one meter apart from each other. The strength recorded from this test was significant lower than the other $blue_{20}$ recordings, see Fig. 4.4. From this observation one can argue that the stress distribution from a BHJ indentation is larger than half a meter away from the borehole. Since the fresh patches seem to have effected the strength of the bhj_7301 recording, the average strength without this value is considered as representative for the $blue_{20}$ recordings.

The standard deviation gives an indication of the scatter in the obtained strength values for the different testing groups. The std.dev. given in Eq. 4.2, 4.3 and 4.5 are of the same magnitude, which is a contradiction of the observed scatter in Fig. 4.4. It appears from this plot that there is a smaller variation in the $blue_{20}$ recordings than in the $patch_{10}$ and the $blue_{10}$ recordings, especially when bhj_7301 is excluded. Therefore, it might be interesting to consider the coefficient of variation (CV), which is the standard deviation divided by the mean value.

$$CV_{patch,10} = \frac{4.4}{20.9} = 0.21$$

$$CV_{blue,10} = \frac{4.5}{25.8} = 0.17$$

$$CV_{blue,20} = \frac{4.5}{40.8} = 0.11$$

$CV_{blue,20}$ is considerable lower than the other two values, and is considered to give a more representative impression of the degree of variation.

Ice temperature effect

The plot in Fig. 4.4 indicates that the ice strength increases as the ice temperature is reduced. This holds in particular for the $blue_{20}$ recordings. By studying the values in Tab. 4.4, one see that the same trend holds for the $patch_{10}$ results, yet not for the $blue_{10}$ recordings. Johnston et al. (2003) suggest that ice temperature has strongest effect on the strength when the temperature is above -5°C The results in this section seems to support this statement.

It is also interesting to compare the average strength values of $patch_{10}$ and $blue_{10}$. The values in Tab. 4.4 show that the $patch_{10}$ ice is weaker than the $blue_{10}$ ice within every temperature interval.

Spatial variation

By first sight at the strength variation along the runway length in Fig. 4.3, one might get the impression that the blue ice strength decreases slightly from the western to the eastern part of the runway. However, if one include the average ice temperature measurements from each testing site, the strength seems to vary (roughly) in accordance with the temperature, see Fig. 5.1. In conclusion, the blue ice strength is independent of location.

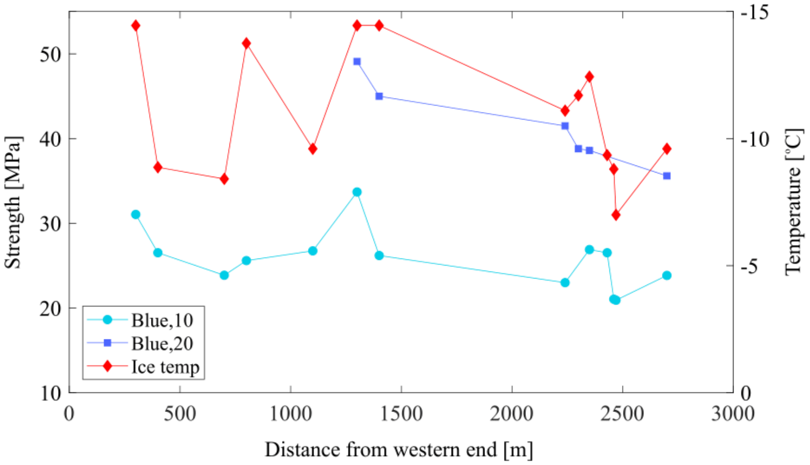

Figure 5.1: Spatial variation of strength along the length axis of the runway, with the average ice temperature for each location included. 0 represents the western end and 3000 represents the eastern end. The airport apron is located in between 2200 and 2450 m.

5.1.2 Failure mode

Fig. 4.11 shows a plot of BHJ strength vs. failure mode size. It appears that the stronger the ice, the higher stress is required to produce a spall of a certain size.

As for the spatial variation, it is interesting to investigate whether ice temperature is effecting the spall size too. Fig. 5.2 shows the failure mode plot for only patch ice results, in where the ice temperature is reported by different colour shadings. Three recordings have been conducted in ice with temperatures above -4°C. None of these measurements produced a spall with crack length exceeding 40 cm, whereas the colder BHJ measurements produced spalls of various sizes. This observation supports the stated theory that warm ice is more ductile than cold ice (Schulson and Duval, 2009). Yet, more data from tempered ice should be collected to confirm this statement.

Similar plots were made for the $blue_{10}$ and $blue_{20}$ results, but the colour shadings appeared to be randomly distributed. This indicates that the ice temperatures have the strongest effect on failure modes for temperatures above -4°C analogous to the effect on ice strength (Johnston et al., 2003).

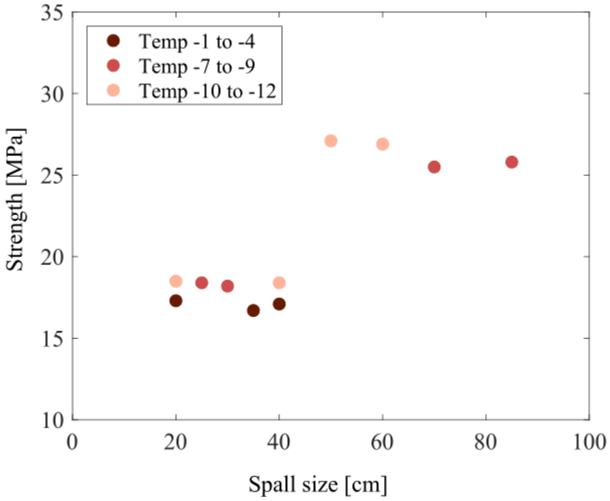

Figure 5.2: BHJ strength vs. spall size for the $patch_{10}$ results. The colour scale indicates the ice temperature.

Different sounds could be heard during the conduction of the BHJ experiments. There were a mixture of long-lasting squeezing-sounds, periodic crushing-sounds and distinct cracking-sounds. Other tests were relative silent, with only smaller periods of sounds. The notes from this observation were rather unsystematic, but a general impression was that the strongest, most brittle ice made the loudest crack-sounds, while the weaker, more ductile ice made long-lasting squeeze-sounds, if any at all. This correspond to the sound tendency observed by Fortt and Schulson (2007); Schulson and Duval (2009) for brittle and ductile failure behaviour.

5.1.3 Comparing $blue_{10}$ and $patch_{10}$ results

Table 5.1: Comparable $patch_{10}$ and $blue_{10}$ results - in location, time and ice temperature

No.	$patch_{10}$	$blue_{10}$
1	bhj_1201 - bhj_1203	bhj_1101 - bhj_1104
2	bhj_4104	bhj_4105 and bhj_4106
3	bhj_6101	bhj_6102
4	bhj_8104	bhj_8101 and bhj_8102
5	bhj_8106	bhj_8107

The BHJ recordings listed in Tab. 5.1 are all conducted under comparable conditions regarding location and time, and thereby also ice temperature. These recordings are particular interesting in the investigation of differences in strength and failure mode between the blue ice and patch ice.

If one compare the ice temperature for all the recordings in Tab.5.1, it becomes evident that the patch ice was warmer than the blue ice within every comparison. Yet, the degree of variation differ. Day 1 stands out as a day with considerable difference in ice temperatures, visualized in the daily temperature plot in Fig. 4.1. On this day, one could really feel that the sun was heating, which explains the significant ice temperature difference that day. During February, the climate gradually changes from summer till autumn, and in the end of the field work period there was little heating effect from the sun.

Because of the dark colour of sand grains, they are known to absorb heat from the sun radiation. If the heating is strong enough, the particles can melt ice in temperatures below 0°C (MacDonell and Fitzsimons, 2008). An important stage in the patching method is to remove all the sand particles in the bottom of the hole before refreezing. However, as illustrated by Fig. 5.3, some particles were often left in the bottom of the patch. This picture also illustrates that the patch ice is in general darker than the surrounding blue ice, but how dark varied for every patch. The patch recordings from day 1 showed that the darkest patch had the highest ice temperature. All together, both particles and the dark ice colour contribute to the increased ice temperature in the patches, especially on days when the heating from the sun is strong. The Troll Airfield personnel have done some research to find the best suited surface cover for the patches; the ice-water mixture or snow, but no conclusion has yet been made.

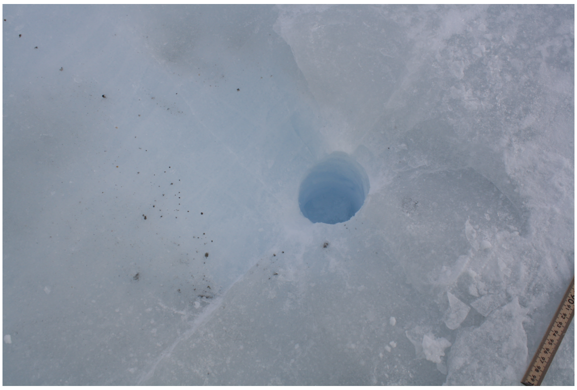

Figure 5.3: Example of sand particles left in the bottom of a patch. The picture is taken from recording bhj_8105.

From the strength values in Tab. 4.3 it is evident that the blue ice is in general stronger than the patch ice, as stated earlier. The strength values of the bhj_1201-bhj_1203 tests are among the lowest, yet not significant weaker than the other patches despite a considerable higher ice temperature.

When comparing the failure mode sizes for the blue ice and patch ice, no systematically difference is observed. This supports the earlier discussed observation, that ice temperatures below -5°C have little effect on the failure modes. Note that comparison no. 1 is not included here because spall size measurements does not exist for bhj_1101-bhj_1104.

The failure behaviour in the stress-time curves have been ranked, and the values are given in Tab. 5.5. It is evident that the behaviour for the blue ice and patch ice is quite similar, illustrated by Fig 5.4. This observation is unexpected for comparison no. 1, where there is a considerable difference in ice temperature. Maybe the strong sun radiation that day effected the blue ice failure behaviour despite the relative cold ice temperatures.

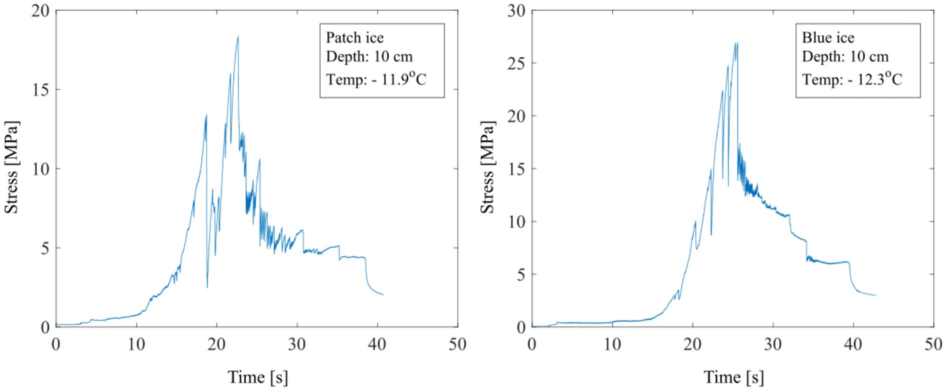

(a) bhj_6101 **(b)** bhj_6102

Figure 5.4: Stress-time curves of comparable BHJ recordings.

5.1.4 Stress evolution after terminal failure

The results are divided into two groups based on the terminal behaviour in the stress-time curve. All the $blue_{10}$ and $patch_{10}$ recordings showed a distinct stress peak, but the stress in most of the $blue_{20}$ recordings continually rose toward a final stress plateau instead. The $blue_{20}$ results are compared to each other, and it is found that whenever no stress peak was obtained, no spalls were produced.

The overlying ice contributes to a confining pressure, which is considerable higher at depth 20 cm than 10 cm. Confinement is known to both increase the strength and alter the failure process (Schulson and Duval, 2009). Thereby is the spalling event partly constrained at depth 20 cm. The higher degree of confinement at 20 cm also makes this ice less sensitive towards natural, localized flaws in the ice, and a smaller scatter in strength values are obtained.

It must be noted that the strength is defined as the maximum recorded stress for all measurements. However, it would maybe be more correct to use the strength definition for flow stress curves for the recordings where the stress continued to increase. According to Sinha (2011), the strength should then be defined as the stress after a certain deformation.

5.1.5 Failure behaviour variation with temperature

In Tab. 4.5, all the $patch_{10}$ and $blue_{10}$ curves are classified based on the failure behaviour. The occurrence of each failure behaviour is plotted against decreasing ice temperature in Fig 5.5.

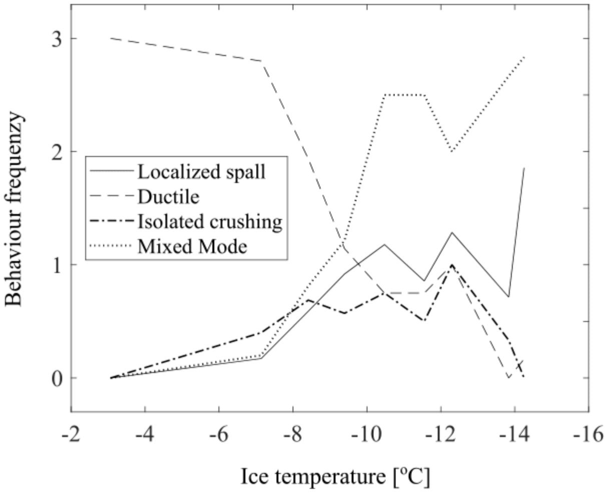

Figure 5.5: Failure behaviour vs. the ice temperature. The lines are represented by the average value for each "hole" temperature. The localized spalls are normalized to the same scale from 0 to 3 as the other categories by multiplying with 3/7.

The behaviour patterns with decreasing ice temperature matches the observations done by Wells et al. (2011) for increasing indentation rates:

- The number of *local spalls* vary within the relevant temperatures, but the trend is that the occurrence is increasing as the ice gets colder.
- The *ductile behaviour* dominates for ice temperatures above -8°C, with reduced severity as the ice gets colder.
- The *isolated crushing* never dominates, but the frequency is highest for ice temperatures in the medium range.
- The *mixed mode* dominates in the colder temperature range, especially when the ice gets colder than -10°C.

It must be noted that the stress drops differ in magnitude. Parts of this difference might be explained by ice induced vibrations because of weaknesses in the equipment. The ice is known to give in when cracks are formed, and it is rather unlikely that the indentation rate, which is supposed to be constant, is unaffected by the sudden lack of resistance. Just before a spall is released, the stress builds up inside the equipment, and when the ice fails, the piston does a small "jump" because of the sudden release in resistance. This is assumed to give an artificial large drop in the stress recording.

In general, the rapid shift in loading/unloading becomes more distinct as the ice temperature decreases. Wells et al. (2011) describe this behaviour as either mixed mode, local spalls or cyclic-load crushing events. O'Rourke et al. (2016) describe another brittle loading pattern called "sawtooth" loading, placed somewhere in between the mixed mode and cyclic loading. Two examples of such behaviour are given in Fig. 4.6. However, the sawtooth loading pattern is described as a periodic, cyclic loading pattern which can be quite regular. The curves in the two examples have varying amplitudes, and the pattern only appears in shorter periods. To answer whether this is sawtooth loading or not requires further investigations, where the possible effect of ice induced vibrations should be included.

Sodhi et al. (1998) found that the transition between ductile and brittle failure is somewhere in the range of ~ 0.3-1 mm s^{-1}. The indentation rate for the newly developed BHJ used in this master thesis is within the suggested transition range. This indention rate is also in the slower part of the rates used by Wells et al. (2011) and O'Rourke et al. (2016). It would be interesting to test the BHJ in even colder temperatures to investigate whether a cyclic loading patterns would appear then.

The penetration depth is also different in the indentation tests conducted by Wells et al. (2011) and O'Rourke et al. (2016) than for the new BHJ. It is the ratio between the penetration depth and the indentor diameter which is interesting. For instance, the indentor used in the experiments conducted by O'Rourke et al. (2016) had a diameter of 20 mm and the penetration depth varied between 2 and 10 mm. The ratio is then in between 0.1-0.5. In comparison is the ratio for the new BHJ at $\sim$1. This must be taken into account if one investigate the terminal behaviour of the stress-time curves or the thickness of the damaged layer.

5.1.6 Bubble density

According to Gagnon and Gammon (1995) is the flexural strength proportional to the bubble density. The pictures from the CT scan in Fig. 4.15-4.17 indicate that the bubble density is higher for the blue ice than the patch ice, which might explain partly why the blue ice is stronger than the patch ice. It must be noted that Gagnon and Gammon (1995) did not suggest any explanation for their statement.

The bubble density for the three CT scanned ice cores are calculated using Eq. 2.1, and in that is the fractional porosity of air (ν) and the mean bubble volume (V_{bubble}) required. Since the ice cores only consist of ice and air, ν is the opposite of SVF:

$$\nu = 1 - SVF, \tag{5.1}$$

where SVF is given for all three cores in Eq. 4.6.4.8.

It is evident from the expression for V_{bubble} in Eq. 2.2 that both the mean short (S) and long (L) bubble diameter are used in Gagnon's calculations, numbers that are not provided by this CT analysis. The best suggestion is to use the average pore diameter, visually taken from the curves in Fig. 4.19. These pore diameters represent the largest sphere one can fit into each bubble, corresponding to S. The calculated bubble densities are given in Tab. 5.2.

Table 5.2: Bubble density calculations for CT scanned ice.

Location	SVF	ν	S [mm]	V_{bubble} [mm^{-3}]	Bubble density
East,10	0.923	0.077	0.40	0.034	2.26
West,10	0.921	0.079	0.40	0.034	2.32
Patch	0.980	0.020	0.35	0.022	0.09

It is evident from the table that the bubble density is higher for the blue ice than the patch ice. However, directly comparison between these results and the bubble densities provided by Gagnon and Gammon (1995) must be done with cation because of the missing *L* measurement.

Then again, both *S* and *L* are given in the paper for the five ice specimens in Fig. 2.1. This enables a back-calculation of the bubble densities if *only* based on *S*. The new bubble densities are given in Tab. 5.3. Basically, all the bubble densities are proportional enlarged, and the linear relationship between the bubble density and the flexural strength is not effected.

Table 5.3: New bubble densities are calculated from the bubble density values given in Gagnon and Gammon (1995), when the bubbles are assumed to have a spherical shape with short diameter. The original bubble densities are given in column 2 for comparison.

Location	Orig. bubble density	New bubble density
G1	1.30	1.60
G2	0.49	0.68
G3	0.40	0.65
G4	3.02	4.40
L	2.66	3.40

The BHJ strength for the blue ice is in general higher than for the patch ice. The findings in this section suggest that the difference in bubble density is a possible explanation for the strength difference.

5.2 Density

The preliminary plan for this field work program included to measure the density at every testing area. But the collecting of the ice cores proved to be challenging. As for the borehole ice drill, the blades on the Kovacs became blunt after short use and had to be sharpened. There were also challenges in collecting continuous ice cores, visualized in Fig. 4.14, and the sampling process proved to be time consuming. Therefore were blue ice cores only collected at three different locations along the runway, and the patch ice only from one location.

To ease the comparison of the density measurements given in Fig. 4.14, a new plot is made where all the densities are plotted against the middle depth of the ice core, see Fig. 5.6.

The vertical line in the plot marks the maximum density for ice (Hobbs, 1974). The density for two of the ice cores are measured to be higher than the maximum limit. The main problem with the mass/volume method was to cut the ends of the ice cores straight to provide an accurate length measurement, and the density values proved to be very sensitive toward the measured core length. For instance, the length of the patch ice core was measured to be 6.6 cm, which resulted in a density of 942.2 kg m^{-3}. If the length was 6.8 cm instead, the density would be 914.5 kg m^{-3}. The uncertainty in the mass/volume method are quantified by Pustogvar and Kulyakhtin (2016) for saline ice specimens, and was found to be $\sim 4\%$.

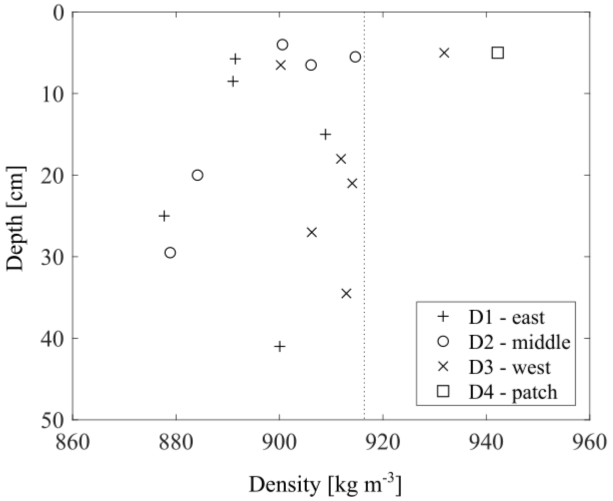

Figure 5.6: Plot of density measurements vs. the middle depth of each core. The results from the different locations are separated by different markers. The vertical line states the maximum density which is physical possible for ice.

In Eq. 4.9-4.11, three other density values are given. These values are more reliable because they are based on SVF calculated by a computer analysis of the X-ray pictures.

The pore size distributions are given in Fig. 4.19a-4.19c, and the shape of the curves for the blue ice specimens are remarkable similar. Since the density values from the two places are almost equal too, an average density of $\sim$ 845 kg m^{-3} is assumed to be representative for the blue ice in general. Likewise, the density of 898 kg m^{-3} for the patch ice is regarded as the best estimate and will be used in the following.

The blue ice density values of 845 kg m^{-3} are within the given density range for glacier ice (Cuffey and Paterson, 2010). So is the patch ice density of 898 kg m^{-3}.

5.3 Thin sections

The grain size measurements reported in Chap. 4.4 must be considered with caution due to the measuring method. A ruler was located next to the sections when the pictures were taken, but this ruler was almost invisible in the photographs. By use of a vector drawing program called Inkscape, a brighter ruler was put on top of the dark one and scaled to provide correct length measurement. This brighter ruler was also used to measure the grain size by simply moving it around in the picture. The grain sizes must therefore only be considered as approximations.

According to Schulson and Duval (2009), the glacier movement can lead to c-axis alignment. It is difficult to decide whether the occasionally observed similarity in grain colours in the blue ice sections are a result of this phenomena, or if it is just a coincident.

An interesting observation for the grain colours in general is that when the thickness of the sections are below 4 mm, the colours start to faint and become more grey. Fig. 5.7 shows pictures of thin section ts_320h at thickness 0.3 and 0.8 mm. This happened for thin section ts_310h and partly for ts_310v, see Tab. 4.6.

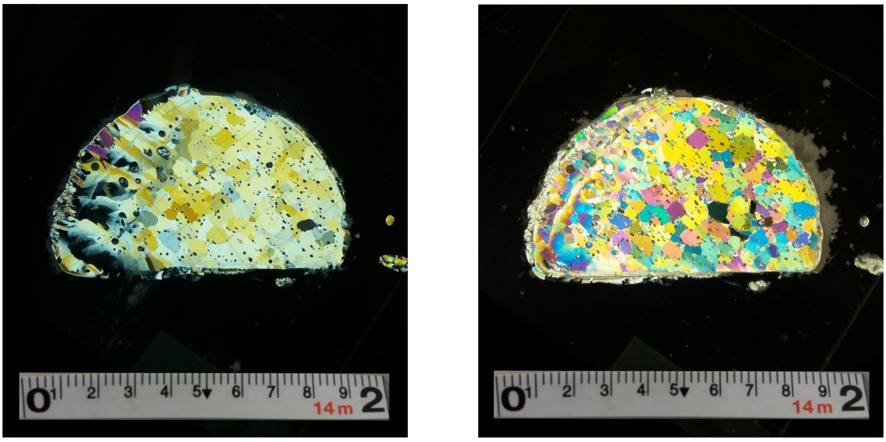

(a) 0.3 mm **(b)** 0.8 mm

Figure 5.7: Pictures of ts_320h with two different section thicknesses.

The grains appear to be distorted along the edge of some of the thin sections, illustrated by the left side of the section in Fig. 5.7a. This is due to melt water produced during the gluing of the ice slab to the heated glass plate, and it becomes more evident when the sections are thinner.

5.3.1 BHJ-sections

Zoomed pictures of the three BHJ-sections are given below, together with the stress-time curves from the corresponding BHJ recording. The red lines indicate the transition between intact blue ice and the damaged layer. This transition is not always clear because the grains are gradually getting smaller towards the centre of the contact zone. The blue lines mark the contact area between the piston and the ice, and it appears that none of them are the fully length of the piston diameter, which is 30 mm. This is because none of the thin sections are cut from the middle of the indented ice. The locations for the vertical cross sections are illustrated by the red dotted lines in the CT scan pictures in Fig. 4.20 and 4.22.

The CT scan pictures (Fig. 4.20-4.22) of the indented ice are interesting to compare to the BHJ sections. The black colour represents air bubbles, and it seems from the pictures that all the air have disappeared from the damage layer. Hence, the indentor load must have compressed the pores in addition to recrystallize the grain structure. This observation will not be further elaborated, limited by the scope of this master thesis.

Tab. 5.4 gives a summary of the layer thickness and grain sizes given in Chap. 4.4, including the length of the blue line.

Table 5.4: Summary of all the damage layer measurements. The length of the blue line provide information about the distance from the thin section to the middle of the indentor mark. The diameter of the indentor is 3 cm.

Thin section	Blue line	Layer thickness	Grain size
ts_7101v	1.5 cm	2 cm	0.3-2 mm
ts_8103h	1.0 cm	0.4 cm	0.3-1 mm
ts_9101v	2.6 cm	1.5 cm	0.5-2 mm

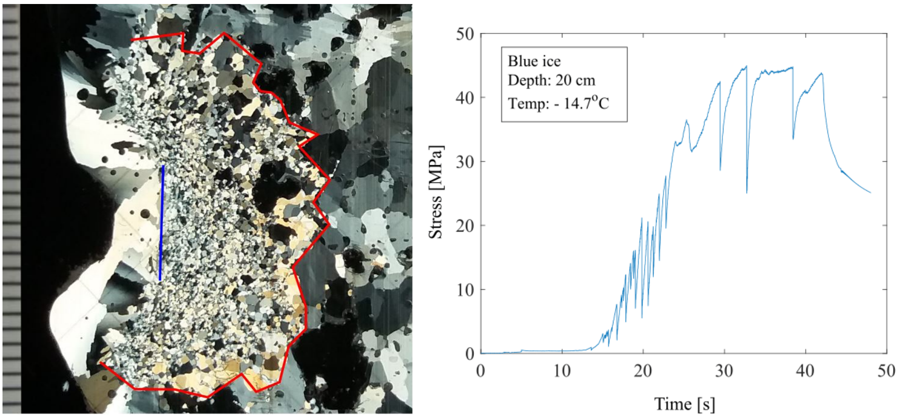

(a) ts_7101v **(b)** bhj_7101

Figure 5.8: Zoomed picture of thin section ts_7101v with the corresponding BHJ stress-time curve. The spacing in the ruler is 2 mm.

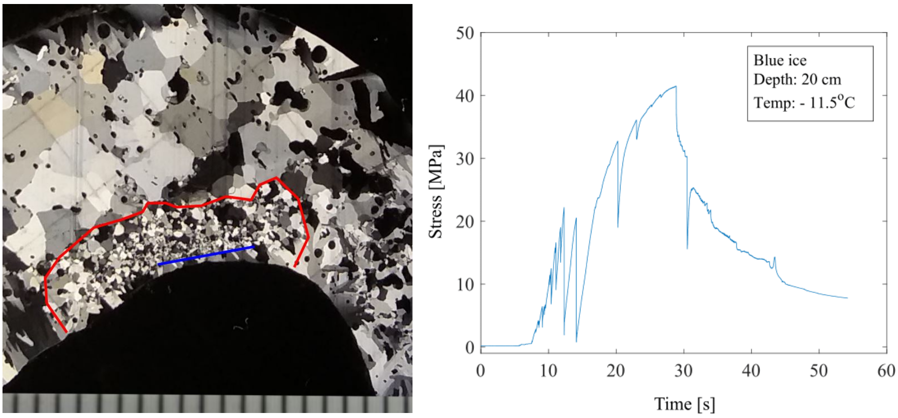

(a) ts_8103h **(b)** bhj_8103

Figure 5.9: Zoomed picture of thin section ts_8103h with the corresponding BHJ stress-time curve. The spacing in the ruler is 2 mm.

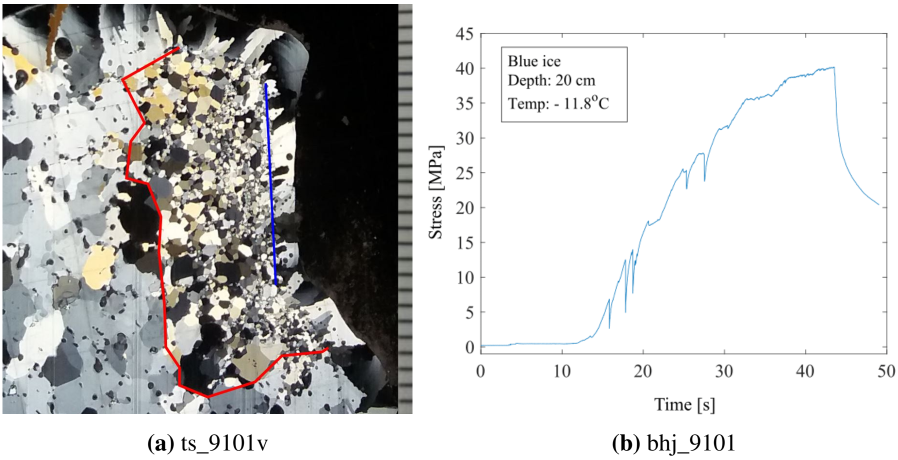

(a) ts_9101v **(b)** bhj_9101

Figure 5.10: Zoomed picture of thin section ts_9101v with the corresponding BHJ stress-time curve. The spacing in the ruler is 2 mm.

First are the two vertical sections ts_7101v and ts_9101v compared. Section ts_7101v measured the thickest damaged layer, despite that the blue line in this section was the shortest of the two and this section was taken furthest away from the centre. The failure behaviour in the bhj_7101 recording also showed the greatest severity of sawtooth loading. This corresponds to the statement by O'Rourke et al. (2016), that sawtooth loading contributes to structure modification and produces a thicker layer.

The blue line of the horizontal section ts_8103h is only 1 cm, which means that the thin section is taken almost along the edge of the indentor zone. This layer thickness is considerable thinner than found in the two other BHJ sections. This might be explained by the location along the edge or that this section is a horizontal cut rather than a vertical cut. Another possible explanation is that the failure behaviour in the stress-time curve is dominated by local spalls rather than sawtooth loading. O'Rourke et al. (2016) have stated that spalling results in reduction of the contact area rather than layer activity.

An attempt of observing microcracks in the thin sections were performed, but it failed because the correct method was not known at the time. If the correct procedure had been applied, one could have studied the distribution of recrystallized grains and microcracks in the damaged layer. According to literature one expect to find recrystallized ice in the centre of the contact area and microcracks along the edge (Barrette et al., 2002). However, the amount of microcracks are said to increase with brittle failure behaviour (Browne et al., 2013). As discussed earlier, the indentation rate in these BHJ experiments were rather slow, implying a domination of recrystallization. Further, if one look at the pictures of the zoomed BHJ-sections, the grains seem to be intact and show different colours. According to Barrette et al. (2002), this is an indication of recrystallized ice.

The findings in this section are interesting, yet more BHJ-sections should be studied to support the argumentation. Two more thick sections of indented ice *were* brought back to Trondheim, but the irregular shape made it difficult to make thin sections out of them. It was in general challenging to collect samples of the indented ice. Firstly because it was only possible to collect samples from recordings where no spalls had been produced. And secondly, the indentation area proved to be fragile, and often only fragments of ice were collected rather than full length cores.

5.4 Russian snow penetrometer

The curve in Fig. 3.16 presents minimum requirements for the RSP index depending on the tire pressure of different aircrafts. The highest value is in between 60 and 70 kg, and 70 kg will therefore be used as the critical limit. If one compare the RSP results presented in Chap. 4.6 with this limit, it is clear that all obtained RSP results from Troll Airfield exceeded this value with good margin.

However, there were some concerns regarding the testing procedure and the relevance of this test. The reason that there were no blow sets deeper than 10 cm is that the hammer started to bounce at the anvil instead of penetrating the ice at this depth. This often happened before 10 cm, but then the bouncing ended after a few hammer drops because a spall was released. Another observation during the testing was that the penetrometer shaft had a tendency to be skew. The inclination became greater as the hammer dropping continued. The U.S. Army Corps of Engineers (2015) standard procedure did not say whether to end the test, continue or straighten up the shaft before continuing. This will give a variation in the result dependant on the person conducting the test. The calculated average RSP index at 274 kg (see Eq. 4.12 is very high when compared to the requirement of 70 kg, and the results within the same testing areas were inconsistent. All this considered, a general thought was that the runway ice on Troll Airfield was too hard for this test.

After the field program was finished, more information about the RSP procedure has been given from CRREL. These procedures are extensively used for strength characterization at American runways located in Antarctica. The new information is relevant for the assessment of the RSP results obtained at the Troll Airfield. There are in particular three points that must be emphasized:

1. The RSP test is not suited for ice material with density lower than 450 kg m^{-3} and larger than 750 kg m^{-3}.
2. When assessing the mean value of the RSP index along the depth, the upper blow set should be excluded because of lack of confinement.
3. If more than 10 drops are required to penetrate 25 mm, the test has reached refusal and should be ended.

First of all, the density of the blue ice is measured to be 845 kg m^{-3}, which is exceeding the suggested density range for the RSP test. Secondly, the first blow set is irrelevant because of lack if confinement. From Fig. 4.23 one can see that the results from the first blow sets were the only ones even close to the critical limit of 70 kg. The first sets were also included in the final RSP indexes given in Tab. 4.9 and in the average value in Eq. 4.12. These values would be even higher than reported if the first blow sets were excluded. The third item states that the test should be ended when number of blows are more 10 pr. blow set. From Tab. 4.9 it is evident that this was the case for several blow sets.

In total, this gives an explanation to the high RSP values obtained at the Troll Airfield. The density exceeded the suggested density range, and the ice is too compact to allow sufficient penetration. As mentioned earlier, the penetration was often driven by production of spalls. Fault cracks are initiated along natural flaws in the ice structure, and it seems that the local variation in the ice structure has a strong effect on the RSP index. This is a plausible explanation for the high degree of randomness in the obtained RSP indexes. In total, the RSP test seems inappropriate for characterization of the runway strength at Troll Airfield.

Attempts of finding a correlation between the RSP and the BHJ results, and between the RSP index and ice temperature have been conducted. No correlation were obtained in neither attempts because of the randomness in the RSP results. Due to the general irrelevance of the RSP test, these attempts have not been pursued.

Chapter 6

Further work

6.1 Runway ice strength

The indentation load factor *c* is currently based on a theoretical derivation, and the magnitude of the BHJ strength values are therefore only valid for relative comparison with each other. However, a calibration tool is under development. This device will provide an accurate value of *c*. All the reported stress values in this project should be adjusted with the correct factor when it is determined.

To extend the application of the measured runway strength, a critical strength value should be determined. Analyses of the runway with relevant load situations can be performed by use of a finite element simulation program, for instance PLAXIS. A suited material model for ice should be implemented in the analysis. Yet, the complexity of the stress state during an indentation test must be kept in mind when comparing the obtained critical strength values with the measured BHJ strength.

It is argued in the discussion that ice strength is reduced when the temperature increases, in particular for temperature above $\sim$ -5°C. Further testing of tempered ice is important since this seems to be the most critical condition, and data from only three such measurements exist. Moreover, if a critical BHJ strength is determined, it might be possible to find a critical temperature range where the strength is approaching the critical limit.

Patching method

The temperature in the patches increases with rising air temperature, in particular if combined with sun radiation. The effect of dark particles left in the bottom of the hole should be further examined, as they seem to cause the difference in ice temperature between the patch ice and the blue ice. Also, further investigation of the best suited surface cover should be continued. The objective is to imitate the bright colour of the surrounding blue ice to reduce the heat absorption in the patches.

6.2 Testing equipment

Borehole jack

The BHJ is recently developed and has never before been used in the field. A few adjustments for the equipment are therefore suggested to improve the functionality:

- The ice drill used in the borehole production should transport all the crushed ice to the surface. If so, one would not have to stick the arm into the borehole and remove the ice manually, and one could make deeper measurements.
- The grey wires between the load cells and the data logger are unnecessary long, and the connection between the load cells and wires are fragile. It would be very practical if the data logger was attached to the steel cylinder and the grey wires were shortened. This would reduce the number of loose items.
- The foam inside the transportation box should be properly adjusted after the shape of the jack. The lifting and moving of the box in the field would then be simplified.
- The already mentioned calibration tool should be included in the field equipment. If so, the indentation load can be constantly calibrated. Any effects of temperature changes and long time use on the friction inside the jack will then be detected.

Russian snow penetrometer

It is concluded in the discussion in Chap. 5.4 that the RSP is not suited for runway strength measurement at Troll Airfield. However, one RSP test was performed in a recently made patch, rsp_7206. The hardness index from this test was 120 kg, which is within the normal range of RSP values. It might be worth looking into whether the RSP test can be used to assess the patch ice strength when the patches are fresh or when the ice temperature is closing up to 0°C during summer. Tempered ice is expected to be more ductile. Yet, the density will still be out of range. This should be further discussed with the CRREL personnel who have more experience with the RSP test.

6.3 Scientific research

A further investigation of the correlation between sawtooth loading and layer thickness is suggested. The damaged layer has been widely investigated for indentation experiments performed in cold laboratories, yet little or no literature exist on such experiments conducted in field.

The additional information of air bubbles provided by the CT scan pictures are very interesting in company with the thin section photographs. A study of the relationship between the compressed air bubbles and the damaged layer might add a new perspective of the failure processes in this zone.

Chapter 7

Conclusion

This chapter is divided into two sections; a practical part and a scientific part. The practical part summarizes the most important conclusions for the management of the Troll Airfield, and the scientific part presents the most interesting conclusions for the scientific research.

7.1 Practical

The blue ice is in general stronger than the patch ice. However, when the ice temperatures are within the same range, the difference in strength is insignificant. It must be noted that most of the BHJ recordings were performed in ice temperatures below -7°C. Recordings performed in ice with temperature above $\sim$ -5°C indicate that this ice is weaker and more ductile than colder ice, which is supported by literature. More experiments should be performed in tempered ice to investigate how the strength evolves when the ice temperature approaches 0°C.

On days when one could feel the heat from the sun, the temperature in the patch ice was considerable higher than in the blue ice. Furthermore, the patch ice proved to be weaker than the blue ice on these days. The temperature difference is explained by sand particles left in the patch, and the darker colour of the patch ice. The darker colour is known to absorb more heat.

Table 7.1: Characterization of the blue ice and patch ice

Characteristics	Blue ice	Patch ice
Density	845 kg m^{-3}	898 kg m^{-3}
Structure	granular	granular
Grain size	4-5 mm	1-7 mm
Grain elongation	moderate vertical elongation	none
Anisotropy	small degree	none

A summary of the obtained characterizations of the runway ice are given in Tab. 7.1. The properties of the blue ice, including strength, structure and density, are found to be consistent along runway length.

Runway monitoring program

The BHJ experiment can be used to investigate the development of the runway strength and to compare the relative strength of different ice types. Yet, the *magnitude* of the strength can only be utilized when the correct indentation load factor c is determined. The theoretical derived value of c is 1.99, which has been used in this thesis.

The experimental setup for the BHJ test is per now too inconvenient and time consuming to be a part of a standard monitoring program. A few adjustments of the BHJ equipment are suggested to ease the testing procedure, and standards for data analyses should be developed.

The RSP test is not suited for runway strength investigations at Troll Airfield because the density is exceeding the recommended density range and the ice appears to be too hard. Having said that, whether the RSP test can be utilized in tempered ice during the summer season should be investigated.

The physical properties given in Tab. 7.1 can be used to estimate ice strength parameters. The uniaxial and triaxial ice strength is extensively quantified based on these properties, an these strength parameters might be easier to implement in a runway simulation than the BHJ strength. Realistic strength values of the runway ice can thereby be estimated, provided that the ice temperature is known. In conclusion, a combination of a runway simulation and simple ice temperature measurements might prove to be sufficient to assess the runway conditions.

7.2 Scientific

The blue ice strength is found to increase with depth, and the confinement at depth 20 cm is high enough to suppress spalling. Furthermore, the coefficient of variation decreases with depth, which is reflected in the reduced scatter in the obtained strength values.

The spall size measurements suggest that the failure modes are more ductile for temperatures above $\sim$ -5°C, and become more brittle when the temperature decreases. In the study of the failure behaviour in the stress-time curves, it is found that decreasing ice temperature has the same effect as increasing indentation rate.

Brittle failure behaviour are recognized as rapid shifts in loading/unloading. In particular is a partly cyclic loading pattern described, commonly referred to as sawtooth loading. This loading mechanism is only observed occasionally, and it is questioned whether the pattern is regular enough to be defined as "sawteeth".

Three thin sections were made of the indented ice, and it was found that greater severity of the possible sawtooth loading resulted in a thicker damaged layer. In X-ray pictures of the damaged layer, it was found that the air pockets in the damaged layer were closed.

Bibliography

Barrette, P., Pond, J., Jordaan, I., 2002. Ice damage and layer formation in small-scale indentation experiments. In: Ice in the Environment: Proceedings of the 16th IAHR International Symposium on Ice, Dunedin, New Zealand, Dec. 2–6, 2002. Vol. 3. pp. 246–253.

Browne, T., Taylor, R., Jordaan, I., Gürtner, A., 2013. Small-scale ice indentation tests with variable structural compliance. Cold Regions Science and Technology 88, 2–9.

Cuffey, K. M., Paterson, W. S. B., 2010. The physics of glaciers. Academic Press.

Fortt, A., Schulson, E., 2007. The resistance to sliding along coulombic shear faults in ice. Acta materialia 55 (7), 2253–2264.

Gagnon, R., Gammon, P., 1995. Characterization and flexural strength of iceberg and glacier ice. Journal of Glaciology 41 (137), 103–111.

Hobbs, P. V., 1974. Ice Physics. Oxford University Press Inc., New York.

Johnston, M., Timco, G., Frederking, R., 01 2003. In situ borehole strength measurements on multi-year sea ice.

Jones, S. J., 1982. The confined compressive strength of polycrystalline ice. Journal of Glaciology 28 (98), 171–178.

Jordaan, I. J., 2001. Mechanics of ice–structure interaction. Engineering Fracture Mechanics 68 (17-18), 1923–1960.

MacDonell, S., Fitzsimons, S., 2008. The formation and hydrological significance of cryoconite holes. Progress in Physical Geography 32 (6), 595–610.

O'Rourke, B. J., Jordaan, I. J., Taylor, R. S., Gürtner, A., 2015. Spherical indentation tests on confined ice specimens at small scales. In: ASME 2015 34th International Conference on Ocean, Offshore and Arctic Engineering. American Society of Mechanical Engineers.

O'Rourke, B. J., Jordaan, I. J., Taylor, R. S., Gürtner, A., 2016. Experimental investigation of oscillation of loads in ice high-pressure zones, part 1: Single indentor system. Cold Regions Science and Technology 124, 25–39.

Pustogvar, A., Kulyakhtin, A., 2016. Sea ice density measurements. methods and uncertainties. Cold Regions Science and Technology 131, 46–52.

Renshaw, C. E., Schulson, E. M., 2001. Universal behaviour in compressive failure of brittle materials. Nature 412 (6850), 897.

Rist, M., Murrell, S., 1994. Ice triaxial deformation and fracture. Journal of Glaciology 40 (135), 305–318.

Schulson, E., 1990. The brittle compressive fracture of ice. Acta Metallurgica et Materialia 38 (10), 1963–1976.

Schulson, E., Duval, P., 2009. Creep and Fracture of Ice. Cambridge University Press.

Sinha, N. K., 1991. In situ multi-year sea ice strength using nrcc borehole indentor. In: Proc. 10th. Int. Conf. Offshore Mechanics and Arctic Engineering (OMAE/ASME), Stavanger, Norway. Vol. 4. pp. 229–236.

Sinha, N. K., 2011. Borehole indentor-a tool for assessing in-situ bulk ice strength and micromechanics. Cold Regions Science and Technology 69 (1), 21–38.

Sodhi, D. S., Takeuchi, T., Nakazawa, N., Akagawa, S., Saeki, H., 1998. Medium-scale indentation tests on sea ice at various speeds. Cold Regions Science and Technology 28 (3), 161–182.

Sund, M., Guldahl, J., 2007. Technical Report on Troll Airfield, Dronning Maud Land, Antarctica. .

Timco, G., Weeks, W., 2010. A review of the engineering properties of sea ice. Cold regions science and technology 60 (2), 107–129.

U.S. Army Corps of Engineers, 2015. Design, Construction, Maintenance, and Evaluation of Snow and Ice Airfields in Antarctica.

Wells, J., Jordaan, I., Derradji-Aouat, A., Taylor, R., 2011. Small-scale laboratory experiments on the indentation failure of polycrystalline ice in compression: Main results and pressure distribution. Cold Regions Science and Technology 65 (3), 314 – 325.

Appendices

A Testing areas

This appendix presents small maps over all the different testing areas. These areas are all located at the runway at Troll Airfield, see overview map in Fig. 3.1.

All testing areas are numbered *X.Y*, where *X* gives the testing day and *Y* gives the testing area for that day, following the same system as in the overview map. All the BHJ and the RSP tests performed in each area are numbered B1-B8 and R1-R8, respectively. For example, bhj_5101 will be found in map number 5.1 as B1, and rsp_3402 will be found in map 3.4 as R2. Fig. A.1 gives a further explanation of the different symbols in the maps.

Thin sections have been made of the indented ice from three BHJ tests, and these tests have been marked with "+TS".

○ BHJ test at depth 10 cm

◎ BHJ test at depth 20 cm

□ RSP test

● A patch

Figure A.1: Explanation of symbols used in the testing area maps.

The scale in each testing area vary a lot. Arrows are therefore given between a few measurements to give an idea of the dimensions. But it must be noted that this scale, and also the relative position within each map, are only based on visual estimates.

1.1

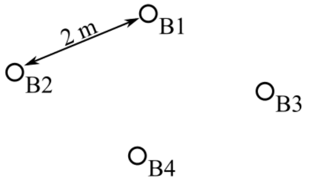

1.2

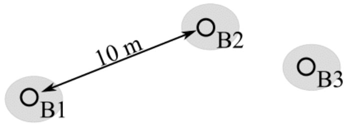

2.1

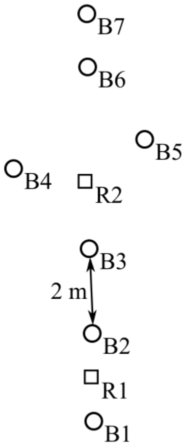

2.2

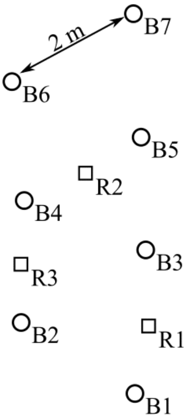

2.3

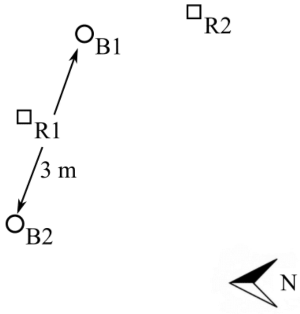

2.4

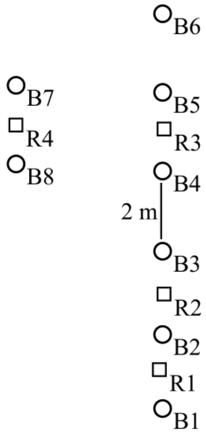

3.1

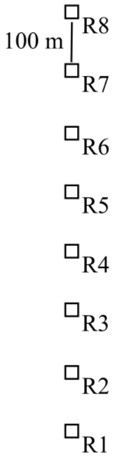

4.1

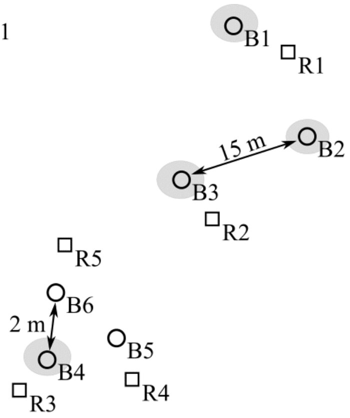

5.1

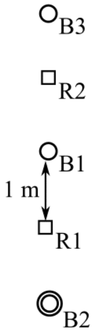

6.1

7.1

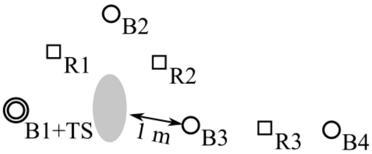

7.2

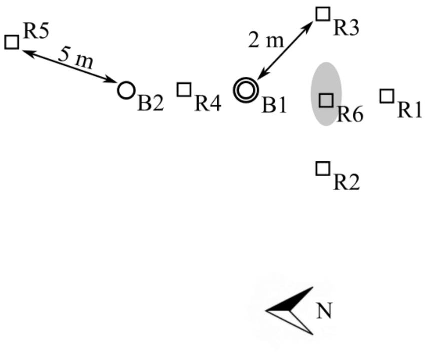

7.3

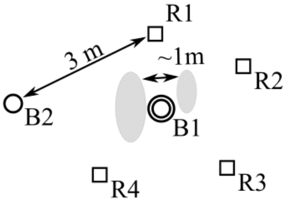
R1
3 m
~1m
R2
B2
B1
R4
R3

7.4

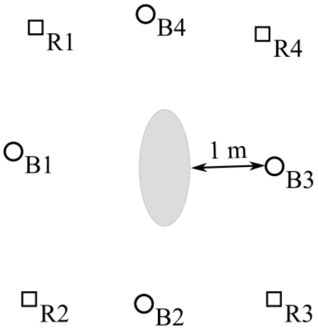
R1
B4
R4
B1
1 m
B3
R2
B2
R3

8.1

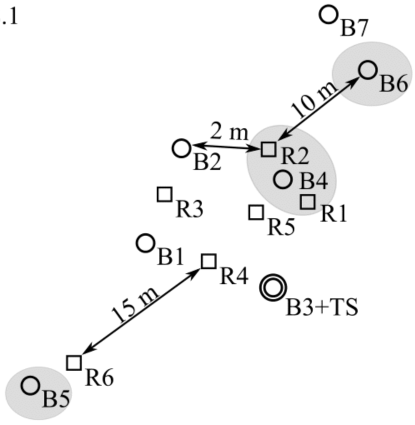
B7
B6
10 m
2 m
B2
R2
B4
R3
R5
R1
B1
R4
15 m
B3+TS
R6
B5

9.1

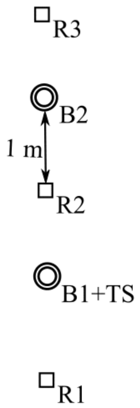
R3
B2
1 m
R2
B1+TS
R1


N

B Borehole jack results

A collection of all the BHJ results are presented in this appendix. This includes the stress-time curves and pictures of the failure mode for those recordings where such are available.

bhj_1101

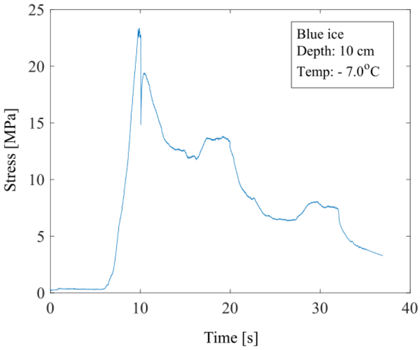

bhj_1102

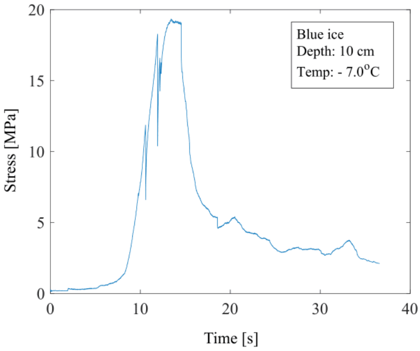

bhj_1103

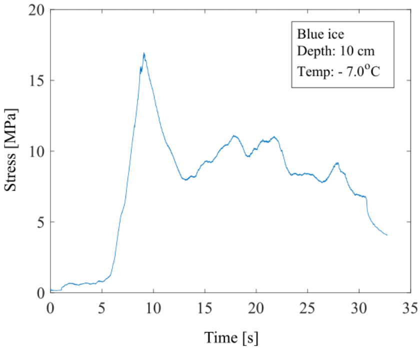

bhj_1104

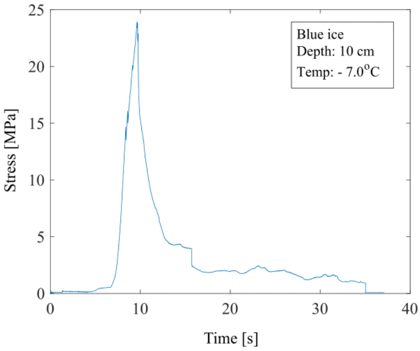

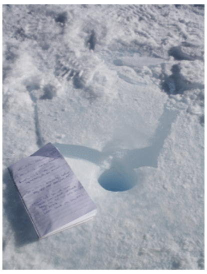

bhj_1201

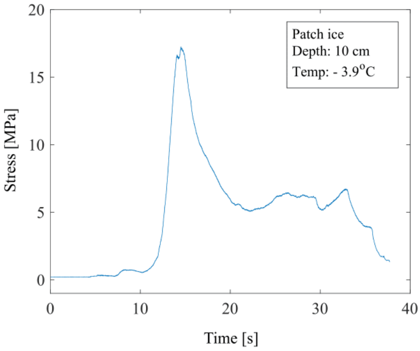

bhj_1202

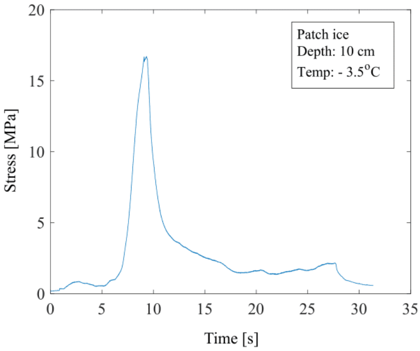

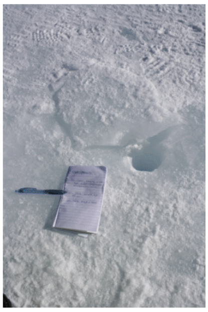

bhj_1203

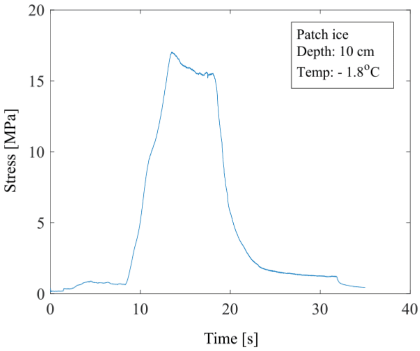

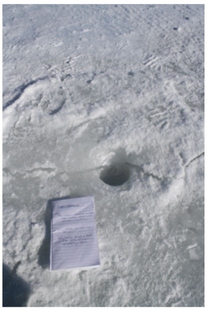

bhj_2101

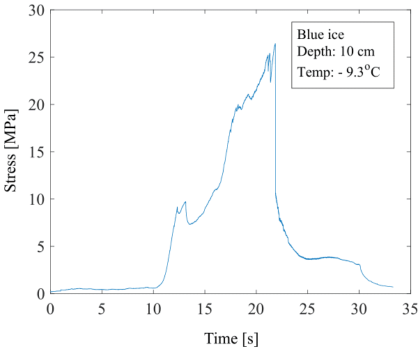

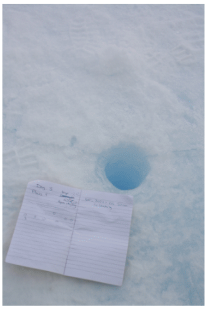

bhj_2102

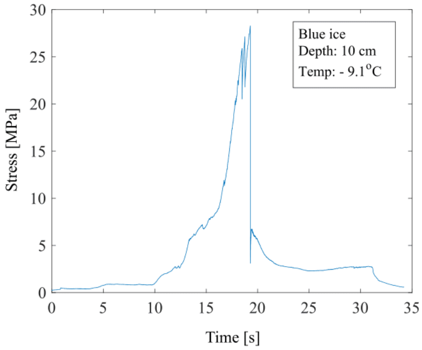

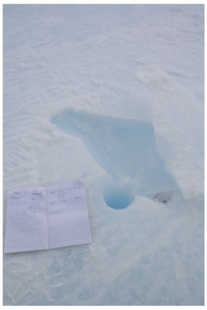

bhj_2103

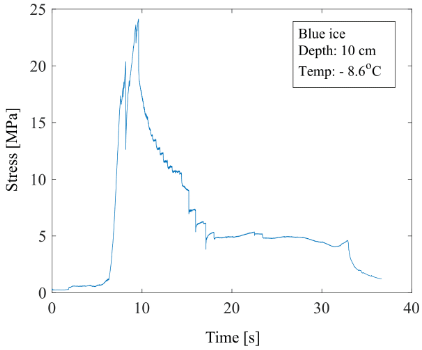

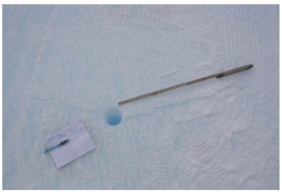

bhj_2104

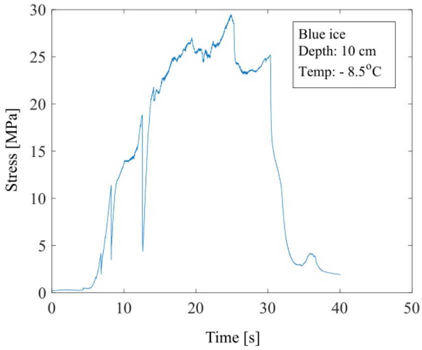

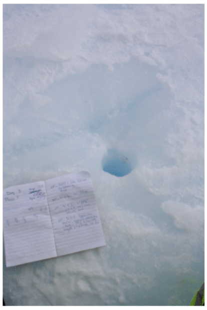

bhj_2105

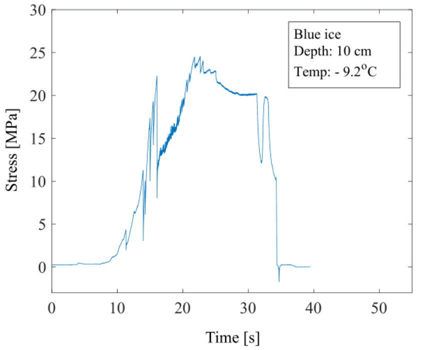

bhj_2106

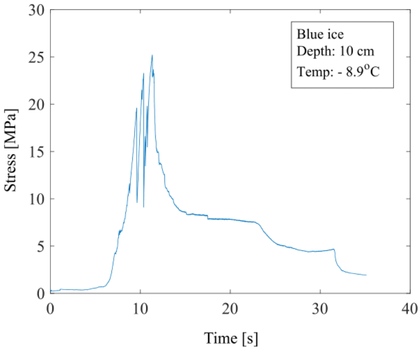

bhj_2107

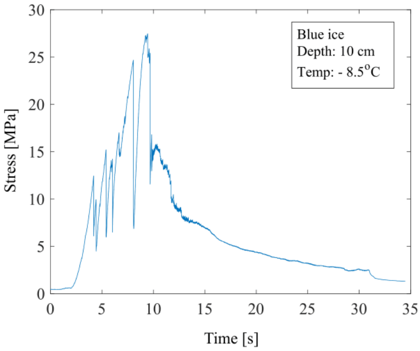

bhj_2201

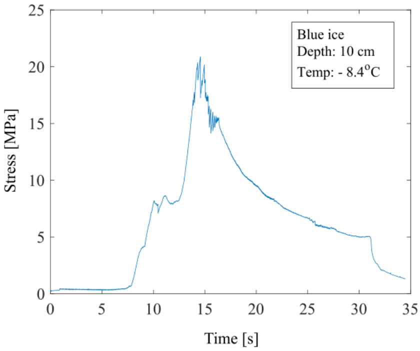

bhj_2202

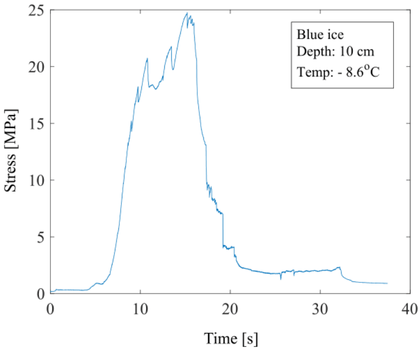

bhj_2203

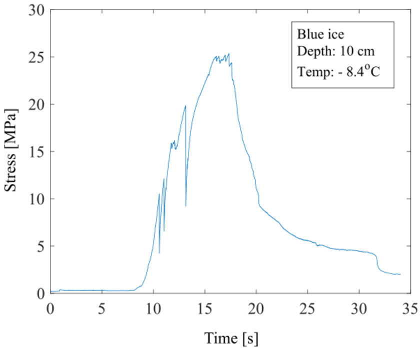

bhj_2204

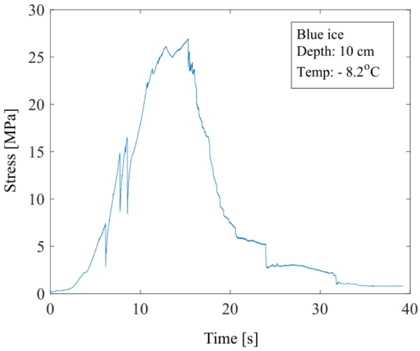

bhj_2205

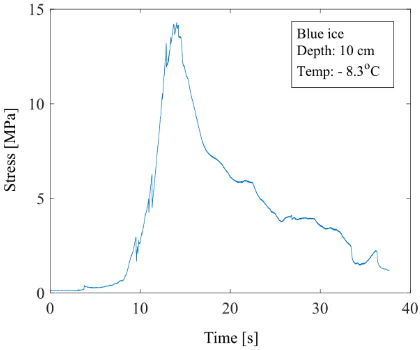

bhj_2206

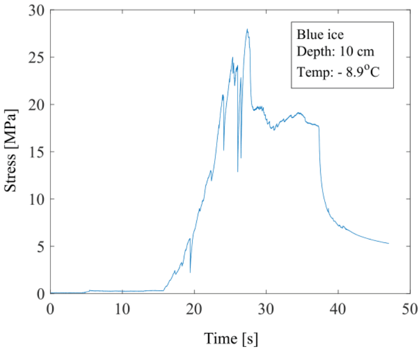

bhj_2207

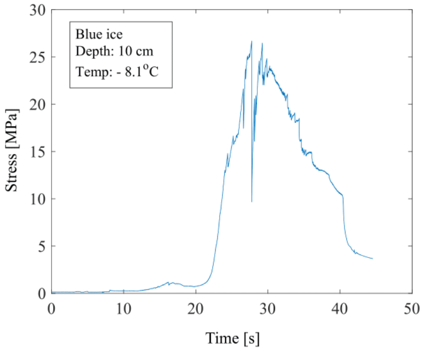

bhj_2301

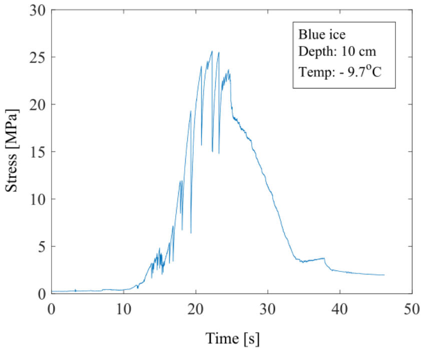

bhj_2302

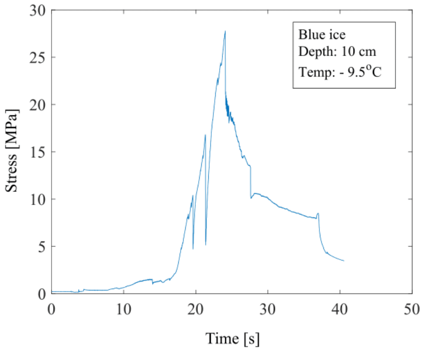

bhj_2401

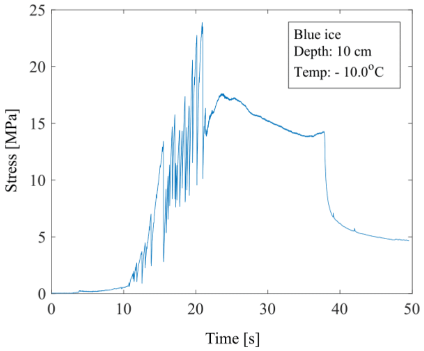

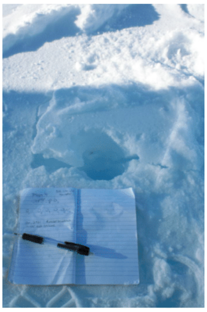

bhj_2402

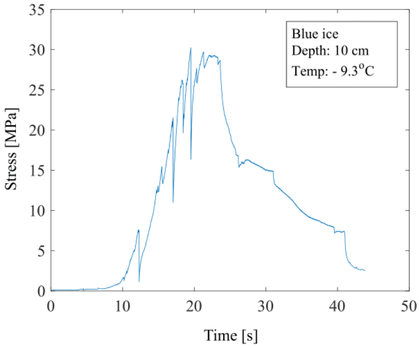

bhj_2403

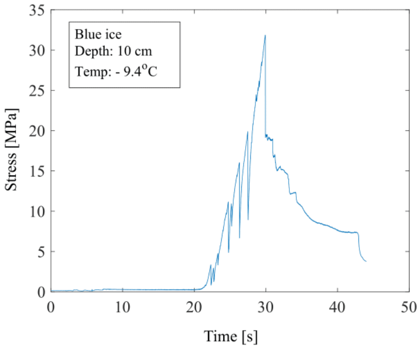

bhj_2404

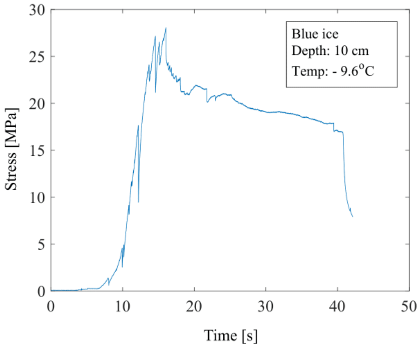

bhj_2405

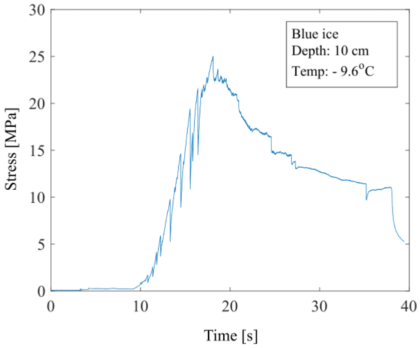

bhj_2406

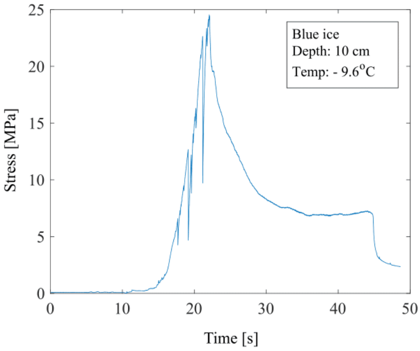

bhj_2407

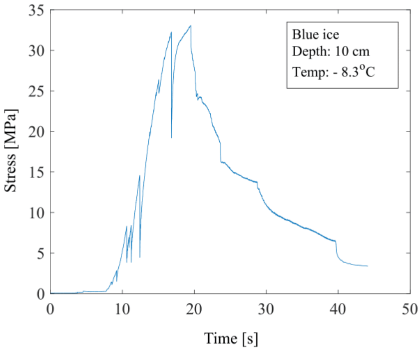

bhj_2408

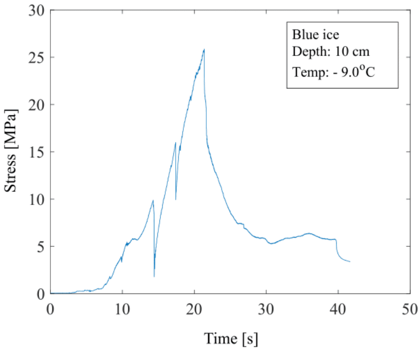

bhj_4101

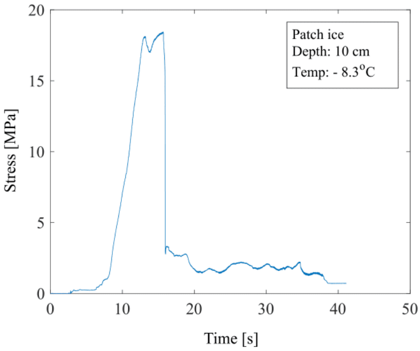

bhj_4102

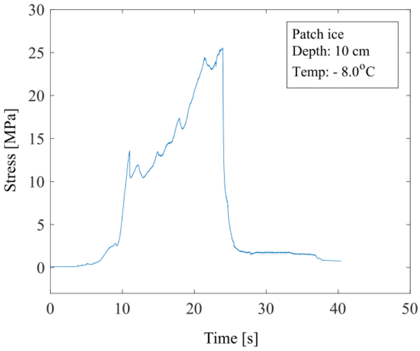

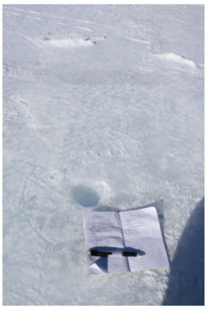

bhj_4103

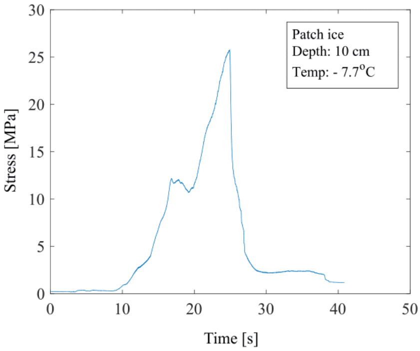

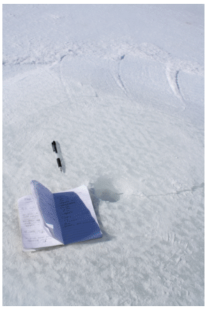

bhj_4104

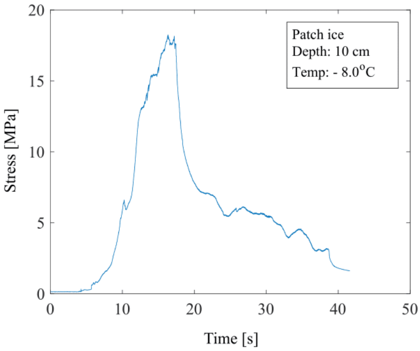

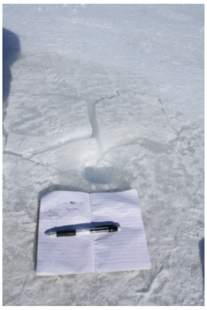

bhj_4105

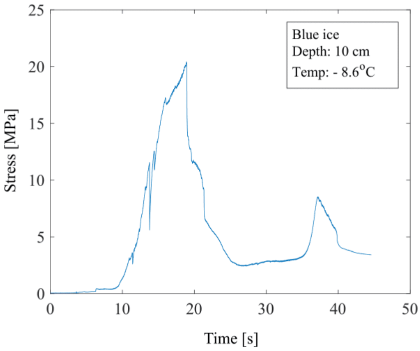

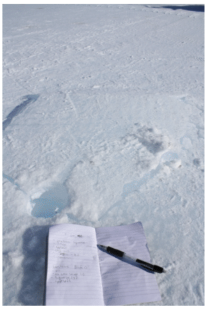

bhj_4106

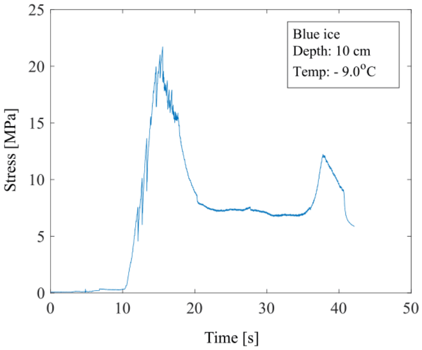

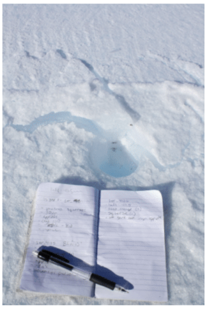

bhj_5101

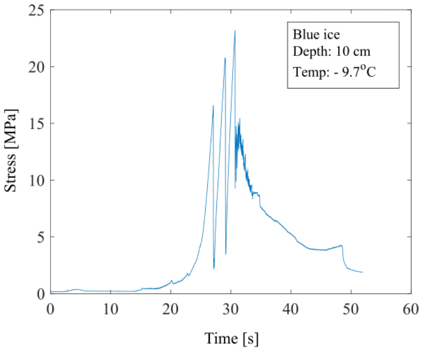

bhj_5102

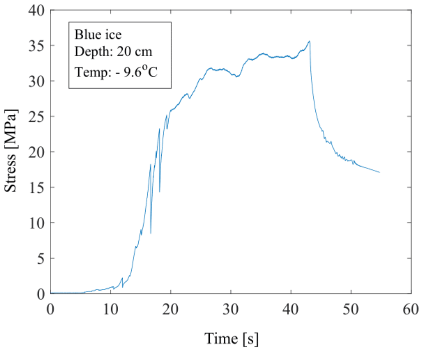

bhj_5103

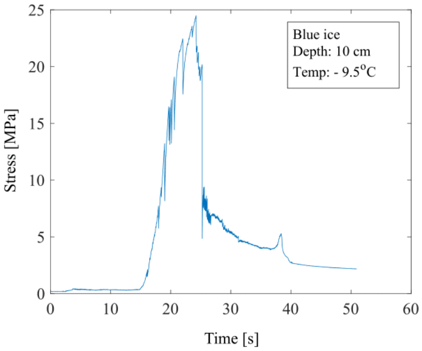

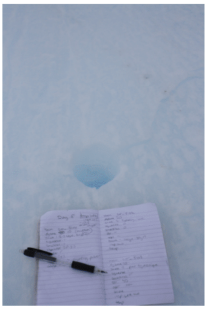

bhj_6101

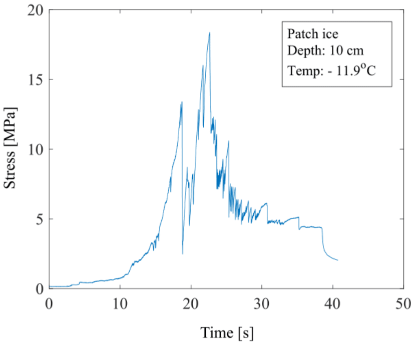

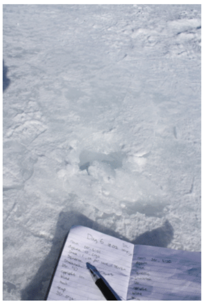

bhj_6102

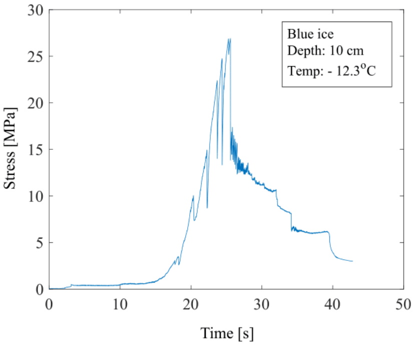

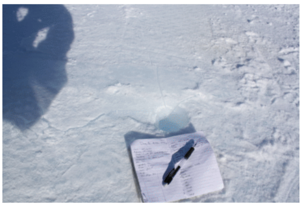

bhj_6103

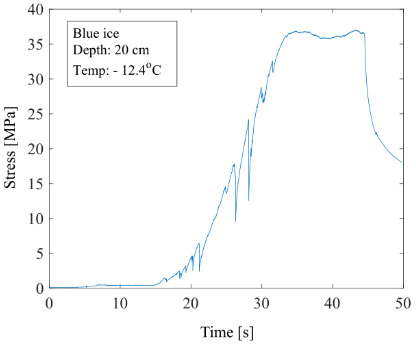

bhj_6104

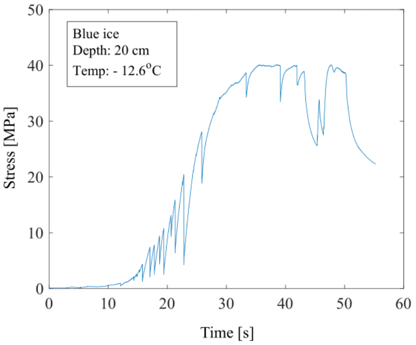

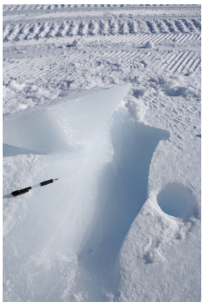

bhj_7101

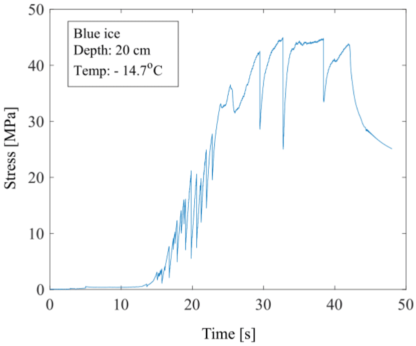

bhj_7102

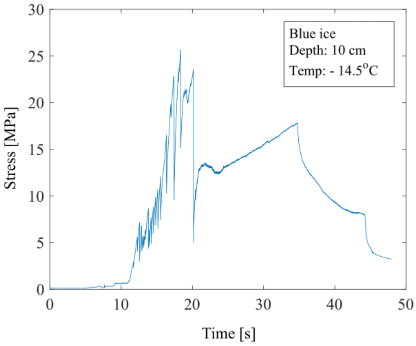

bhj_7103

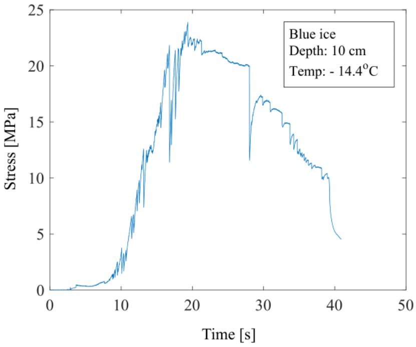

bhj_7104

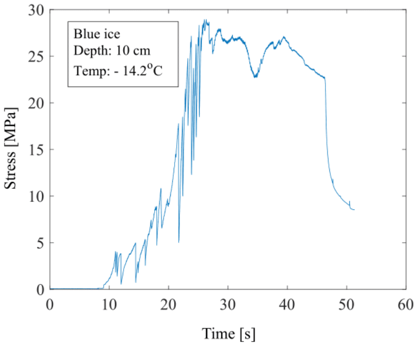

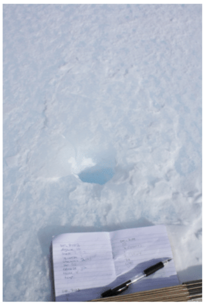

bhj_7201

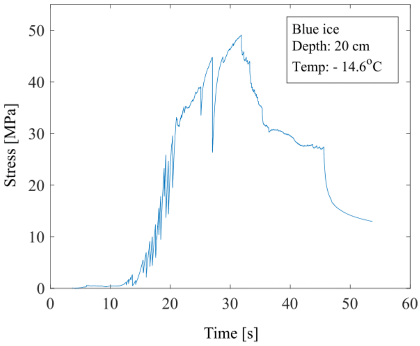

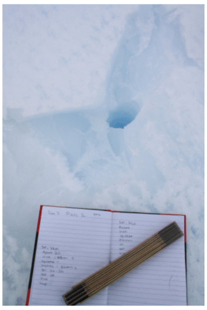

bhj_7202

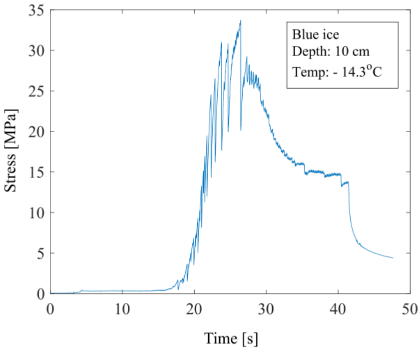

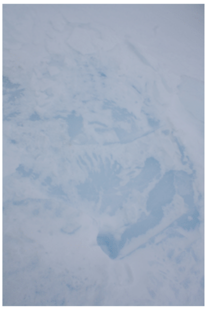

bhj_7301

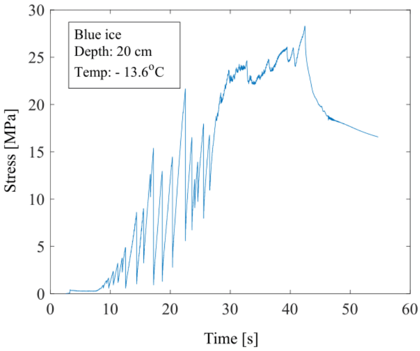

bhj_7302

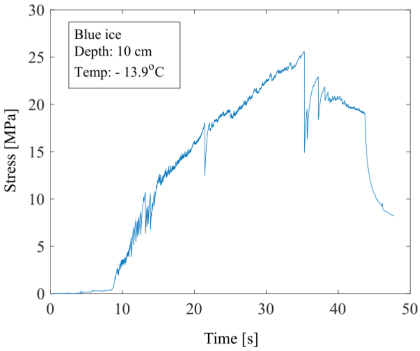

bhj_7401

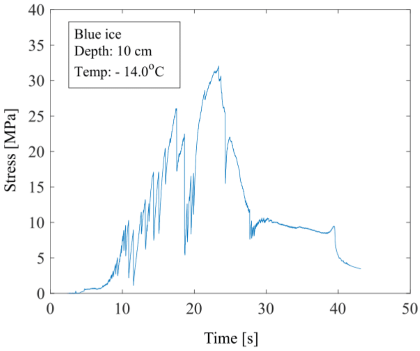

bhj_7402

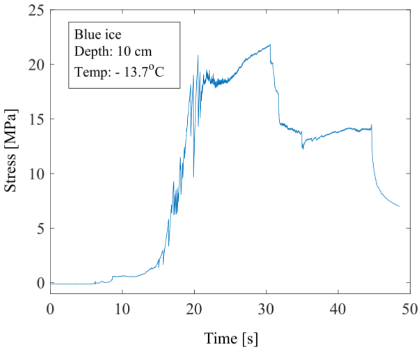

bhj_7403

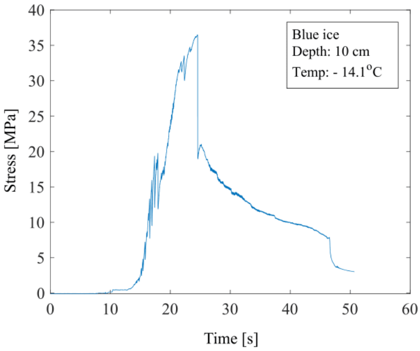

bhj_7404

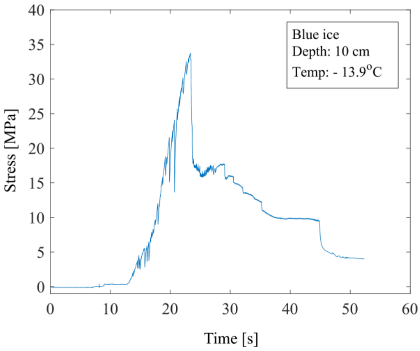

bhj_8101

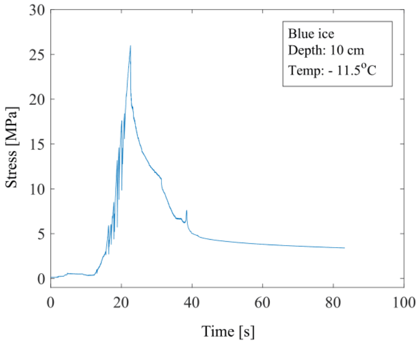

bhj_8102

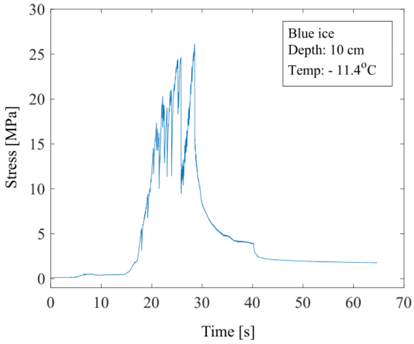

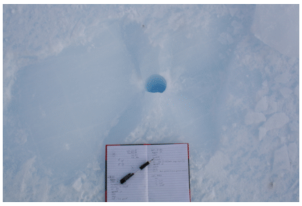

bhj_8103

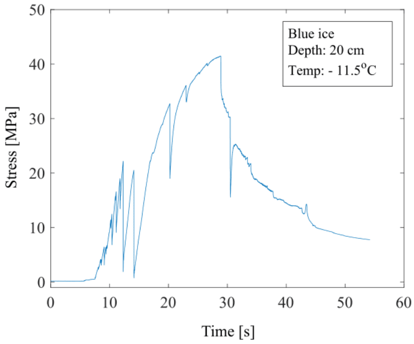

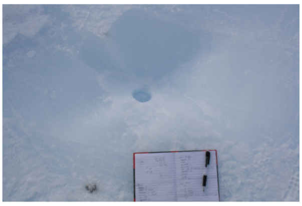

bhj_8104

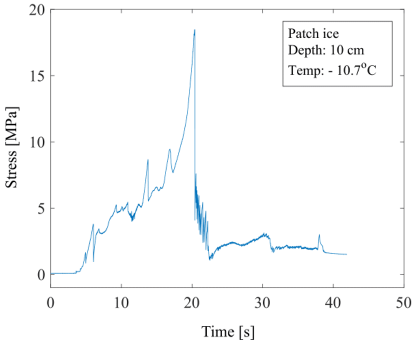

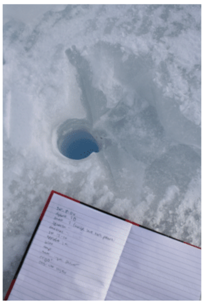

bhj_8105

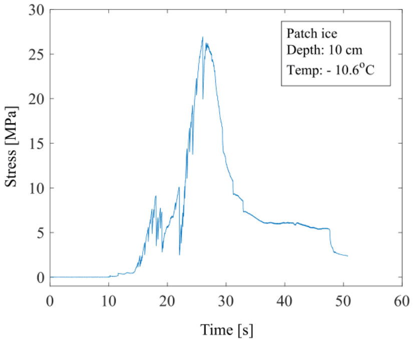

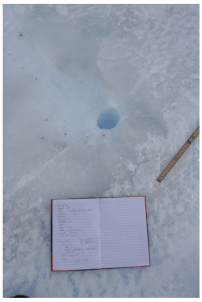

bhj_8106

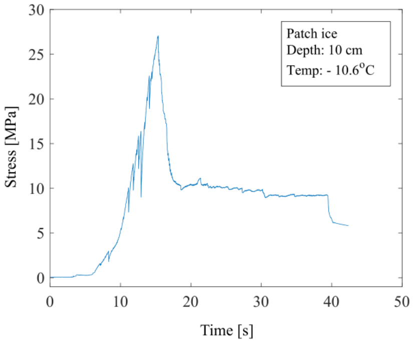

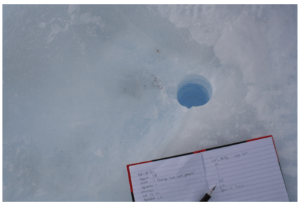

bhj_8107

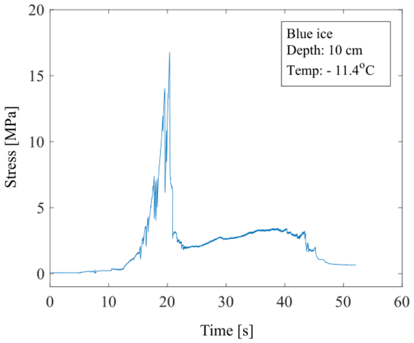

bhj_9101

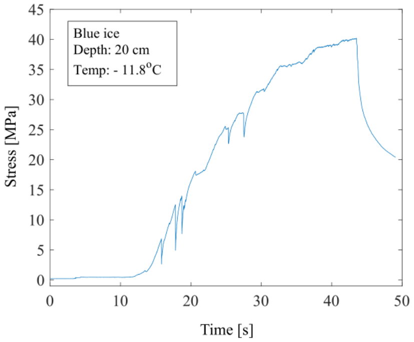

bhj_9102

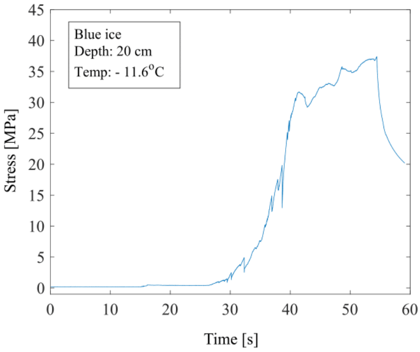
Blue ice
Depth: 20 cm
Temp: - 11.6°C
Stress [MPa]
Time [s]
0
5
10
15
20
25
30
35
40
45
0
10
20
30
40
50
60